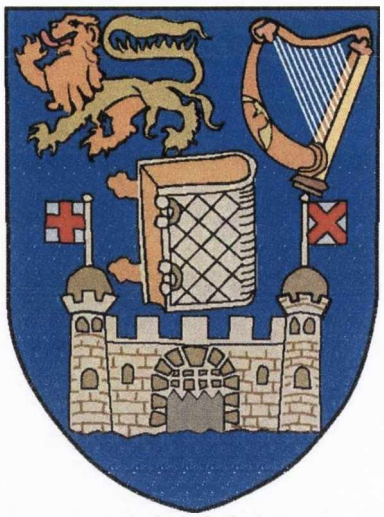

Charging, doping and gating of a single dangling bond on a bare Si(100)-c(4 × 2) surface

by

Mauro Mantega

A thesis submitted for the degree of
Doctor of Philosophy
School of Physics
Trinity College Dublin

April 2012

Declaration

I, Mauro Mantega, hereby declare that this dissertation has not been submitted as an exercise for a degree at this or any other University.

It comprises work performed entirely by myself during the course of my Ph.D. studies at Trinity College Dublin. I was involved in a number of collaborations, and where it is appropriate my collaborators are acknowledged for their contributions.

A copy of this thesis may be lended or copied by the Trinity College Library upon request by a third party provided it spans single copies made for study purposes only, subject to normal conditions of acknowledgement.

Abstract

Despite the increasing interest in novel materials for the next generation of microelectronic devices, such as graphene and topological insulators, Si(100) surface is still the most important substrate for nano-device applications. Its high stability and the possibility of manipulating and functionalizing the surface properties at an atomic level are opening up new perspectives for a wide range of applications ranging from transistor downscaling, dictated by Moore's law, to quantum computing.

The adsorption of single atoms and small inorganic molecules plays a fundamental role in controlling the passivation, oxidation and epitaxial growth of the surface. Hydrogen passivated Si(100) surfaces, for example, can be patterned by desorbing H atoms through the tip of a scanning tunneling microscope (STM) and a variety of arrangements of coupled dangling bonds (quantum dots) can be created. Furthermore, the morphology and electronic properties of the reconstructed Si(100) surface provide a template for exploring systems with low dimensionality and quantum confinement effects on a real system. The quasi one dimensional dispersion of the Si(100) surface states can be exploited to study the fundamental physics related to real quantum wells.

The dimer rows of the $p(2 \times 2)$ and $c(4 \times 2)$ reconstructed Si(100) surfaces exhibit interesting surface electronic properties originating from the dangling bonds: the empty dangling bond state (π^*) is situated within the silicon bulk band gap and reveals energy dispersion only along the dimer row. The standing wave pattern in the local density of states, affected by surface adspecies, is very sensitive to the precise nature and configuration of the adspecie and it inspired us to develope a non intrusive, non local approach to characterize them. The adsorption of the simplest adspecie, a single H atom, which has a fundamental rôle related to the passivation of the surface and nano-patterning procedures will be presented. The adsorbed H atom, on the otherwise bare Si(100) surface with $c(4 \times 2)$ reconstruction, passivates one of the Si dangling bonds, breaking the Si-Si π-bond and leaving an isolated dangling bond (named the single dangling bond, SDB) on the other site of the dimer. An exhaustive description of the bonding configuration of the single H atom on the surface is presented as a function of the doping of the sample. Two approaches have been adopted.

The first one, called local approach, consists of analyzing local data such as the topography and the LDOS in the proximity of the reacted site to extract information about the bonding configuration of the adspecie.

The second approach, called non-local approach, makes use of nonlocal information, such as the standing wave pattern in the nonlocal density of states far away from the reacted site, to determine the adsorption configuration of the H. The properties of the single dangling bond are also evaluated.

Data are obtained by performing *ab initio* computer simulations and compared with scanning tunneling microscopy and spectroscopy (STM/STS) experiments.

With these tools, we were able to characterize the geometry and the charging state of the SDB for different doping conditions. For n-doped systems, the H-produced SDB is doubly occupied with the H_B configuration being the lowest in energy. This

configuration coincides with the majority specie found in low temperature STM experiments. The H_T configuration is the lowest in energy for p-doped samples, with the SDB state being empty. Finally, according to our calculations, the H_B configuration is predicted to be the lowest in energy for the neutral intrinsic case, and the SDB state is partially occupied and spin-polarized.

The nonlocal approach enabled us to map the phase-shift $\Theta(k)$ and it proved to be a very precise fingerprint for discriminating different H adsorption configurations. It has the potential to become a very general tool to determine the configuration of molecules and adspecies deposited on surfaces where the topographic signatures of different configurations are indistinguishable.

We also found that the configuration and charging state of the SDB are responsible for a gating between the reacted row and a bare adjacent one. The charge present at the reacted site originates a depletion of charge in the adjacent row, due to the Coulomb interaction, which results in a gating effect. The magnitude of the gating is proportional to the charging of the SDB and to the directionality of the SDB orbital.

All the results presented in this thesis can provide an interesting perspective for exploring fundamental properties of coupled systems (e.g. quantum wells) as well as applicative aspects aimed at the fabrication of nano-devices. The gating effect, together with the ability to create quantum wells by nanopatterning the Si(100) with an STM tip, may offer the opportunity to study coupled real quantum wells.

The interplay between charging and geometry can be taken as the basic mechanism for fabricating an atomic-scale switch device. In fact, by tuning the surface doping from p-type to n-type, one may switch between the two H configurations. These have distinct scattering and transport properties, so that the switch can be detected electrically or by mapping the phase-shift using the nonlocal approach method.

At the end of my PhD I was involved in another project with the aim of modelling a heterostructure based on graphene and topological insulators, by means of

first-principles calculations. In the last part of this thesis, the preliminary results concerning the electronic properites of a graphene-Bi_2Se_3 heterostructure are presented. The main idea is to model a material which combines the roboustness of the topological protected surface states of a topological insulator (TI) with the promising transport properties of pristine graphene. For different graphene-TI separations, the evolution of the band gap and the of the band structure is studied. At a close distance between the two subsystems, a conical band in the proximity of the Fermi level originates at the graphene-Bi_2Se_3 interface region. Our preliminary results predict this band to be topologically protected even though further investigations are required. A topological protected state in graphene, once supported by experimental verification, would candidate this versatile material as a very promising replacement for silicon aimed at nanoelectronics applications.

Acknowledgements

Over the past four years, I received a lot of help and support from a large number of people, without whom none of this research would have been possible.

First of all, I would like to thank my supervisor, Prof. Stefano Sanvito. His guidance and enthusiasm, together with his competence and helpfulness, were invaluable over these last four years.

I would like to thank Dr. Ivan Rungger who performed the SMEAGOL calculations presented in this thesis. His suggestions and the very useful discussions we had were really appreciated.

I would also like to thank my experimental collaborators, Prof. John J. Boland and Dr. Borislav Naydenov. All of the "experimental vs. theoretical" meetings we had were very useful and gave me an all-round view of my project. I would particularly like to thank Dr. Borislav Naydenov who performed all of the experiments presented in this thesis.

I would like to thank all the people (past and present) of the Computational Spintronics Group who contributed to establishing a very relaxed and pleasant working atmosphere within the group, and made it an ideal environment to work. Some of

them were not only colleagues but became close friends of mine. I would like to thank the people I met in CRANN. I had very interesting discussions with many of them and they were always very encouraging and supportive.

Furthermore, I would like to thank the Trinity Center for High Performance Computing (TCHPC) and the Irish Center for High-End Computing (ICHEC) for providing the computational resources required for the work presented in this thesis. I am grateful to the Science Foundation of Ireland (SFI) for providing the founding for my scholarship. I would like to thank Stefania and Lia for the invaluable assistance they gave me with everything concerning bureaucracy.

Finally, I would like to thank my family for being so supportive at this and every stage of my life.

Go raibh míle maith agaibh!

Contents

CHAPTER 1

Introduction

The invention of the transistor in 1947 by John Bardeen, Walter H. Brattain, and William B. Shockley from Bell Labs started the semiconductor revolution, thus giving birth to a series of new devices with remarkable potential for expanding the applicability of electronic equipment. Transistors, with their subsequent developments as integrated circuits, are made of crystalline solid materials called semiconductors, whose electrical properties can be tuned over an extremely wide range through the addition of small amounts of other chemical species (doping). The electric current in semiconductors is carried by electrons, which have a negative charge, and/or by holes, analogous entities carrying a positive charge. The availability of two kinds of charge carriers in semiconductors is a valuable property exploited in many electronic devices made of such materials. The electrical properties of semiconductors are extremely sensitive to the slightest trace of other elements, and high purity is usually required so that they can be used for making semiconductor devices. During World War II, methods of purifying germanium were developed and this explains

why early transistors were produced using such material. A few years later, research on the purification of silicon succeeded in producing samples suitable for semiconductor devices, and new devices made of silicon were manufactured from about 1960. Since then silicon, due to its abundance and consequent low price, quickly became the preferred raw material for electronic device applications.

There are a few more reasons why silicon overtook germanium as the basic material for the semiconductor industry. Firstly, silicon retains its semiconducting properties at higher temperatures than germanium does. Silicon diodes can be operated at temperatures up to 200 °C, whereas germanium diodes cannot be operated above 85 °C. Secondly, silicon, unlike germanium, forms a tenaciously adhering oxide film (silicon dioxide) with excellent electrical insulating properties when it is heated to high temperatures in an oxygen rich atmosphere. This film is utilized as a mask to permit the desired impurities that modify the electrical properties of silicon to be introduced into it during the manufacturing of semiconductor devices. The mask pattern, formed by a photolithographic process, permits the creation of tiny transistors and other electronic components in silicon. The optimization in the fabrication process followed by the transistors miniaturization brought the integration of a large number of transistors into a single integrated circuit called a microprocessor. This device contained all the arithmetic, logic, and control circuitry required to perform the functions of computers central processing unit (CPU). The first large scale production microprocessor, the 4004, was introduced by Intel Corporation in 1971, together with the memory integrated circuit. It included 2300 transistors built with a $10\mu m$ process. The stage was now set for the computerization of small electronic equipment [1]. The silicon-processing lengh scale has shrunk tenfold every 15 years since 1971, following Moore's low [2], and nowadays it stands at 22 nm, which translates into microprocessors incorporating a few billions of transistors. At such dimensions quantum effects, such as the onset of quantum tunneling of electrons through po-

tential barriers, limit the ability to confine charges to a densely packed array. The physical limit for the transistor size is estimated to be around 5 nm, a distance where direct tunneling of electrons between source and drain will occur. The race to miniaturization has recently presented ample research and development opportunities in the growth and characterization of novel materials for the next generation of electronic devices such as graphene, topological insulators, hybrid organomolecular silicon, multiferroics etc. [3–13]

Despite this important and sustained effort, to date the Si(100) surface still remains the most important substrate for nano-device applications [3, 14–18]. Its high stability and the possibility of manipulating and functionalizing the surface properties at an atomic level are opening up new perspectives for a wide range of applications ranging from transistor downscaling, dictated by Moore's law, to quantum computing [19–22]. The adsorption of single atoms and small inorganic molecules plays a fundamental role in controlling the passivation, oxidation and epitaxial growth of the surface [23, 24]. Hydrogen passivated Si(100) surfaces, for example, can be patterned by desorbing H atoms through the tip of a scanning tunneling microscope (STM) [25] and a variety of arrangements of coupled dangling bonds (quantum dots) can be created [26, 27]. Furthermore, the morphology and electronic properties of the reconstructed Si(100) surface provide a template for exploring systems with low dimensionality and quantum confinements effects on a real system.

The quasi one dimensional dispersion of the Si(100) surface states (see next section for details) can be exploited to study the fundamental physics related to real quantum wells. Yokoyama *et al.* were able to confine surface electrons and create one dimensional quantum wells on a Si(100)-c(4×2) surface by depositing Al atoms on the surface through the tip of a scanning tunneling microscope [28]. 3D topographic images, acquired at T=63 K, exhibit a standing wave pattern with two, three and four peaks between the Al ad-dimer chains for sample biases of 0.9 V, 1.1 V and

1.2 V, respectively [see Fig. 1.1(a)]. A similar experiment was performed by Sagisaka *et al.*. Quantum confinement of surface electrons was achieved by depositing W atoms on a Si dimer row of the Si(100) surface from the tip of a scanning tunneling microscope [29,30]. The differential conductance (dI/dV) images for different sample biases show a standing wave pattern with an increasing number of bright spots (peaks) as a function of the bias. The bright protrusions at the borders of the images are the confining W atoms [see Fig. 1.1(b)]. Boland *et al.* created a one dimensional quantum well on the Si(100) surface by depositing small Pt clusters [31]. The standing wave pattern in the differential conductance (dI/dV) image, acquired at 77 K, resambles the "particle in a box" picture [see Fig.1.1(c)].

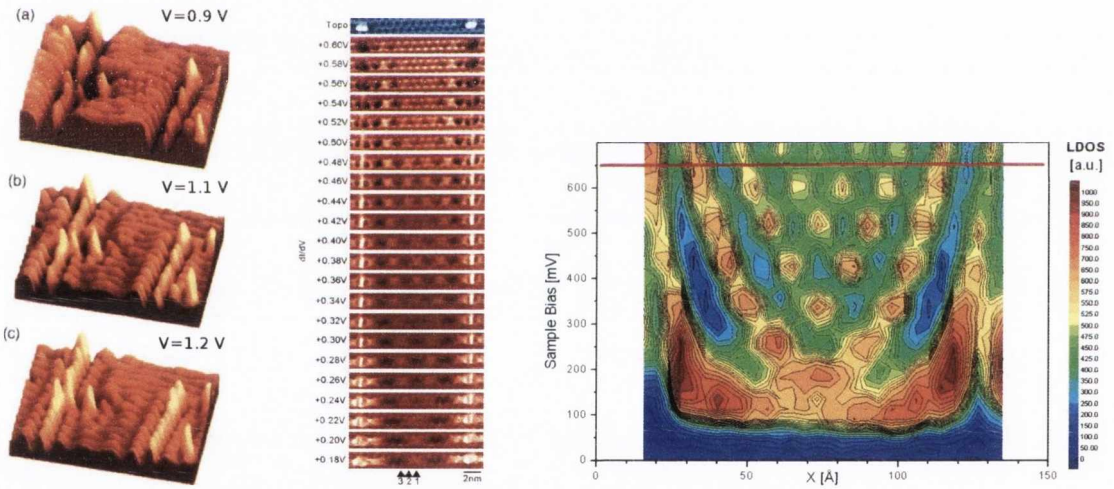

(a) Yokoyama *et al.* (b) Sagisaka *et al.* (c) Boland *et al.*

Figure 1.1: Standing wave pattern in the scanning tunneling microscope images obtained by 1D confinement of surface electrons in real quantum wells. (a) Yokoyama *et al.* were able to create quantum wells by depositing Al atoms on the Si(100) surface from the tip of a scanning tunneling microscope [28]. (b) Sagisaka *et al.* used W atoms to confine electrons along the dimer row of the Si(100) surface [29,30]. (c) Boland *et al.* created a one dimensional quantum well by depositing small Pt clusters on the dimer row of the Si(100) surface [31].

Besides the attention to the fundamental physics related to real quantum wells, there is an increasing interest in Si-based platforms for quantum computing applications. The race to miniaturization has driven the length scale of the silicon

lithographic process used for transistors production down to the nanoscale (22nm, nowadays). A further shrinking in the dimensions will see the onset of quantum effects, such as quantum tunneling of electrons through potential barriers, limiting the ability to confine charges to a densely packed array. In addition, the number of donors in the transistor channel are discrete and countable and the device starts to be very sensitive to the precise location of individual dopants whose electrical characteristics can be observed at low temperatures [32]. These quantum limit issues can be turned into advantages by building a device which relies on coherent quantum behaviour to store and recover information. Morton *et al.* showed that the nuclear spin and the electron spin can be used to store the quantum information. Silicon is particularly attractive for hosting spin quantum bits (qubits) because it possesses a low spin-orbit coupling which determines a long spin coherence time. Spin qubits can be realized in silicon using confined donor-bound spins or lithographically defined silicon-based quantum dots [33, 34].

Despite new materials are promising candidates for future applications in electronics, the interest around the Si-based technology is far from fading away. The advanced state of Si electronics and its capability to integrate novel applications, such as spin qubits, with the existing technology, requires an accurate study of the electronic properties of low dimensional structures and the one depending on the precise position of the dopants.

1.1 Si(100) surface

Surface reconstruction refers to the process by which atoms at the surface of a crystal assume a different structure than that of the bulk. This process is due to the abrupt change in the external potential felt from electrons, which goes from the bulk value, inside the crystal, to vanishing above the surface. The system reacts to the potential change by minimizing the energy, thus leading to interesting effects both in the

atomic and electronic structure near the surface. The changes in the atomic positions of surface atoms can be such that the periodicity of the surface differs from that of the atoms on a bulk-terminated plane with the same orientation. The standard way to describe the new periodicity of the surface is by multiples of the lattice vectors of the corresponding bulk-terminated plane. For instance, a $n_1 \times n_2$ reconstruction on the (klm) plane is such that the lattice vectors on the plane are n_1 and n_2 times the primitive lattice vectors of the ideal, unreconstructed, bulk-terminated (klm) plane [35]. The Si(100) bulk-terminated plane consists of atoms that have two bonds covalent to the rest of the crystal, while the other two bonds on the surface have been severed. The severed bonds are called dangling bonds and each of them is half-filled, i.e. it contains only one electron. If we consider a tight-binding approximation of the Si electronic structure, with a four sp^3 orbital basis associated to each atom, it follows that the dangling bond states have an energy in the middle of the band gap. This energy is also the Fermi level, since the Si dangling bond occupied states are the highest occupied states. The surface Si atoms come together in pairs, giving rise to a 2×1 periodicity. New bonds are formed, called dimer bonds, with each bonded pair of atoms called a dimer. The formation of a dimer bond eliminates two of the dangling bonds in the unit cell, one per dimer atom. This leaves two dangling bonds, one per dimer atom, which, for symmetric dimers, are degenerate and half-filled. The energy of these states determines the position of the Fermi level, since they are the highest occupied states. The dimers, in the lowest energy configuration of the system, are tilted: one of the atoms is a little higher than the other when considered relatively to the average height of surface atoms, which is taken as the macroscopic definition of the surface plane.

This tilting has an important effect on the electronic levels, as illustrated schematically in *Fig. 1.2*. The up-atom of the dimer has three bonds at an angle close to 90^o. Such an atom is in a bonding configuration close to sp^3: it forms covalent bonds

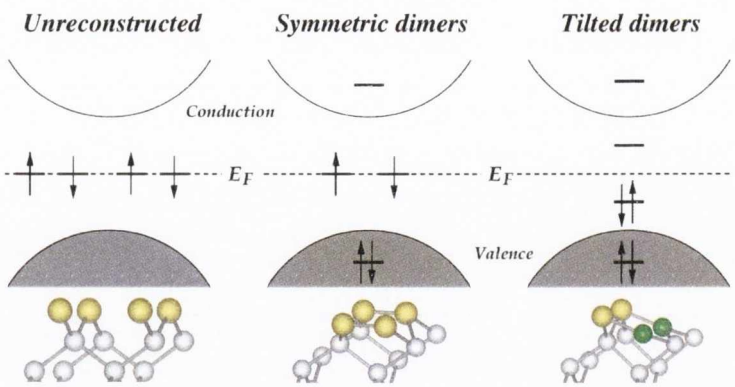

Figure 1.2: Effects of dimerization and tilting on the states around the Fermi level, E_F, for the reconstructed Si(100) surface.

through three of its *sp* orbitals, while one of them does not participate to the bonding. At the same time, the down-atom of the dimer has three bonds which are almost planar. These are in a bonding configuration close to sp^2 and form three bonding orbitals containing one *s* and two *p* states, while the third *p* orbital, the one perpendicular to the plane, does not participate to the bonding. When considering the two orbitals that do not participate to the bonding, it can be seen that the *sp* orbital of the up-atom has lower energy than the *p* orbital of the down-atom. Consequently, the two remaining dangling bond electrons are accommodated by the up-atom *sp* orbital, which becomes filled, while the down-atom *p* orbital remains empty. The net effect is that the surface has semiconducting character, with a small band gap between the occupied up-atom *sp* state and the unoccupied down-atom *p* state. The Fermi level is now situated in the middle of the surface band gap (*Fig. 1.2*), which is smaller than the band gap of the bulk [35]. The semiconducting nature of the surface was established more that 30 years ago by photoemission spectroscopy experiments (PES) [36,37] and confirmed by inverse-photoemission, photoelectron and STM spectroscopies [38–40].

Beside the dimerization and tilting processes within the 2×1 surface unit cell, there is a long range reconstruction process which consists of dimers with alternating buckling. The $p(2 \times 2)$ reconstruction shows alternating buckling along the dimer

rows while alternating buckling occurring also along the direction perpendicular to the dimer rows leads to the $c(2\times4)$ reconstruction. The distance between the Si atoms forming the second surface layer (connected to the backbonds of the topmost layer) is different depending on the position of the surface Si atoms along the direction perpendicular to the surface. The distance between the Si atoms attached to the backbonds of the top Si atom of the dimer is shorter with respect to the one between the Si atoms attached to the backbonds of the bottom atom of the dimer. This results in an alternation of the dimers as a more efficient way to accomodate the surface stress in the underlying layer of Si atoms. The apparent $p(2 \times 1)$ surface symmetry observed at room temperature can be attributed to the thermally activated flip-flop motion of dimers, while $c(4 \times 2)$ and $p(2 \times 2)$ surface reconstructions are detected at low temperature (*Fig. 1.3*). STM experiments [41–44], low-energy electron diffraction (LEED) [45] and angle-resolved photoemission spectroscopy (ARPES) [44] confirm the coexistence of $p(2 \times 2)$ and $c(4 \times 2)$ reconstructions at low temperature (below 200K), thus revealing a prevalence for the $c(4 \times 2)$ reconstruction pattern. *Ab initio* total energy calculations, in a very good agreement with experiments, indicate an energy difference between the $p(2\times2)$ and $p(2\times1)$ reconstructions of $\sim$0.5 eV/dimer while the difference between the $c(4 \times 2)$ and the $p(2 \times 2)$ is $\sim$0.005 eV/dimer, the $c(4 \times 2)$ being lower in energy. The small energy difference between $p(2 \times 2)$ and $c(4 \times 2)$ reconstructions explains the coexistence of both periodicities at low temperature [46–48].

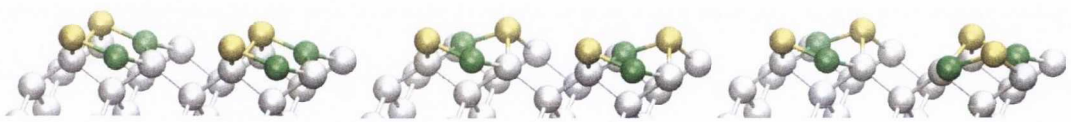

Figure 1.3: Perspective view of the Si(100) surface with, respectively, $p(2 \times 1)$, $p(2 \times 2)$ and $c(4 \times 2)$ reconstruction (from left to right). The yellow and green silicon atoms are respectively the top and bottom atom of the surface dimers.

The morphology of the structure is reflected on the electronic properties of the surface. The dimer rows of the $p(2\times2)$ and $c(4\times2)$ reconstructed Si(100) surfaces ex-

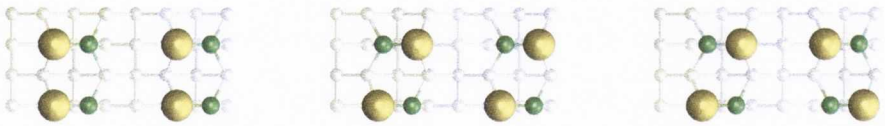

Figure 1.4: From left to right: top view of a balls-and-sticks model of the Si(100) surface with, respectively, $p(2 \times 1)$, $p(2 \times 2)$ and $c(4 \times 2)$ reconstruction.

hibit interesting surface electronic properties originating from the π dangling bonds: the empty dangling bond state (π^*) is situated within the silicon bulk band gap and reveals energy dispersion only along the dimer row [Fig. 1.5(a)] [46,47,49]. Hence the π^* band exhibits a quasi-one-dimensional (1D) character, which has been confirmed by scanning tunneling microscopy observations of surface standing waves [28–30, 50]. These surface states in the conduction band are almost decoupled from the bulk and

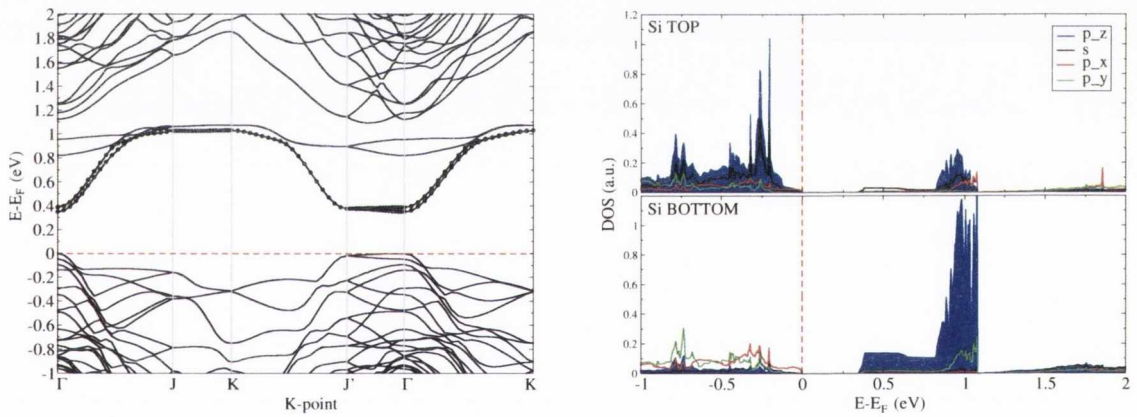

(a) Band structure

(b) Density of states

Figure 1.5: Band structure (a) and density of states (b) of the Si(100) surface with $c(4 \times 2)$ reconstruction for a 2×4 supercell. (a): the filled circles bands are the π^* bands, one for each dimer row. These bands show a pronounced dispersion along the direction of the dimer rows ($\Gamma - J$ and $K - J'$) while they are almost flat in the direction perpendicular to the dimer row, exhibiting a quasi-one-dimensional character. (b): the π^* bands are mainly due to states coming from the bottom atom of the dimers.

they are mainly due to states coming from the bottom atoms of the surface dimers, as shown by the density of states plots in Fig. 1.5(b). The standing wave pattern in the local density of states, induced by surface adspecies, is very sensitive to the precise nature and configuration of the adspecie and it inspired us to develope a

non intrusive, non local approach to characterize them. The thesis will focus on the adsorption of the simplest adspecie, a single H atom, which has a fundamental rôle related to the passivation of the surface and nano-patterning procedures. The aim of this work is to study the effects of a single hydrogen atom adsorbed on an otherwise bare Si(100) surface with $c(4 \times 2)$ reconstruction. The adsorbed H atom on the surface passivates one of the Si dangling bonds, breaking the Si-Si π-bond thus leaving an isolated dangling bond on the other site of the dimer [51]. The dimer containing the adsorbed H atom will be referred throughout the text as the reacted dimer and the dangling bond on the opposite site of the same dimer as the single dangling bond (SDB). The aim of this thesis will be to provide an exhaustive description of the bonding configuration of a single H atom on a bare Si(100)-$c(4 \times 2)$ surface as a function of the doping of the sample. Two approaches have been adopted.

The first one, called *local approach*, consists of analyzing local data such as the topography and the LDOS in the proximity of the reacted site to extract informations about the bonding configuation of the adspecie. These data are obtained by performing *ab initio* computer simulations and compared with scanning tunneling microscopy and spectroscopy experiments at a spatial position corresponding to the reacted site.

The second approach, called *non-local approach*, makes use of nonlocal informations, such as the standing wave pattern in the nonlocal density of states far away from the reacted site, in order to determine the adsorption configuration of the H.

The properties of the single dangling bond are also evaluated. In particular, a complete spectroscopic analysis of the charging state of the SDB is carried out as a function of the H bonding configuration and the doping of the sample by means of *ab initio* calculations and STM/STM measurements. The reacted dimer acts as a potential barrier for the electrons travelling on the same dimer row and, depending on the H configuration and the SDB charging state, on the adjacent row. The aspects

related to the details of the gating effect between adjacent rows will be addressed in this thesis.

1.2 Quantum well

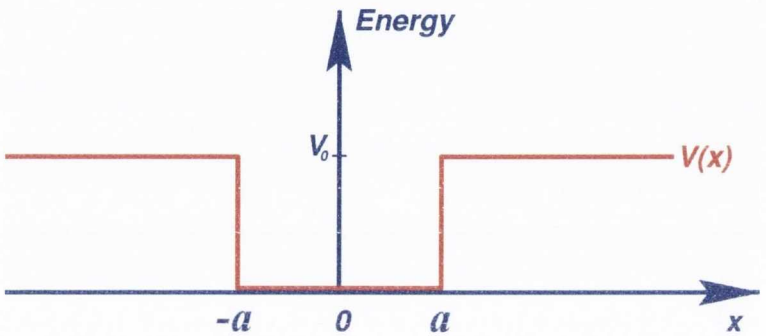

Figure 1.6: Schematic representation of a potential well formed by two barriers located at $|x| = a$.

In quantum mechanics, the one dimensional space lying between two potential barriers at a distance of the same order of magnitude as the de Broglie wave length, is called a quantum well. The main characteristic of a quantum well is that is only allows states with discrete energy values. I will discuss a few examples of the quantum well states in the chapters of this thesis discussing our results (Chaps. 4, 5), therefore it is worthwhile to present a brief overview of the basic physics describing a quantum well. A more comprehensive discussion about quantum wells can be found in any quantum mechanics book, for example in Ref. [52].

1.2.1 Infinite potential barriers

Let us consider the case of two infinitely high barriers ($V_0 \to \infty$) located at the positions $|x| = a$, as shown in Fig. 1.6. Due to the infinite barrier height, the wave function ψ of a particle moving inside the well does not penetrate inside the barrier. This leads to a boundary condition requiring the wave function to vanish at the barrier interfaces so that $\psi = 0$ at $|x| = a$. Inside the central region, the potential

vanishes and the Schrödinger equation becomes the one described by a free particle with energy ε and mass m

$$\frac{\partial^2 \psi}{\partial x^2} + k^2 \psi(x) = 0, \tag{1.1}$$

where the wave vector k is defined as

$$k = \sqrt{\frac{2m\varepsilon}{\hbar^2}} \qquad \text{and} \qquad \varepsilon = \frac{\hbar^2 k^2}{2m}. \tag{1.2}$$

The solutions at the right-hand and left-hand side boundary are, respectively

$$\psi_1(a) = Ae^{ika} + Be^{-ika} = 0 \qquad \text{and} \qquad \psi_2(a) = Ae^{-ika} + Be^{ika} = 0. \tag{1.3}$$

These two conditions describe the wave function of a free particle approaching and being reflected by each barrier. Since the two equations concern to the same particle, they cannot give independent solutions and they must be degenerate so that the determinant of the coefficients must vanish

$$\begin{vmatrix} e^{ika} & e^{-ika} \\ e^{-ika} & e^{ika} \end{vmatrix} = 0. \tag{1.4}$$

This leads to the requirement that

$$\sin(2ka) = 0, \tag{1.5}$$

which imposes discrete values for k and ε

$$k_n = \frac{n\pi}{2a} \qquad \varepsilon_n = \frac{n^2\pi^2\hbar^2}{8ma^2} \qquad \text{with} \qquad n = 1, 2, 3, ... \tag{1.6}$$

Hence, the spacing between the allowed energy values increases quadratically with the index n. By substituting the value for k back into one of the equation for the

boundary conditions, for example Eq. 1.3, it leads to

$$\frac{B}{A} = -e^{in\pi} = (-1)^{n+1}. \tag{1.7}$$

By considering increasing values of the index n, the wave functions alternates between cos and sin

$$\psi_n(x) = \begin{cases} A\cos\left(\dfrac{n\pi x}{2a}\right) & n \text{ odd} \\ A\sin\left(\dfrac{n\pi x}{2a}\right) & n \text{ even} \end{cases}. \tag{1.8}$$

This can be recast into a single equation by offsetting the position so that

$$\psi_n(x) = A\sin\left[\frac{n\pi}{2a}(x+a)\right]. \tag{1.9}$$

By normalizing the wave function, the constant A can be determined,

$$\langle\psi_n(x)|\psi_n(x)\rangle = A^2\int_{-a}^{a}\sin^2\left[\frac{n\pi}{2a}(x+a)\right]dx = 1, \tag{1.10}$$

leading to

$$A = \frac{1}{\sqrt{a}}. \tag{1.11}$$

The particle is said to be in a pure state if it occupies a single energy level (eigenvalue of the Hamiltonian). Usually, the particle occupies a linear superposition of energy levels, its total wave function, on the average, will receive contributions from many of them. Then the wave function is a sum over the Fourier series, where the coefficients are related to the probability for each level to be occupied. This can be written as

$$\psi_n(x) = \sum_n \frac{c_n}{\sqrt{a}}\sin\left[\frac{n\pi}{2a}(x+a)\right], \tag{1.12}$$

where the probability of the state n to be occupied is given by $|c_n|^2$ and the coefficients c_n are subject to the limitation on the total probability (particle number

conservation) that

$$\sum_n |c_n|^2 = 1. \tag{1.13}$$

1.2.2 Finite potential barriers

In a situation where the potential barrier is not infinite, the wave function penetrates into the region under the barriers. If the energy ε of the particle is lower than the height of the barrier V_0, then the particle can propagate freely in the region $|x| < a$, for which the Schrödinger equation has the form aforementioned in Eq. 1.1, and k is given by

$$k^2 = \frac{2m\varepsilon}{\hbar^2}. \tag{1.14}$$

In the range $|x| > a$, the wave function decays inside the barrier and the Schrödinger equation becomes

$$\frac{\partial^2\psi}{\partial x^2} + \gamma^2\psi(x) = 0 \qquad \text{with} \qquad \gamma^2 = \frac{2m(V_0 - \varepsilon)}{\hbar^2}. \tag{1.15}$$

The solution of Eq. 1.15 has the form

$$\psi(x) = Ce^{-\gamma|x|} \qquad \text{for} \qquad |x| > a, \tag{1.16}$$

γ being the damping coefficient. Due to the symmetry of the potential, the Schrödinger equation would have either even or odd symmetry solutions like the ones given in Eq. 1.8. The basic properties discussed for the infinite barriers case will carry over to the present one and the solutions in the well region are expected to be either sin or cos [52]. According to the usual boundary conditions, both the wave function and its derivative must match at each boundary. This leads to four equations with two unknowns: the amplitude of C for the sin and cos wave functions and the wave vector k (and hence γ) for the bound state energy levels. The problem can be solved

by requiring the logarithmic derivative ψ'/ψ to be continuous. This enables us to eliminate immediately the constants, rather then apply the boundary conditions to the wave function and its derivative separately [53]. The even- and odd-symmetry (cos and sin) wave functions will be treated separately.

For the even-symmetry wave function given by Eq. 1.8, the logarithmic derivative is

$$\frac{\partial}{\partial x} ln[\psi(x)] = \frac{-k\sin(kx)}{\cos(kx)} = -k\tan(kx). \tag{1.17}$$

The logarithmic derivative of the wave function inside the barrier is $\gamma\,\mathrm{sign}(x)$. By matching the wave function at the boundary $x = a$ (by symmetry reasons this equals $x = -a$) gives

$$k\tan(ka) = \gamma, \tag{1.18}$$

which determines the allowed values for the bound states energies. By introducing the reduced variables ξ and β, the Eq. 1.18 becomes

$$\tan(\xi) = \sqrt{\frac{\beta^2}{\xi^2} - 1}, \qquad \text{with} \qquad \xi = ka \qquad \text{and} \qquad \beta^2 = \frac{2mV_0a^2}{\hbar^2}. \tag{1.19}$$

The right-hand side of Eq. 1.19 is a monotonically decreasing function and only the energy values in the range $(0,\ V_0)$ constitute bound states. In general, graphical solutions are required to solve the Eq. 1.19. The left-hand side and the right-hand side of Eq. 1.19 are plotted separately in Fig. 1.7, and the circled crossings are the allowed solutions. Bearing in mind the graphical representation, if the potential amplitude V_0 is reduced, β and ξ decrease and the available range for the two curves to intersect becomes smaller. However, the right-hand side of Eq. 1.19 varies from infinity (for $\xi = 0$) to zero (for $\xi = \beta$), while the tangent function goes to zero for $\xi = 0$ or $n\pi$ and diverges for $\xi =$ odd or $\pi/2$. Therefore there is at least one crossing. The graphical solutions are marked with circled crossings in Fig. 1.7. Larger values of the potential amplitude V_0 allow more bound states energies.

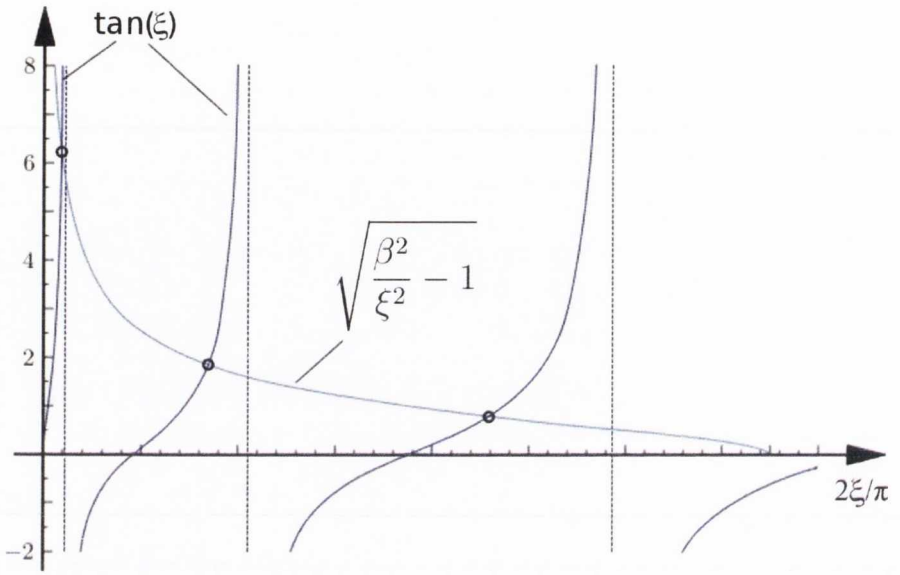

Figure 1.7: Left-hand side and right-hand side of Eq. 1.19 are plotted separately and the graphical solutions are indicated by the circled crossings.

The boundary condition on the odd-symmetry wave functions of Eq. 1.8 is calculated in the same fashion. The logarithmic derivative for the propagating waves in the region $|x| < a$ must match the one of the decaying wave functions inside the barrier for $|x| > a$. In formulas

$$\begin{aligned} \frac{\partial}{\partial x} ln[\psi(x)] &= \frac{k\cos(kx)}{\sin(kx)} = k\cot(kx) \qquad \text{for} \quad |x| < a \\ \frac{\partial}{\partial x} ln[\psi(x)] &= -\gamma sgn(x) \qquad\qquad\quad \text{for} \quad |x| > a. \end{aligned} \tag{1.20}$$

By matching them in one of the boundaries, the following expression is obtained

$$k\cot(kx) = -\gamma \qquad \text{or} \qquad \cot(\xi) = -\sqrt{\frac{\beta^2}{\xi^2} - 1}, \tag{1.21}$$

where β and ξ are defined by Eq. 1.19. The graphical solution is shown in Fig. 1.8 The left-hand side of Eq. 1.21 starts on the opposite side of the ξ axis, with respect to the even symmetry case and no crossing is guaranteed.

By comparing the even and odd solutions (Figs. 1.7 and 1.8), the alternation between them can be noticed. For small amplitude of the potential V_0, or for small

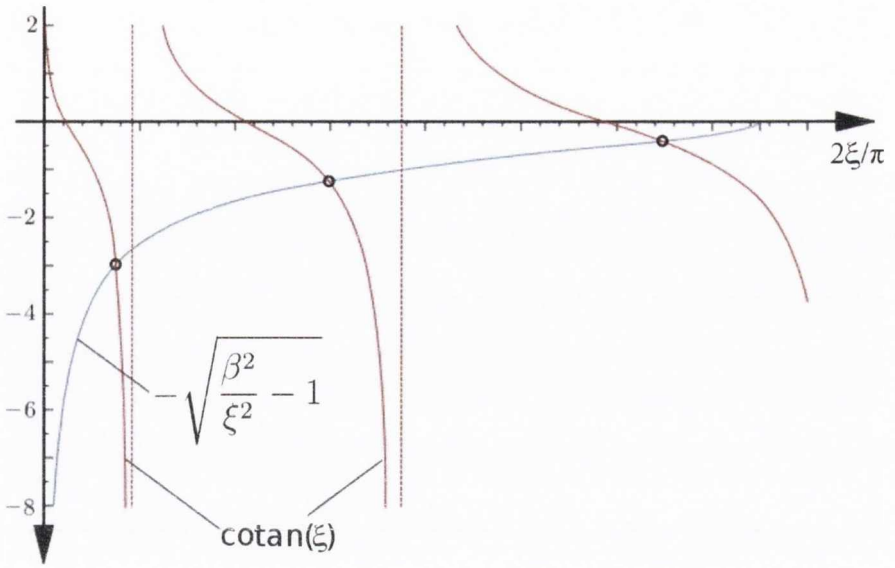

Figure 1.8: Left-hand side and right-hand side of Eq. 1.21 are plotted separately and the graphical solutions are indicated by the circled crossings.

widths of the well, there is at least one bound state lying just below the top of the well. An increase of the potential (or width) allows more possible bound states. The first bound state has an even symmetry wave function. The following states alternate between odd and even symmetry [52].

The case with $\varepsilon > V_0$ is not treated in this thesis and it can be found in a standard quantum mechanics book (e. g. in Ref. [52]).

1.3 Scanning Tunneling Microscope

1.3.1 Introduction

Most of the simulated data presented in this thesis is compared with experiments performed with a scanning tunneling microscope. For this reason it is worthwhile introducing the basic concepts behind this very successful and well established technique.

Scanning tunneling microscope (STM) is a very powerful microscope developed to study the electronic and structural properties of surfaces with atomic precision.

It was invented by Binnig and Rohrer [54–57] (who were awarded the Nobel Prize in Physics in 1986) and implemented by Binnig, Rohrer, Gerber and Weibel [58,59]. A schematic of the STM is shown in Fig. 1.9. It consists of a probe tip, usually made

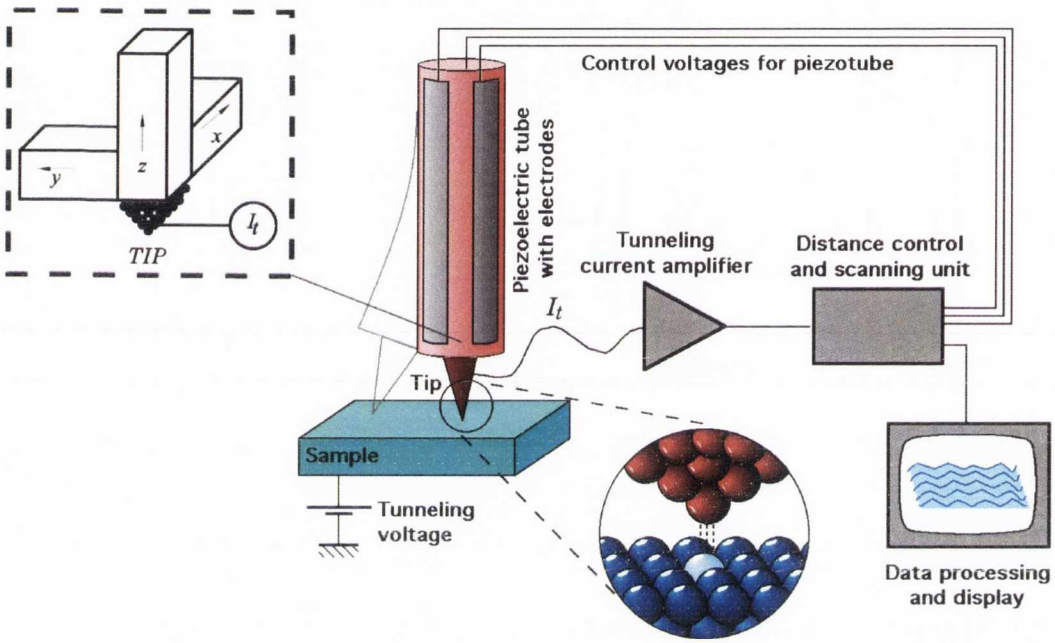

Figure 1.9: Schematic diagram of the scanning tunneling microscope (figure from Michael Schmid, TU Wien). A probe tip is operated by applying a voltage to the piezotube, consisting of piezoelectric transducers along the x, y and z axes. As the tip scans over the sample surface, a contour plot of tunneling current isosurfaces is traced. The tip-sample distance is tuned through a feedback loop where the tunneling current $I(V)$ is constantly compared to a reference value.

of W or Pt, attached to a piezotube which includes three mutually perpendicular piezoelectric transducers along the x, y and z axis. By applying a voltage, the piezoelectric transducers expand or contracts, allowing the tip to scan the xy plane. The transducer along the z axis is used to position the tip a few angstroms away from the sample such that the electron wave function of the tip overlaps with the one of the sample surface. When a bias voltage is applied between the tip and the sample a tunneling current flows. The tunneling current is amplified by the current amplifier to become a voltage, which is compared to a reference value according to a feedback loop. If the tunneling current is larger than the reference value, then the voltage applied to the transducer acting on the z axis tends to withdraw the tip from the

sample surface and vice versa. An equilibrium position is then established through the feedback loop. As the tip scans over the xy plane of the sample surface, it traces a contour plot of tunneling current isosurfaces, corresponding to a two dimensional array of equilibrium z positions. The line-scan image is a sequence of curves, each of which representing a contour along the x direction with constant y [60].

The tunneling current $I(V)$ is then the basic quantity measured in a STM experiment. The STM operates mainly according two different modes. The constant current mode consists of a scan of the tip position over the sample surface to obtain a two-dimensional map of the tunneling current. In practice this is realized by keeping the current fixed and by varying the tip-sample distance accordingly. The experimental quantity measured in the constant current mode is the corrugation of the tip, defined as the difference between the largest and smallest tip-sample distance. This experimental setup allows a high resolution perpendicular to the surface, due to the exponential dependence of the tunneling current on the width of the barrier (tip-sample distance). This configuration is able to reach atomic resolution and single adatoms and single defects can be resolved.

The spectroscopic mode consists in varying the applied bias voltage and in measuring the consequent change in the tunneling current. This mode allows a local investigation of the electronic structure of the sample. The fundamental quantity acquired in a STS (scanning tunneling spectroscopy) experiment is the differential conductivity dI/dV as a function of the applied bias V. Hence, from the differential conductivity the LDOS of the sample can be estimated [61–67].

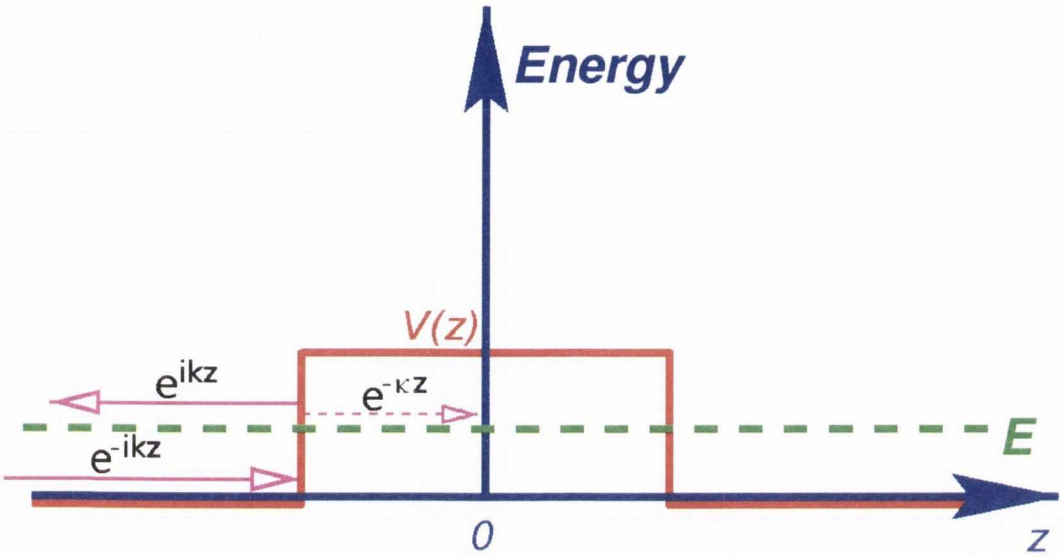

Figure 1.10: Schematic plot of an electron in a potential barrier $V(Z)$.

1.3.2 One dimensional model for tunneling

In quantum mechanics an electron with energy E, moving in a potential $V(z)$ is described by the Schrödinger equation

$$\left[-\frac{\hbar^2}{2m}\frac{d^2}{dz^2} + V(z)\right]\psi(z) = E\psi(z), \tag{1.22}$$

where m is the electron mass. In the case of a square potential barrier, like the one shown in Fig. 1.10, the Eq. 1.22 has solutions

$$\psi(z) = \psi(0)e^{\pm ikz}, \tag{1.23}$$

where k is the wave vector given by

$$k = \frac{\sqrt{2m(E-V)}}{\hbar}. \tag{1.24}$$

These solutions describe an electron moving towards the potential barrier or away from it (incident and reflected waves), respectively. Within the potential barrier

Eq. 1.22 has the solution

$$\psi(z) = \psi(0)e^{-i\kappa z}, \tag{1.25}$$

where

$$\kappa = \frac{\sqrt{2m(V-E)}}{\hbar} \tag{1.26}$$

is the decay constant. The wave function of the electron penetrating the barrier has an exponential decay. Thus the probability density of finding an electron inside the barrier is finite and nonzero and it is proportional to $|\psi(0)|^2 e^{-2\kappa z}$. This simple model may be used to explain the basic features of metal-vacuum-metal tunneling, i.e. the basic mechanism behind the STM microscope. The work function ϕ of a metal surface is defined as the minimum energy required to remove an electron from the bulk to the vacuum level and it depends, in general, on the material and on the crystallographic orientation of the surface. In metals, when neglecting the thermal excitation, the Fermi level E_F is the upper limit of the occupied states. If considering the vacuum level as a reference point of energy, $E_F = -\phi$. In this simple model the work function of the tip is assumed to be equal to the one of the sample. When a bias V is applied, the electron can tunnel from the sample to the tip and *vice versa*. An electron belonging to the sample, occupying a state ψ_n with energy E_n lying between $E_F - eV$ and E_F, has a chance to tunnel into the tip. By assuming that the applied bias eV is much smaller than the work function ϕ, then the energy window explored by the bias is very close to the Fermi level E_F. The energy states of interest in the sample fall into this window so that $E_n \approx -\phi$. The probability w of an electron belonging to the n-th of these states to be at the tip surface $z = W$ is

$$w \propto |\psi_n(0)|^2 e^{-2\kappa W}, \tag{1.27}$$

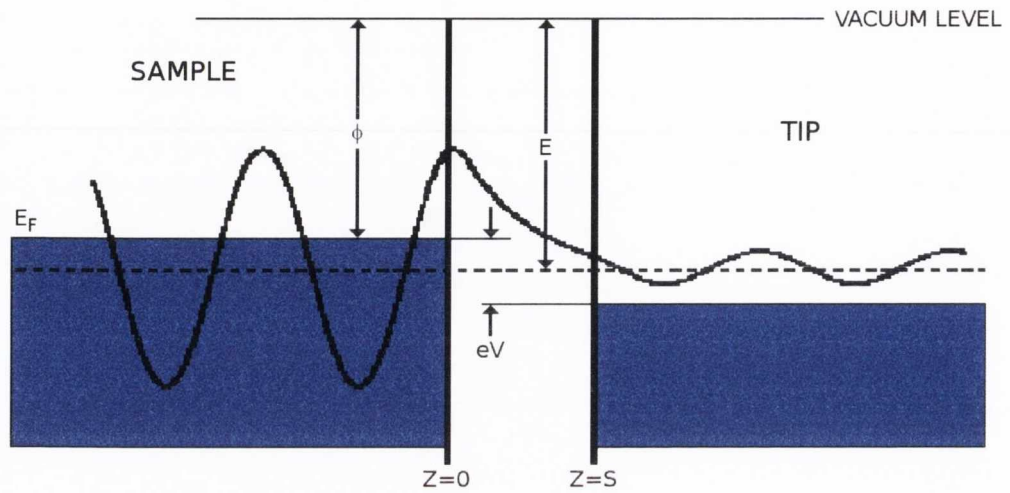

Figure 1.11: Schematic representation of a metal-vacuum-metal tunneling junction. Figure from Chen, see ref. [60].

where $\psi_n(0)$ is the value of the n-th sample state at the sample surface and

$$\kappa = \frac{\sqrt{2m\phi}}{\hbar} \tag{1.28}$$

is the decay constant of a sample state near the Fermi level in the barrier region [60].

Ordinarily, in a typical STM experiment, the DOS of the tip does not vary (in first approximation) while scanning over the sample surface. The tunneling current is proportional to the number of state belonging to the sample surface within the energy window defined by eV. These states are responsible for the tunneling current. The number of these states depends on the nature of the sample surface: it is finite for metals and very small or zero for semiconductors and insulators. By including all the sample states in the energy interval eV, the tunneling current becomes

$$I \propto \sum_{E_n=E_F-eV}^{E_F} |\psi_n(0)|^2 e^{-2\kappa W}. \tag{1.29}$$

If V is small enough for the density of states not to change significantly, the Eq. 1.29 can be written in terms of local density of states (LDOS) at the Fermi level. The

LDOS $\rho_S(z, E)$ of the sample at location z and energy ϵ is defined as

$$\rho_S(z, E) \equiv \frac{1}{\epsilon} \sum_{E_n=E-\epsilon}^{E} |\psi_n(z)|^2, \tag{1.30}$$

for a sufficiently small ϵ. The tunneling current can then be recast in terms of the LDOS of the sample

$$I \propto V \rho_S(0, E_F) e^{-2\kappa W}. \tag{1.31}$$

The dependence of the logarithm of the tunneling current with respect to the tip-sample distance is a measure of the work function ϕ, or of the (apparent) tunneling barrier height [68, 69]. From Eq. 1.31

$$\phi = \frac{\hbar^2}{8m} \left(\frac{d\ lnI}{dW} \right)^2. \tag{1.32}$$

By combining Eq. 1.25 and Eq. 1.30 at the postion $z = W$ corresponding to the tip surface, the following expression can be derived

$$\sum_{E_F-eV}^{E_F} |\psi(0)|^2 e^{-2\kappa W} \equiv \rho_S(W, E_F) eV. \tag{1.33}$$

This let us write the tunneling current as

$$I \propto \rho_S(W, E_F) V. \tag{1.34}$$

A topographic STM image is obtained by scanning the STM tip over the surface, keeping constant the tunneling current. According to this one-dimensional model it corresponds to a constant LDOS contour of the sample surface at the Fermi level [60]. This model has been proven to be valid at low bias, at least in first approximation, whenever the length scale of the surface features of interest is much larger than a characteristic length defined as $\pi/\kappa \approx 3$Å [70].

1.3.3 Bardeen model

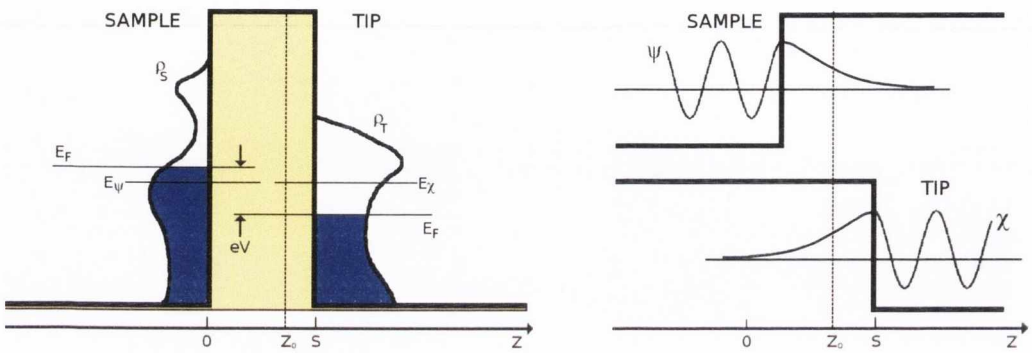

Figure 1.12: In the Bardeen approach the two subsystems are calculated separately. The tunneling current is obtained through the overlap of the wavefunctions of the free systems (b), using the Fermi golden rule. (a): schematic representation of the density of states of the tip and the sample.

A further advancement in the development of the theory of STM has been taken with the time-dependent perturbation approach to the metal-insulator-metal tunneling junction due to Bardeen [71]. The Bardeen approach considers the electronic states of two separate sub-systems, obtained by solving the stationary Schrödinger equation, instead of considering the combined system [Fig. 1.12(a)]. Time-dependent perturbation theory is used to determine the probability of an electron to be transferred from one electrode to the other. The tunneling matrix element M, accounting for the electron transfer, is determined by the overlap of the surface wave function of the two subsystems at a separation surface [Fig. 1.12(b)]. It is then determined by a surface integral on an arbitrary surface placed between the two electrodes, $z = z_0$

$$M = \frac{\hbar^2}{2m} \int_{z=z_0} \left(\chi^* \frac{\partial \psi}{\partial z} - \psi \frac{\partial \chi^*}{\partial z} \right) dS, \tag{1.35}$$

where ψ and χ are the wave functions of the two electrodes. The rate of electron transfer is then determined by the Fermi golden rule [72]. The probability w of an electron in the state ψ with energy E_ψ to tunnel to a state χ with energy E_χ is given

by

$$w = \frac{2\pi}{\hbar}|M|^2\delta(E_\psi - E_\chi). \tag{1.36}$$

The δ-function indicates that the tunneling between the electrodes can happen only between states with the same energy. At any finite temperature, the occupation of the energy levels is given by the Fermi distribution. The tunneling current, at a bias voltage V, can thus be obtained by summing over all the relevant states

$$I = \frac{4\pi e}{\hbar}\int_{-\infty}^{\infty}[f(E_F - eV + \epsilon) - f(E_F + \epsilon)] \times \rho_S(E_F - eV + \epsilon)\rho_T(E_F + \epsilon)|M|^2 d\epsilon, \tag{1.37}$$

where

$$f(E) = \frac{1}{1 + e^{\left[\frac{(E-E_F)}{k_B T}\right]}}, \tag{1.38}$$

is the Fermi distribution function, and ρ_S and ρ_T are the density of states of the two electrodes (the sample and the tip). If $k_B T$ is smaller than the required energy resolution, then the Fermi distribution can be approximated by a step function and the tunneling current can be written as

$$I = \frac{4\pi e}{\hbar}\int_0^{eV} \rho_S(E_F - eV + \epsilon)\rho_T(E_F + \epsilon)|M|^2 d\epsilon. \tag{1.39}$$

By assuming that the magnitude of the tunneling matrix element $|M|$ does not change appreciably in the energy interval of interest, then the tunneling current is determined by the convolution of the DOS of the two electrodes [71, 73]

$$I \propto \int_0^{eV} \rho_S(E_F - eV + \epsilon)\rho_T(E_F + \epsilon) d\epsilon. \tag{1.40}$$

According to the Bardeen formula, the electronic structure of the electrodes enters the Eq. 1.40, through the DOS ρ_S and ρ_T in a symmetric way. Both electrodes equally contribute to the tunneling current, as verified in the classic junction experiment by

Giaever *et al.* [74, 75].

By requiring the tip to have a constant DOS, the DOS of the sample can be recovered by performing a STS experiment, where the differential conductance dI/dV is measured. In this case it is proportional to the DOS of the sample

$$\frac{dI}{dV} \propto \rho_S(E_F - eV). \tag{1.41}$$

1.3.4 Tersoff-Hamann model

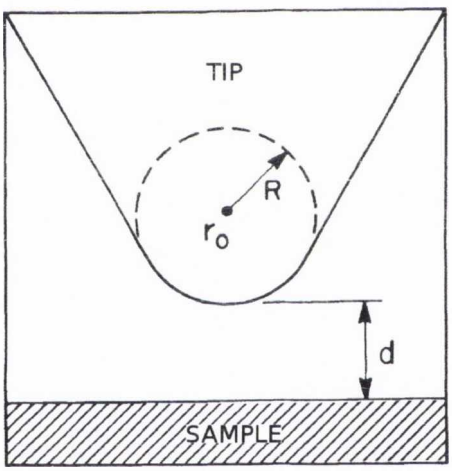

Figure 1.13: S-wave tip model in the Tersoff-Hamann description (figure from ref. [70]). The tip is modeled as a spherical potential well of radius R at distance d from the sample. Only the s-wave solution of the spherical potential well problem is considered as tip wave function.

Another step forward in the theoretical description of the unprecedented atomic resolution achieved by STM experiments was achieved with the work of Tersoff and Hamann [70, 76]. They introduced the spherical tip model, or s-wave-tip model, where the tip is modeled with a spherical shape and the tip wave function is taken as the solution of the Schrödinger equation for a spherical potential well of radius R. Under the assumption that only the s-wave solution is important for this particular problem, the tunneling current at low bias is proportional to the Fermi level DOS at

the center of curvature r_0 of the tip

$$I \propto \sum_{E_\mu = E_F - eV}^{E_F} |\psi_\mu(r_0)|^2 = eV\rho_S(r_0, E_F). \tag{1.42}$$

In the s-wave model, the constant current STM image is a Fermi level LDOS contour of the bare surface, taken at the center of curvature r_0 of the tip. The advantage of this model is that the tip properties can be taken out of the problem and the STM images reflect the properties of the sample only (rather than those of the combined tip/sample system). For free-electron metals, the Fermi level LDOS and the surface charge density contours at a distance from the surface in first approximation coincide, so that the STM images are simply the surface charge density contours [60, 70, 76].

An alternative approach based on the free-electron tip was developed by Stoll [77, 78]. In this the tunneling current is calculated using a scattering method.

1.3.5 Chen extension to the Tersoff-Hamann model

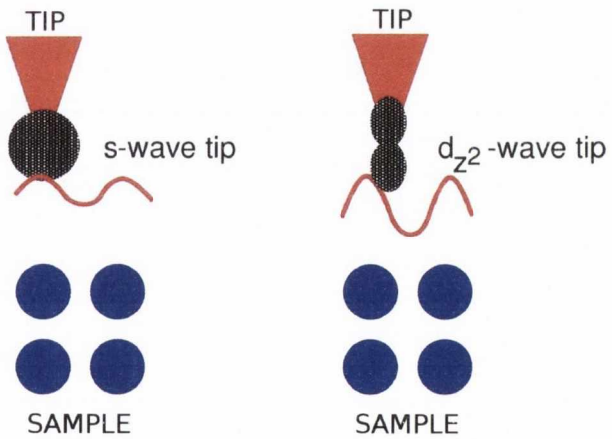

Figure 1.14: Schematic picture of the increased corrugation amplitude obtained by taking in account a d_{z^2} tip state, compared to the s-wave model.

An extension to the Tersoff-Hamann model was proposed by Chen [60, 79, 80] by taking into account more directional tip-states like the d_{z^2} or the p_z states pointing towards the sample. Chen's formalism gives a simple dependence of the matrix

tip state	$M_{\mu\nu} \propto$
s	$\psi^S(r_0)$
$p_i,\ i = x, y, z$	$\frac{\partial}{\partial i}\psi^S(r_0),\ i = x, y, z$
$d_{z^2-\frac{r^2}{3}}$	$\left(\frac{\partial^2}{\partial z^2} - \frac{\kappa_\mu^2}{3}\right)\psi^S(r_0)$

Table 1.1: Matrix elements $M_{\mu\nu}$ within the Chen model. The prefactors depend on the tip state.

element $M_{\mu\nu}$ from the tip orbital. The sample wave functions have the form

$$\psi_\mu^S \propto e^{\kappa_\mu z}, \tag{1.43}$$

where z is the coordinate perpendicular to the sample surface and κ_μ is the vacuum decay constant. The matrix element $M_{\mu\nu}$ is still proportional to the sample wave function at the position of the tip, through a prefactor that depends on the type of orbital used for the tip state (see table 1.1). The inclusion of the tip states into the model explains the high corrugation amplitude observed experimentally. This quantity is underestimated in the Tersoff-Hamann model.

1.3.6 Soler model

The models described so far are independent of the geometrical shape and the composition of the tip. This is not a major issue when the experiments are highly reproducible. However, the information conveyed by the experimental data is much more rich and complex than the picture of this approximation and they involve the convolution of both sample and tip states. In fact, depending on the system and the conditions under investigation, the tip cannot be considered in equilibrium, due to uncontrolled tip-sample interactions or eventual contacts with the surface that could entirely modify its structure. These uncertainties are crucial in the case of STS measurements, where slight changes in the tip can produce a completely different spectra. As a final consequence, it is common that experiments have a low

experimental reproducibility, and that conclusions from a direct observation of the experimental information could not be soundly extracted in all circumstances. A careful comparison with first-principles simulations, in which multiple configurations of the tip are employed, can provide a strategy to gain insight in the interpretation of measurements. The method developed by Soler *et al.* [81] consists in performing first-principles simulations for a given sample and several tip compositions or structures by incorporating the band structure of tip and sample at the same level of theory, using density-functional theory (DFT). The scheme is based on the Bardeen model described in section 1.3.3. The tunneling current, on the basis of the Fermi's golden rule, can be expressed as

$$I = \frac{2\pi e}{\hbar} \sum_{\chi,\psi} [f(E_\chi) - f(E_\psi)] \, |M_{\chi\psi}|^2 \delta(E_\chi - E_\psi + eV), \tag{1.44}$$

where $f(E_j)$ is the Fermi-Dirac function, the energies E_j, $(j = \chi, \psi)$, are referred to the Fermi levels of the tip and the sample, respectively and V is the applied bias voltage between the electrodes. The Bardeen matrix element $M_{\chi\psi}$ couples the states χ (with energy E_χ) and ψ (with energy E_ψ) of tip and sample, respectively, considered as isolated systems. It takes the form

$$M_{\chi\psi} = -\frac{\hbar^2}{2m} \int_\Sigma [\chi^*(\mathbf{r}) \nabla\psi(\mathbf{r}) - \psi(\mathbf{r}) \nabla\chi^*(\mathbf{r})] \cdot d^2(\mathbf{r}), \tag{1.45}$$

where the integral can be calculated over any surface lying in the vacuum region between the two electrodes. Hence the total tunnel current will be a sum over all states in the energy window delimited by the voltage, and under the condition of elastic tunneling, stated by the delta function in Eq. 1.44 [81]. The evaluation of the matrix $M_{\chi\psi}$ can be very demanding because the whole system (tip + sample) has to be included in the simulation cell and $M_{\chi\psi}$ has to be computed for every tip position $\mathbf{R}$. In order to simplify the problem, the Tersoff-Hamann model [70, 76] can applied

and the tip and the sample can be treated as separate sub-systems. Within this model, the potential between the tip and the sample is considered to be constant. It leads to

$$\nabla^2 G_\chi(\mathbf{r}-\mathbf{R}) - \kappa_\chi^2 G_\chi(\mathbf{r}-\mathbf{R}) = -\delta(\mathbf{r}-\mathbf{R}), \qquad \text{with} \qquad \kappa_\chi^2 0 = \frac{2m}{\hbar^2}(\phi_\chi - E_\chi), \quad (1.46)$$

which describes a pointed tip located at $\mathbf{R}$ with a continuous energy spectrum formed by spherically symmetric states. ϕ_χ is the work function of the tip and G_χ is the Green's function of the tip. The solution of Eq. 1.46, satisfying the contour conditions, is of the form

$$G_\chi(\mathbf{r}-\mathbf{R}) = \frac{e^{-\kappa_\chi|\mathbf{r}-\mathbf{R}|}}{4\pi|\mathbf{r}-\mathbf{R}|}. \quad (1.47)$$

The tunneling matrix elements can now be evaluated by using the Green's function of Eq. 1.46 as the tip state, and by applying the Green's theorem afterwards

$$M_{\chi\psi}(\mathbf{R}) = -\frac{\hbar^2}{m}\sqrt{2\pi\kappa_\chi}\int_\Sigma [G^*(\mathbf{r}-\mathbf{R})\nabla\psi(\mathbf{r}) - \psi(\mathbf{r})\nabla G^*(\mathbf{r}-\mathbf{R})]\cdot d^2(\mathbf{r}) = \\ = -\frac{\hbar^2}{m}\sqrt{2\pi\kappa_\chi}\psi(\mathbf{R}). \quad (1.48)$$

The tunneling current reduces to the LDOS of the sample near the Fermi energy and located at the tip position [81]

$$I \propto \int_{E_F}^{E_F+eV} \rho_\psi(\mathbf{R},\epsilon)d\epsilon. \quad (1.49)$$

Alternatively to Eq. 1.48, the value of ψ in the vacuum region can be estimated by propagating the wave functions from the position $\mathbf{r}$ of a surface Σ_ψ, close to the sample, up to the points $\mathbf{r}'$ of another surface Σ_χ, close to the tip (Fig. 1.15). These wave functions are then substituted back in Eq. 1.45 to find more precise values for the matrix elements. A more exhaustive discussion on the method can be found in

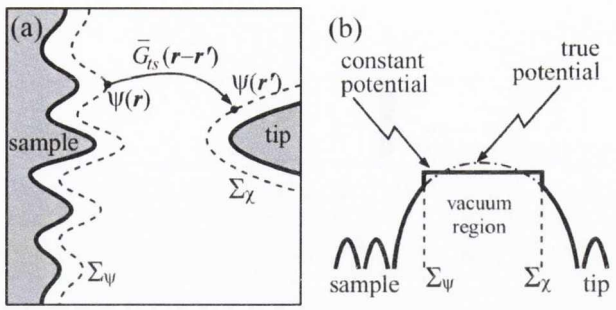

Figure 1.15: (a) A schematic representation of the propagation of $\psi(\mathbf{r})$ values at the mathematical surface Σ_ψ (close to the sample) across the vacuum region up to the points $\mathbf{r}'$ in Σ_χ (close to the tip). (b) The approximation of a flat effective potential in the vacuum region between the tip and the sample (figure from ref. [81]).

Ref. [81].

Further extensions explain the remaining discrepancy between experiments and theory by taking in account, for example, the details of the composition and the geometry of the tip [82–87], the elastic deformation of tip and sample surface in the case of metal surfaces [88, 89], or where a nonperturbative expressions for the tunneling current is adopted [90–104].

1.4 Outline of dissertation

The aim of this work is to investigate several aspects related to the adsorption of hydrogen atoms on an otherwise bare Si(100) surface with $c(4 \times 2)$ reconstruction. The H atom passivates one of the surface dangling bonds leaving a single dangling bond (SDB) on the opposite site of the same dimer. We determine the most favourable bonding configurations of the hydrogen on the surface for the neutral system and for n- and p-doped conditions. We study the charging state of the single dangling bond originating at the site facing the H for different adsorption configurations and as a function of the doping. Afterwards we focus on the confinement effects arising from the potential barriers created by the reacted dimer on the surface and the effect of the aforementioned barriers on the electronic structure of the surface, such as the

formation of standing waves in the conduction band. We analyze the effect that such a barrier has on the adjacent dimer rows of the surface and the possibility of gating effects between rows. The results are obtained by means of *ab initio* computer simulations performed within the density functional theory (DFT) framework and the non-equilibrium Green's function (NEGF) formalism. The calculated results are compared with scanning tunneling microscopy and spectroscopy (STM/STS) data.

The computer simulations done with the SMEAGOL code have been performed by Dr. Ivan Rungger, belonging to the Computational Spintronics Group[1], Trinity College Dublin.

All the experimental measurements have been performed by Dr. Borislav Naydenov, who belongs to the chemistry group lead by Prof. John J. Boland of the Chemistry Department at the Center for Research on Adaptive Nanostructures and Nanodevices[2] (CRANN) in Trinity College Dublin.

The theoretical methods behind the computational work presented in this thesis are described in chapter 2. I will give a brief overview of the approximations that drive us from the unsolvable many-body Schrödinger equation to a set of decoupled, single-particle equations. The Born-Oppenheimer approximation for solids, the classical nuclei approximation and the mean-field approximation are described. The main concepts behind the density functional theory (DFT) follow with a brief review of the most popular implementations of the exchange-correlation functionals which made this method a very practical and powerful tool for predicting the electronic properties of materials. I will introduce the basic concepts of the modern transport theory by starting from a simple toy model for transport and extending the main ideas to more complex systems by making use of the Green's function formalism. A short description of the SMEAGOL code is given at the end of the chapter.

The computational methods involved in the practical solution of the Kohn-Sham

[1]website: www.spincomp.eu
[2]website: www.crann.tcd.ie

equations are presented in chapter 3. The main idea behind the pseudopotential approach is described. This enables us to treat the electron-nucleus interaction in a simplified way. The Bloch's theorem is reported along with the definitions of direct lattice and reciprocal lattice. The plane wave and atom centered basis sets are also dscribed. Some sampling scheme of the Brillouin zone to a finite number of k-points is presented in this chapter along with the supercell approach. Some details about the numerical framework of the *ab initio* DFT-code VASP will be given.

Chapter 4 focuses on the local approach technique used to characterize the bonding configuration of a hydrogen atom on a bare Si(100)-$c(4 \times 2)$ surface and the charging state of the single dangling bond originating from it. The aim of the local approach consists in the description of the electronic and structural properties of the reacted site (dimer) by elaborating the information obtained from *ab initio* calculations and STM/STS experiments around the reacted area. In particular, the charging state of the single dangling bond is studied as a function of the H adsorption configuration and the doping of the sample.

The non-local approach is described in chapter 5. This is a non intrusive method of studying the electronic structure and the geometrical configuration of adsorbates on surfaces. The simulated and measured non-local DOS are used to map the standing waves originated by the presence of adspecies. This technique is used to characterize the adsorption configurations of the H atom and the charging state of the single dangling bond discussed in the previous chapter. Gating effects between adjacent dimer rows, originating from the reacted dimer, are the object of the second part of the chapter.

A very general description of the properties of topological insulators is given in this chapter 6. It is followed by the preliminary results obtained by DFT-based *ab initio* calculations on a heterostructure formed by the topological insulator Bi_2Se_3 epitaxially grown on a graphene substrate. Properties such as the band gap, the band

structure and the spin texturing of the combined system are studied as a function of the distance between the two sub-systems.

CHAPTER 2

Theoretical Framework

2.1 Introduction

In this chapter I describe the theoretical framework behind the methods used in this thesis. The systems of interest in condensed matter physics consist of an ensemble of electrons and nuclei interacting through Coulombic and exchange forces. The exact quantum many-body problem has no analytic solution for systems involving more than two particles and approximations are required. Section 2.2 presents the adiabatic approximation that allows us to decouple the electron motion from the motion of the nuclei and to split the total many-body wavefunction into a product of a wavefunction accounting for the electrons and one accounting for the nuclei. In most of the cases of our interest the exchange effects related to the nuclei are negligible and their wave packets are very localized due to their large masses therefore the nuclei can be treated classically. This is the aim of section 2.3. Due to the two-body nature of the electron-electron interaction, the many-electron wave function,

is still very difficult to treat and this problem can be tackled by introducing the mean-field approximation, described in section 2.4. The basic assumption behind this method is that the electrostatic field felt by an electron in an atom is due to the central potential of the nucleus together with a field (namely, the mean field) created by all the other electrons. As a consequence, the many-electron wave function can be factorized into a product of one-electron orbitals. The main ideas of the density functional theory [105–108], according to the Hohenberg, Kohn and Sham formulation are described in section 2.5. The key concept is that the energy can be written as a functional of the electronic charge density, instead of the many-electrons wave function. In addition, the real system can be mapped into an auxiliary system of non-interacting fermions that can be solved readily and exactly.

Section 2.6 presents a theoretical description of electronic quantum transport starting from a simple molecular toy model, according to the bottom-up approach followed by Datta [109]. The theory will be expanded to more general systems by introducing the Green's function formalism.

Section 2.7 gives a brief description of SMEAGOL, an *ab initio* transport code [110, 111].

2.2 Adiabatic approximation

The physical and chemical properties of a microscopic system of interacting particles, nuclei and electrons, can be described exactly by solving the time-independent many-body Schrödinger equation [112] of the form

$$\hat{H}|\Psi\rangle = E|\Psi\rangle, \tag{2.1}$$

where $\langle \mathbf{r}, \mathbf{R}|\Psi\rangle = \Psi(\mathbf{r};\mathbf{R})$ is the many-body wave function depending on the set of nuclear ($\mathbf{R}$) and electronic ($\mathbf{r}$) coordinates. For a system with N_I nuclei with mass

M_I and atomic number Z_I, and N_e electrons with mass m the Hamiltonian operator is given by

$$\hat{H} = \hat{T}_e(\mathbf{r}) + \hat{T}_N(\mathbf{R}) + \hat{V}_{ee}(\mathbf{r}) + \hat{V}_{NN}(\mathbf{R}) + \hat{V}_{Ne}(\mathbf{r}, \mathbf{R}), \tag{2.2}$$

with

$$\hat{T}_e(\mathbf{r}) = -\sum_{i=1}^{N_e} \frac{\hbar}{2m} \nabla_i^2, \tag{2.3}$$

$$\hat{T}_N(\mathbf{R}) = -\sum_{I=1}^{N_I} \frac{\hbar}{2M_I} \nabla_I^2, \tag{2.4}$$

$$\hat{V}_{ee}(\mathbf{r}) = \frac{1}{2} \sum_{\substack{i,j=1 \\ i \neq j}}^{N_e} \frac{e^2}{|\mathbf{r}_i - \mathbf{r}_j|}, \tag{2.5}$$

$$\hat{V}_{NN}(\mathbf{R}) = \frac{1}{2} \sum_{\substack{I,J=1 \\ I \neq J}}^{N_I} \frac{Z_I Z_J e^2}{|\mathbf{R}_I - \mathbf{R}_J|}, \tag{2.6}$$

$$\hat{V}_{Ne}(\mathbf{r}, \mathbf{R}) = -\frac{1}{2} \sum_{i=1}^{N_e} \sum_{I=1}^{N_I} \frac{Z_I e^2}{|\mathbf{r}_i - \mathbf{R}_I|}. \tag{2.7}$$

Here $T_e(\mathbf{r})$ is the electronic kinetic energy, $T_N(\mathbf{R})$ is the nuclear kinetic energy, $V_{ee}(\mathbf{r})$, $V_{NN}(\mathbf{R})$ and $V_{Ne}(\mathbf{r}, \mathbf{R})$ are the potential energies due, respectively, to the coulombic interaction between the electrons, between the nuclei and between the nuclei and the electrons. ∇_i^2 (∇_I^2) is the Laplacian with respect to the three cartesian coordinates of the i^{th} electron (I^{th} nucleus). Since electrons are fermions, the total electronic wave function must be antisymmetric and it should change sign whenever the coordinates of any two electrons are exchanged. The symmetry properties of the nuclei wave function depend on the nuclear spin: they are fermions for half-integer nuclear spin (e.g. H, ^{3}He) and bosons for integer spin (e.g. ^{4}He, H_2). In principle all the properties of the system can be derived by solving the time-independent Schrödinger equation but, in practice, this problem is almost impossible to treat within a full quantum mechanical framework. A complete analytic solution is only available for hydrogenic atoms or the H_2^+ molecule. Exact numerical solutions are also limited to a few cases,

mostly atoms and small molecules. The most important feature contributing to this difficulty is the two-body nature of the Coulomb interaction that makes the aforementioned Schrödinger equation not separable. Let us consider the case of a single atom with Z electrons. The electron wave function can be, in principle, written as an antisymmetrized product of one-electron wave functions (Slater determinant, [113]). This assumes, however, some kind of separability of the Schrödinger equation, implying that the probability of finding an electron at some point in space is independent of the positions of the other electrons. The electron-electron interaction is quite at odds with this picture, because an electron located at point $\mathbf{r}$ in space precludes other electrons from approaching this location. Hence the probability of finding an electron at point $\mathbf{r}$ depends on the location of the other $Z-1$ electrons. This phenomenon is known as *correlation* and implies that the many-body wave function should depend on two electronic coordinates. This means that the full Schrödinger equation cannot be easily decoupled into a set of single-particle equations. Approximations are required in order to solve the problem [114].

One powerful approximation, called the Born-Oppenheimer [115] approximation, allows the many-body wavefunction of the system to be broken into its electronic and nuclear (vibrational, rotational) components. It relies on the fact that the nuclear mass is ~ 1800 times bigger than the electron mass. Within a classical picture, the velocity of the electrons can be considered much bigger than the one of the nuclei and the motion of electrons and nuclei can be separated. The electrons can be thought of as instantaneously following the motion of the nuclei, while remaining always in the same stationary state of the electronic Hamiltonian. According to this approximation, also called *adiabatic approximation*, the electrons do not undergo transitions between stationary states. In other words, as the nuclei follow their dynamics, the electrons instantaneously adjust their wave function according to the nuclear wave function. Let us consider the case of a molecule, where the electronic

spectrum is discrete. Three basic types of motion can be related to a molecule: electronic, nuclear vibrations and nuclear rotations, each one corresponding to a typical energy scale. The energy scale of the electronic motion is given by the separation between successive electronic eigenstates and it has the same order of magnitutde of the ground state energy. It is approximately given by $E_e \approx \hbar^2/(ma^2)$ where a is the typical interatomic distance in the molecule and it is of the order of few eV. The energy scale of nuclear vibrations is given, in the harmonic approximation, by $E_v = \hbar\omega$ where ω is the frequency of the vibrational motion. In first approximation $E_v = \hbar\omega \approx (m/M)^{1/2}E_e$ with M being the mass of the molecule and m the electron mass. The rotational energy is related to the angular momentum of the molecule and it is quantized in levels separated by $\approx \hbar$ and it is given by $E_r = L^2/I$ where I is the moment of inertia of the molecule. This energy can be approximated as $E_r \approx \hbar^2/(Ma^2) = (m/M)E_e$. Therefore, for the N_2 molecule, for example, the first electronic excitation energy is 7.5 eV, the vibrational excitation energy is around 300 meV and the rotation level separation is around 0.5 meV. It can be noticed that the rotational energy is two order of magnitude smaller than the vibrational energy which is almost two order of magnitude smaller than the elctronic one. This makes reasonable the assumption that no transition between electronic states can be induced by nuclear motion and the error associated to the separation between nuclear and electronic motion is negligible.

In the case of extended systems like crystals, the electronic spectrum is continuous and so is the excitation spectrum. For insulators and semiconductors the smallest electronic excitation is given by the energy band gap which is in the order of few eV. For metallic systems the electronic excitations form a continuum and, strictly speaking, the adiabatic approximation should not be applicable. However, the range between room temperature and a few thousands Kelvin is usually much lower than the electronic Fermi temperature, excitations are confined to a narrow region around

the Fermi surface and most properties are little affected by neglecting non-adiabatic contributions coming from these few electrons. The limits of the adiabatic approximations are reached when the electronic energy scale becomes comparable with the one of the nuclear vibrational motion and nuclei and electrons need to be treated in a unified framework. This can happen when the electronic gap closes due to some external factor like pressure or temperature and whenever electron-phonon interactions are not negligible [114].

The adiabatic separation between electrons and nuclei can be cast in a formal mathematical framework by decomposing the original wave function Ψ into a product between an electronic wave function $\Psi_{el}(\mathbf{r};\mathbf{R})$ which depends parametrically from the nuclear coordinates, and a nuclear wave function $\Phi_{nuc}(\mathbf{R})$

$$\Psi(\mathbf{r};\mathbf{R}) = \Psi_{el}(\mathbf{r};\mathbf{R})\Phi_{nuc}(\mathbf{R}). \tag{2.8}$$

The electronic part of the Schrödinger equation becomes

$$\left[-\sum_{i=1}^{N_e} \frac{\hbar}{2m}\nabla_i^2 - \frac{1}{2}\sum_{I=1}^{N_I}\sum_{i=1}^{N_e} \frac{Z_I e^2}{|\mathbf{r}_i - \mathbf{R}_I|} + \frac{1}{2}\sum_{\substack{i,j=1 \\ i\neq j}}^{N_e} \frac{e^2}{|\mathbf{r}_i - \mathbf{r}_j|} \right] \Psi_{el} = E_{el}(\mathbf{R})\Psi_{el}. \tag{2.9}$$

The nuclear motion is governed by the nuclear Schrödinger equation, where the ground state electronic energy E_{el} enters the potential energy expression

$$\left[-\sum_{I=1}^{N_I} \frac{\hbar}{2M}\nabla_I^2 + \frac{1}{2}\sum_{\substack{I,J=1 \\ I\neq J}}^{N_I} \frac{Z_I Z_J e^2}{|\mathbf{R}_I - \mathbf{R}_J|} + E_{el}(\mathbf{R}) \right] \Phi_{nuc} = E\Phi_{nuc}. \tag{2.10}$$

When separating the nuclear from the electronic contribution, the (non-adiabatic) dynamical term deriving from the action of the nuclear kinetic operator on the electronic wave funcstion has been neglected. The related error should be of the same

order of magnitude of the rate m_e/M_I between the effective mass of the electron and the mass of the nucleus and it is negligible everytime there is no strong electron-phonon coupling.

2.3 Classical nuclei approximation

According to the adiabatic approximation the total wave function can be written in the form given in Eq. (2.8) where $\Phi_{nuc}(\mathbf{R})$ is the nuclear wavefunction. Atomic nuclei exhibit exchange effects only at very low temperature and nuclear wave packets are quite localized due to the large nuclear masses. These two observations enable us to conclude that, in most of the cases, a classical treatment of the atomic nuclei is justified. The dynamics of the mean values of the position $\mathbf{R}$ and momentum $\mathbf{P}$ operators can be then obtained from Ehrenfest's theorem [116]

$$i\hbar\frac{d\langle\mathbf{R}\rangle}{dt} = \langle[\hat{H},\mathbf{R}]\rangle = i\hbar\frac{\langle\mathbf{P}\rangle}{M} \Rightarrow M\frac{d\langle\mathbf{R}\rangle}{dt} = \langle\mathbf{P}\rangle, \tag{2.11}$$

$$i\hbar\frac{d\langle\mathbf{P}\rangle}{dt} = \langle[\hat{H},\mathbf{P}]\rangle = -i\hbar\langle\nabla E_n(\mathbf{R})\rangle, \tag{2.12}$$

where the brackets $\langle\rangle$ indicate the expectation values (mean values) of the operators (e.g. $\langle\mathbf{R}\rangle = \langle\Psi|\mathbf{R}|\Psi\rangle$). The Newtonian equation of motion is obtained by combining the two equations

$$M\frac{d^2\langle\mathbf{R}\rangle}{dt^2} = -\langle\nabla E_n(\mathbf{R})\rangle. \tag{2.13}$$

The *classical nuclei approximation* consists in identifying the mean value of the position operator with the cartesian coordinates of the classical particle. This can be understood if the nuclear wave function is represented as a product of Dirac's δ-functions centered at the classical positions. Therefore, the equations of motion become

$$M\frac{d^2\mathbf{R}}{dt^2} = -\nabla E_n(\mathbf{R}), \tag{2.14}$$

where $E_n(\mathbf{R})$ is the n-th adiabatic potential energy surface[1]. The final expression for the equation of motion is obtained by using the Hellmann-Feynman theorem [117, 118], which states that the variation of the electronic energy with respect to an external parameter ($\mathbf{R}$ in this case) coupled to the electronic variables can be calculated as the expectation value of the variation of the Hamiltonian

$$\frac{\partial E_n(\mathbf{R})}{\partial \mathbf{R}} = \langle \Psi_n(\mathbf{R}) \left| \frac{\partial \hat{H}(\mathbf{R})}{\partial \mathbf{R}} \right| \Psi_n(\mathbf{R}) \rangle, \tag{2.15}$$

and hence

$$M\frac{d^2\mathbf{R}}{dt^2} = -\langle \Psi_n(\mathbf{R}) \left| \frac{\partial \hat{H}_{el}(\mathbf{R})}{\partial \mathbf{R}} \right| \Psi_n(\mathbf{R}) \rangle - \frac{\partial \hat{V}_{NN}(\mathbf{R})}{\partial \mathbf{R}}, \tag{2.16}$$

where $\mathbf{R}$ represents the classical nuclear configuration with

$$\hat{H}_{el} = \hat{T}_e(\mathbf{r}) + \hat{T}_N(\mathbf{R}) + \hat{V}_{ee}(\mathbf{r}) + \hat{V}_{Ne}(\mathbf{r}, \mathbf{R}) \tag{2.17}$$

and $\hat{V}_{NN}$ is given by the equation (2.6). The solution of the stationary problem, i.e. $\nabla E_n(\mathbf{R}) = 0$ is known as *geometry optimization* and it is as important as the determination of the dynamical evolution of the system. In order to obtain $E_n(\mathbf{R}) = 0$ and its gradient it is necessary to solve the time-independent Schrödinger equation. This is called an electronic structure calculation [114]. For a deeper understanding of the topic see Ref. [119, 120].

2.4 The many-body problem and the mean-field approximation

The electronic Schrödinger equation for a system of N_e interacting electrons under the effect of an external Coulomb potential generated by a collection of N_I atomic

[1]The total energy of an atom arrangement can be represented as a curve or (multidimensional) surface, with atomic positions as variables.

nuclei can be written as:

$$\hat{H}_{el}|\Psi_{el}(\mathbf{r};\mathbf{R})\rangle = E_{el}(\mathbf{R})|\Psi_{el}(\mathbf{r};\mathbf{R})\rangle \tag{2.18}$$

where $\Psi_{el}(\mathbf{r};\mathbf{R})$ is the many-electron wave function and $E_{el}(\mathbf{R})$ are the eigenvalues. Both Ψ_{el} and E_{el} depend parametrically on the nuclear coordinates $\mathbf{R}$. The electronic Hamiltonian is given by

$$\hat{H}_{el} = \left[-\sum_{i=1}^{N_e} \frac{\hbar}{2m}\nabla_i^2 - \frac{1}{2}\sum_{I=1}^{N_I}\sum_{i=1}^{N_e} \frac{Z_I e^2}{|\mathbf{r}_i - \mathbf{R}_I|} + \frac{1}{2}\sum_{\substack{i,j=1 \\ i\neq j}}^{N_e} \frac{e^2}{|\mathbf{r}_i - \mathbf{r}_j|} \right] \Psi_{el} = E_{el}(\mathbf{R})\Psi_{el}. \tag{2.19}$$

The main difficulty in solving this equation arises from the two-body term describing the electron-electron Coulomb interaction

$$\hat{V}_{ee}(\mathbf{r}) = \frac{1}{2}\sum_{\substack{i,j=1 \\ i\neq j}}^{N_e} \frac{e^2}{|\mathbf{r}_i - \mathbf{r}_j|}, \tag{2.20}$$

which prevents the many-electron wave function to be written as a product of single-particle wave functions. This problem is known as the *many-body* problem and is intrinsically related to the two-body nature of the electron-electron interaction. The presence of an electron in a region of space influences the behaviour of all the other electrons of the system so that they cannot be considered as individual entities. Developing approximate schemes to solve this problem is worthwhile because the knowledge of the electronic structure of a system gives access to all its physical and chemical properties. The electronic ground state determines the atomic structure of the system, the relative stability of different structures, polarizabilities and dielectric properties *etc.* In order to be able to factorize the many-electron wave function, the *mean-field* approximation is introduced. This takes from an original work by Hartee and Slater, who gave a mathematical groundwork to the method [121, 122]. The

basic assumption is that the electrostatic field felt by an electron in an atom is due to the central potential of the nucleus together with a field (mean field) created by all the other electrons. As a consequence, the many-electron wave function can be written as a product of one-electron orbitals. The electron-electron interaction term can be written as:

$$V_{ee}(\mathbf{r}) = \sum_{i=1}^{N_e} V(\mathbf{r_i}) \quad \text{with} \quad V(\mathbf{r_i}) = \sum_{\substack{j=1 \\ j \neq i}}^{N_e} \frac{e^2}{|\mathbf{r_i} - \mathbf{r_j}|}. \tag{2.21}$$

By replacing $V(\mathbf{r_i})$ with an appropriate effective value

$$V(\mathbf{r_i}) = \left\langle \sum_{\substack{j=1 \\ j \neq i}}^{N_e} \frac{e^2}{|\mathbf{r_i} - \mathbf{r_j}|} \right\rangle = V^{eff}(\mathbf{r}) \tag{2.22}$$

it is possible to factorize the many-body electron wave function Ψ_{el} in a product of single-particle wave functions (Hartree approximation)

$$\Psi_{el}(\mathbf{r_1}, \mathbf{r_2}, ..., \mathbf{r_n}) = \psi(\mathbf{r_1})\psi(\mathbf{r_2}), ..., \psi(\mathbf{r_n}). \tag{2.23}$$

Thus a set of decoupled single-particle equations are obtained. Each single-particle wave function depends on 3 independent spatial coordinates, hence the determination of the properties of the system imply the solution of a set of $3N_e$ unknowns, N_e being the total number of electrons. In order to take in account the antisymmetry postulate of the wave function, the simple product of wave functions is replaced by a Slater determinant and the Hartree-Fock equations are obtained [123]. These equations involve a quantistic non-local term in the Hamiltonian, called exchange energy. The contribution to the total energy given by the exchange energy can be written as

$$E_{exchange} = -\frac{e^2}{2} \sum_{\substack{i,j=1 \\ i \neq j}}^{N_e} \int\int d\mathbf{r} d\mathbf{r}' \psi_i^*(\mathbf{r}) \psi_j^*(\mathbf{r}') \frac{1}{|\mathbf{r} - \mathbf{r}'|} \psi_i(\mathbf{r}') \psi_j(\mathbf{r}) \delta_{\sigma_i \sigma_j}. \tag{2.24}$$

The Hartree-Fock equations account for the quantistic interaction between electrons with the same spin, through the exchange term, but a term accounting for the correlation between electrons with opposite spin is missing. For this reason, the Hartree-Fock approximation works very well when the correlations effects are small or negligible while it fails in predicting properties where many-body effects are present.

2.5 Density Functional Theory

Density functional theory, known as DFT [105–108], which was developed by Hohenberg, Kohn and Sham in 1964, is based on the concept that the total energy of an electronic system can be written as a functional of the electronic charge density, instead of the many-electron wave function. The main theorem at the base of the theory states that the ground state charge density determines all the properties that can be extracted from the Hamiltonian by solving the Schrödinger equation. This confers a great advantage, as it enable us to describe the system with only 3 coordinates needed to describe the charge density ρ, instead of the $3N_e$ coordinates, needed to describe the many-body wave function Ψ. In the case of a non-degenerate, non-spin polarized system of N_e electrons

$$\Psi(\mathbf{r}_1, \mathbf{r}_2, ..., \mathbf{r}_n) \rightarrow \rho(\mathbf{r}) \qquad \Rightarrow \qquad 3N_e \text{ coordinates } \rightarrow \text{ 3 coordinates} \tag{2.25}$$

$$\rho(\mathbf{r}) = N \int \Psi^*(\mathbf{r}, \mathbf{r}_2, ..., \mathbf{r}_n)\Psi(\mathbf{r}, \mathbf{r}_2, ..., \mathbf{r}_n)\, d\mathbf{r}_2\, d\mathbf{r}_3 \ldots d\mathbf{r}_n. \tag{2.26}$$

2.5.1 Hohenberg and Kohn theory

Within the Born-Oppenheimer approximation [115], the time-independent Schrödinger equation for a system of interacting fermions is given by

$$\hat{H}|\Psi\rangle = E|\Psi\rangle, \tag{2.27}$$

where the Hamiltonian is

$$\hat{H} = \hat{T}_e + \hat{V}_{ext} + \hat{V}_{ee} \qquad \text{with} \qquad \hat{V}_{ext} = \sum_{i=1}^{n} v_{ext}(\mathbf{r_i}), \tag{2.28}$$

and V_{ext} is the external potential that can be written as a sum of single-particle potentials $v_{ext}(\mathbf{r_i})$ (e.g. of the form given in Eq. 2.7). The Hohenberg and Kohn theorem [105, 108] states that:

"the external potential is univocally determined by the electronic density, up to a trivial additive constant".

As a corollary, since the ground state charge density, $\rho_{GS}(\mathbf{r})$, univocally determines V_{ext}, it also determines the ground state wavefunction Ψ_{GS}, which should be otherwise obtained by solving the full many-body Schrödinger equation. The proof of the theorem shows the existence of a one-to-one invertible correspondence between the ground state many-body wavefunction Ψ_{GS} and the external potential V_{ext}. Moreover, it shows a one-to-one correspondence between Ψ_{GS} and the ground state charge density ρ_{GS}

$$V_{ext} \Leftrightarrow \Psi_{GS}, \quad \Psi_{GS} \Leftrightarrow \rho_{GS} \quad \Rightarrow \quad \rho_{GS} \rightarrow |\Psi[\rho_{GS}]\rangle \rightarrow V_{ext}[\rho_{GS}]. \tag{2.29}$$

The most important consequence of the Hohenberg and Kohn theorem is that, at least in principle, the expectation value on the ground state of each operator $\hat{O}$ is an unique functional of the exact ground state density ρ_{GS}

$$\langle \Psi[\rho_{GS}]|\hat{O}|\Psi[\rho_{GS}]\rangle = O[\rho_{GS}]. \tag{2.30}$$

In addition to the first theorem proving the existence of the functional, Hohenberg

e Kohn showed its variational nature

$$E_{V_{ext}}[\rho] = \langle \Psi[\rho] | \hat{T}_e + \hat{V}_{ee} + \hat{V}_{ext} | \Psi[\rho] \rangle, \tag{2.31}$$

where $\hat{V}_{ext}$ is the external potential of a system with ground state density $\rho_{GS}(\mathbf{r})$ and energy E_{GS}. The wave functions Ψ_{GS} and $\rho_{GS}(\mathbf{r})$ can be obtained by minimizing the energy functional through a trial density ρ, according to the Hohenberg and Kohn minimum principle

$$E_{GS} := E_{V_{ext}}[\rho_{GS}] = \min_{\rho \in \Lambda} E_{V_{ext}}[\rho], \tag{2.32}$$

where Λ is the totality of all the n-particles integrable charge densities. The minimization procedure of the charge density is performed over 3 coordinates instead of the $3N_e$ needed for minimizing the wave function. By considering the independent contributions

$$E_{V_{ext}}[\rho] = F_{HK}[\rho] + \int d\mathbf{r}\, \rho(\mathbf{r}) V_{ext}(\mathbf{r}), \tag{2.33}$$

the functional

$$F_{HK}[\rho] = \langle \Psi[\rho] | \hat{T}_e + \hat{V}_{ee} | \Psi[\rho] \rangle, \tag{2.34}$$

is a universal functional of the charge density ρ and it does not depend on $\hat{V}_{ext}$. Given the differentiability of $E_{V_{ext}}(\rho)$, the variational principle can be written as a stationarity principle of the energy functional with respect to charge density variations that keep constant the total number of electrons N_e

$$\frac{\delta}{\delta \rho} \left(E_{V_{ext}}[\rho] - \mu \int d\mathbf{r}\, \rho(\mathbf{r}) \right) = 0. \tag{2.35}$$

From Eq.(2.35) the Euler-Lagrange equation can be obtained

$$\frac{\delta E_{V_{ext}}[\rho]}{\delta \rho(\mathbf{r})} = \frac{\delta F_{HK}[\rho]}{\delta \rho(\mathbf{r})} + V_{ext}(\mathbf{r}) = \mu. \tag{2.36}$$

The Lagrange multiplier μ, which is relative to the constraint on the number of electrons N_e, expresses the chemical potential (thermodynamical extension of DFT) [124]. The explicit form of the kinetic and the electron-electron functionals entering the expression of $F_{HK}[\rho(\mathbf{r})]$ given by Eq.(2.34) is not known. If good approximations to these functionals could be found, than a direct minimization of the energy functional would be possible. Kohn and Sham [106, 107] proposed a scheme to approximate the kinetic and electron-electron functionals. It consists of an auxiliary system of non-interacting particles to be described by a single determinant function, whose charge density equals the one of the "real" interacting system. The universal functional $F_{HK}[\rho(\mathbf{r})]$ of the fictitious system can then be calculated from the orbitals because it corresponds to the kinetic energy of the system of non-interacting particles

$$F_{HK}[\rho(\mathbf{r})] = T_{KS}[\rho(\mathbf{r})]. \tag{2.37}$$

2.5.2 Kohn and Sham equations

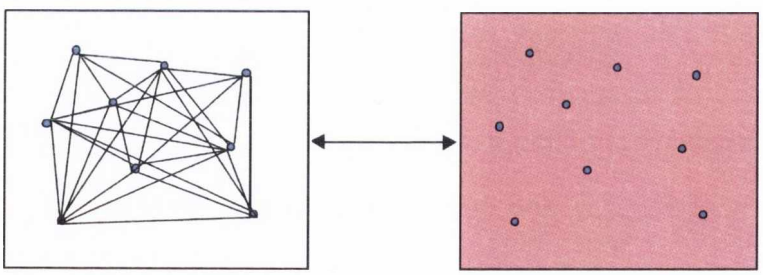

Figure 2.1: A cartoon representing the relationship between the "real" many-body system (left-hand side) and the non-interacting system of Kohn-Sham density functional theory (right-hand side).

Kohn and Sham equations [106–108] provide a practical scheme to solve the Hohenberg and Kohn theory and became a very powerful tool for investigating the physics related to atoms, molecules and solids. The main idea originates from the observation that a system of non-interacting electrons can be exactly described by an antisymmetric wave function of the Slater determinant type, made of one-electron

orbitals. According to the Hartree-Fock theory, the kinetic energy for such a system can be easily expressed in terms of one-electron orbitals

$$T = -\frac{\hbar^2}{2m}\sum_{i=1}^{\infty} f_i \langle \phi_i | \nabla^2 | \phi_i \rangle, \tag{2.38}$$

where ϕ_i are the one-electron orbitals and f_i the corresponding occupation numbers ($f_i = 0, 1$). The strategy proposed by Kohn and Sham consists in finding a system of non-interacting electrons that produces the same electronic density of the interacting system and use the equation (2.38) to calculate exactly the kinetic energy. This is not, of course, the kinetic energy of the interacting system: the missing fraction is due to the fact that the true many-body wave function is not a single Slater determinant. As such there is a kinetic correlation contribution, which needs to be included in the correlation energy term. The energy functional for a system of N_e non-interacting fermions, described by the Hamiltonian $\hat{H}_{KS} = \hat{T}_{KS} + \hat{V}_{KS}$, can be written as

$$E_{KS}[\rho] = T_{KS}[\rho] + \int d\mathbf{r}\, V_{KS}(\mathbf{r})\rho(\mathbf{r}), \tag{2.39}$$

according to the Hohenberg and Kohn theory. $T_{KS}[\rho]$ is the kinetic energy functional of the ground state of non-interacting particles with charge density ρ, and external potential V_{KS}. The exact ground state density ρ_{KS}, linked to the Hamiltonian $\hat{H}_{KS}$, is obtained by applying the Hohenberg and Kohn variational principle

$$\frac{\delta E_{KS}[\rho]}{\delta \rho(\mathbf{r})} = \frac{\delta T_{KS}[\rho]}{\delta \rho(\mathbf{r})} + V_{KS}(\mathbf{r}) - \varepsilon = 0. \tag{2.40}$$

The Kohn and Sham scheme is based on the assumption that, for each system of interacting particles, a local potential $V_{KS}(\mathbf{r})$ can be determined in such a way that the ground state charge density $\rho_{KS}(\mathbf{r})$ of the non-interacting system under the influence of the potential $V_{KS}(\mathbf{r})$, equals the charge density of the interacting system

$\rho(\mathbf{r})$. If $\hat{H}_{KS}$ is not degenerate, the charge density expression for the non-interacting system is unique

$$\rho_{KS}(\mathbf{r}) = \rho(\mathbf{r}) = \sum_{i=1}^{n} |\phi_i(\mathbf{r})|^2. \tag{2.41}$$

The eigenfunctions $\phi_i(\mathbf{r})$ and the eigenvalues ε_i can be obtained from a Schrödinger-like equation

$$\left(-\frac{\hbar^2}{2m}\nabla^2 + V_{KS}(\mathbf{r})\right)\phi_i(\mathbf{r}) = \varepsilon_i\,\phi_i(\mathbf{r}), \qquad \varepsilon_1 \leq \varepsilon_2 \leq ... \leq \varepsilon_n. \tag{2.42}$$

Once the potential $V_{KS}(\mathbf{r})$ is known for $\rho(\mathbf{r})$, the Hohenberg and Kohn theorem guarantees its uniqueness. $V_{KS}(\mathbf{r})$ univocally determines the single-particle orbitals which are unique functionals of the charge density: $\phi_i(\mathbf{r}) = \phi_i(\rho, \mathbf{r})$. The kinetic energy of the non-interacting system is itself a unique functional of the charge density $\rho(\mathbf{r})$

$$T_{KS}[\rho] = \sum_{i=1}^{n} \int d\mathbf{r}\,\phi_i^*(\mathbf{r})\left(-\frac{\hbar^2}{2m}\nabla^2\right)\phi_i(\mathbf{r}). \tag{2.43}$$

The universal functional $F_{HK}[\rho]$ for the interacting system can be written as

$$F_{HK}[\rho] \equiv T_{KS}[\rho] + \frac{e^2}{2}\int\int \frac{\rho(\mathbf{r})\rho(\mathbf{r}')}{|\mathbf{r}-\mathbf{r}'|} d\mathbf{r}\,d\mathbf{r}' + E_{xc}(\rho), \tag{2.44}$$

where $E_{xc}[\rho]$ is the exchange-correlation energy given by

$$E_{xc}[\rho] \equiv F_{HK}[\rho] - T_{KS}[\rho] - \frac{e^2}{2}\int\int \frac{\rho(\mathbf{r})\rho(\mathbf{r}')}{|\mathbf{r}-\mathbf{r}'|} d\mathbf{r}\,d\mathbf{r}'. \tag{2.45}$$

The exchange-correlation energy $E_{xc}[\rho]$ includes the quantistic (non Coulombic) contribution of the electron-electron interaction and the difference between the kinetic energies of the interacting and the non-interacting systems. The energy functional

for the interacting system then becomes

$$E_{V_{ext}}[\rho] = T_{KS}[\rho] + \int d\mathbf{r}\, V_{ext}(\mathbf{r})\rho(\mathbf{r}) + \frac{e^2}{2}\int\int \frac{\rho(\mathbf{r})\rho(\mathbf{r}')}{|\mathbf{r}-\mathbf{r}'|} d\mathbf{r}\, d\mathbf{r}' + E_{xc}(\rho) \geq E_0. \quad (2.46)$$

From the Hohenberg and Kohn minimization principle, the Euler-Lagrange equations can be obtained (N_e fixed)

$$\delta E_{V_{ext}}[\rho] = \int d\mathbf{r}\, \delta\rho(\mathbf{r}) \left\{ V_{eff}(\mathbf{r}) + \left.\frac{\delta T_{KS}[\rho]}{\delta\rho}\right|_{\rho_0} - \epsilon \right\} = 0, \quad (2.47)$$

where the effective potential $V_{eff}(\mathbf{r})$ is given by

$$V_{eff}(\mathbf{r}) \equiv V_0(\mathbf{r}) + e^2 \int d\mathbf{r}' \frac{\rho(\mathbf{r}')}{|\mathbf{r}-\mathbf{r}'|} + V_{xc}(\rho_0, \mathbf{r}) \quad (2.48)$$

and

$$V_{xc}(\rho_0, \mathbf{r}) \equiv \left.\frac{\delta E_{xc}[\rho]}{\delta\rho(\mathbf{r})}\right|_{\rho_0}. \quad (2.49)$$

The Euler-Lagrange equations of the interacting system are formally identical to the ones of the non-interacting system, where $V_{eff}(\mathbf{r})$ replaces $V_{KS}(\mathbf{r})$. The charge density $\rho(\mathbf{r})$ minimizing the energy functional can be obtained from the solution of the single-particle Kohn and Sham equations

$$\left(-\frac{\hbar^2}{2m}\nabla^2 + V_{eff}(\mathbf{r})\right)\phi_i(\mathbf{r}) = \varepsilon_i\,\phi_i(\mathbf{r}). \quad (2.50)$$

The final Hamiltonian is that of a non-interacting electrons gas feeling the effective potential $V_{eff}(\mathbf{r})$ and where all the many-body effects of the real system are included. The ground state total energy for the system of interacting particles can be written as:

$$E_{KS} = \sum_{i=1}^{n} \varepsilon_i + E_{xc}[\rho(\mathbf{r})] - \int V_{xc}(\mathbf{r})\rho(\mathbf{r})\, d\mathbf{r} - \frac{e^2}{2}\int \frac{\rho(\mathbf{r})\rho(\mathbf{r}')}{|\mathbf{r}-\mathbf{r}'|}\, d\mathbf{r}\, d\mathbf{r}' + E_{ion}. \quad (2.51)$$

Such an energy functional is expressed in terms of the n orbitals that minimize the non-interacting electronic kinetic energy under the fixed density constraint. The one-electron orbitals are known as Kohn-Sham orbitals and, in principle, they do not have any obvious physical meaning by themselves except for the highest occupied molecular orbital (HOMO). They are the result of a mathematical construction devised to simplify the problem. In practice, it is customary to consider them as single-particle physical eigenstates. The Kohn and Sham scheme allows, in principle, the determination of the exact ground state charge density and the total energy. In practice, the exact expression of the functional $E_{xc}[\rho]$ [with its derivative $V_{xc}(\mathbf{r})$] is not known, and approximations are required. Due to their non-linearity, the Kohn and Sham equations have to be solved through a self-consistent iterative approach.

2.5.3 Spin-polarized systems

The extension of Kohn and Sham equations to spin-polarized systems allows us to investigate systems with open shells and spontaneous ferromagnetic or anti-ferromagnetic ground states [125–128]. The electronic density can be decomposed into two independent spin densities $\rho = \rho_\uparrow + \rho_\downarrow$ and the Kohn-Sham equations can be written independently for each spin component ($\sigma = \uparrow, \downarrow$)

$$\left(-\frac{\hbar^2}{2m}\nabla^2 + V_{KS}^{\sigma}(\mathbf{r})\right)\phi_i^{\sigma}(\mathbf{r}) = \varepsilon_i^{\sigma}\,\phi_i^{\sigma}(\mathbf{r}), \tag{2.52}$$

where

$$V_{KS}^{\sigma}(\mathbf{r}) = V_{ext}(\mathbf{r}) + e^2 \int \frac{\rho(\mathbf{r})}{|\mathbf{r}-\mathbf{r}'|}\, d\mathbf{r}' + V_{xc}^{\sigma}(\mathbf{r}), \tag{2.53}$$

$$V_{xc}^{\sigma}(\mathbf{r}) = \frac{\delta E_{xc}[\rho^{\uparrow}, \rho^{\downarrow}]}{\delta \rho^{\sigma}(\mathbf{r})}, \tag{2.54}$$

$$\rho^{\sigma}(\mathbf{r}) = \sum_i f_i^{\sigma} |\phi_i^{\sigma}(\mathbf{r})|^2, \quad \rho(\mathbf{r}) = \sum_{\sigma} \rho^{\sigma}(\mathbf{r}), \tag{2.55}$$

$$\sum_{i=1}^{\infty} f_i^{\sigma} = n_{\sigma}, \quad n_{\uparrow} + n_{\downarrow} = n. \tag{2.56}$$

Here f_i^{σ} is the occupation number and is assumed to be: 0 for $\varepsilon_i^{\sigma} > \mu^{\sigma}$; 1 for $\varepsilon_i^{\sigma} < \mu^{\sigma}$; in the range [0,1] for $\varepsilon_i^{\sigma} = \mu^{\sigma}$. In the case of non-spin-polarized systems $\rho_{\uparrow} = \rho_{\downarrow}$ spin-polarized DFT (SDFT) reduces to the simpler case of DFT with double occupancies of the single-particle orbitals. In SDFT the total energy is written as

$$E_{KS}[\rho^{\uparrow}, \rho^{\downarrow}] = T_{KS}[\rho^{\uparrow}, \rho^{\downarrow}] + \int \rho(\mathbf{r}) V_{ext}(\mathbf{r}) d\mathbf{r} + \frac{1}{2} \int\int \frac{\rho(\mathbf{r})\rho(\mathbf{r}')}{|\mathbf{r}-\mathbf{r}'|} d\mathbf{r} d\mathbf{r}' + E_{XC}[\rho^{\uparrow}, \rho^{\downarrow}] - \int \rho(\mathbf{r}) \mu_{XC}[\rho^{\uparrow}, \rho^{\downarrow}](\mathbf{r}) d\mathbf{r}, \tag{2.57}$$

with

$$T_{KS}[\rho^{\uparrow}, \rho^{\downarrow}] = -\frac{\hbar^2}{2m} \sum_{\sigma=\uparrow,\downarrow} \sum_{i=1}^{n} \langle \phi_i^{\sigma} | \nabla^2 | \phi_i^{\sigma} \rangle. \tag{2.58}$$

Spin-density functional theory assumes that the projection of the total spin of the system is a good quantum number. There are cases, like disordered or low-symmetry structures, when this does not happen and non-collinear magnetism can appear [114, 129]. A non-collinear extension to the Kohn-Sham equations has been introduced via the incorporation of the two-component spinor wavefunctions [129–133]. However, the materials under consideration in this thesis do not exhibit non-collinear magnetism and so this will not be further discussed.

2.5.4 Approximations to the exchange-correlation functional

The total energy as a functional of the density can be broken down into a number of different contributions

$$E[\rho] = T_{KS} + V_{ext} + E_H + E_X + E_C, \tag{2.59}$$

where T_{KS} is the kinetic energy of the non-interacting system, E_H is the classical electron-electron Hartree energy, V_{ext} is the external potential due to the nuclei and E_X and E_C are, respectively, the exchange and correlation energies. V_{ext} and E_H are known as explicit functional of the density. T_{KS} and E_X are only known as a functional of the non-interacting Kohn-Sham orbitals while E_C is unknown. From the computational point of view, calculating the exchange energy E_X is quite demanding. If it is treated exactly as a functional of the orbitals, it will not be able to compensate for any error introduced when approximating the correlation energy E_C. The key issue is to deal with the sum of the two terms $E_X + E_C$ taken at the same level of approximation.

LDA

The local density approximation (LDA) [134] is the most popular and widely used approximation for the exchange-correlation energy. The main idea is to consider a general inhomogeneous electron system as locally homogeneous and then to use at any point in space the exchange-correlation functional corresponding to the homogeneous electron gas evaluated at the local density. This latter is known to an excellent accuracy from montecarlo simulations. Thus E_{xc} depends only on the local density of the system

$$E_{xc}^{LDA}[\rho] = \int \epsilon_{xc}^{hom}[\rho(\mathbf{r})]\rho(\mathbf{r})\, d\mathbf{r}, \tag{2.60}$$

where $\epsilon_{xc}^{hom}[\rho(\mathbf{r})]$ is the exchange-correlation energy density for the homogeneous electron gas. The exchange-correlation potential V_{xc} is then obtained from the exchange-correlation functional by the functional derivative

$$V_{xc}^{LDA}(\mathbf{r}) = \frac{\delta E_{xc}^{LDA}[\rho]}{\delta \rho(\mathbf{r})}. \tag{2.61}$$

The LDA approximation is suitable to describe systems with smooth density variations like metals, where the electrons can be treated within the free electron picture, or intrinsic semiconductors. LDA is appropriate for calculating structural and vibrational properties of solids, while binding energies are overestimated and bond lengths underestimated. The limitations of LDA are related to the fact that the inhomogeneities in the density are not taken in account. Moreover, the electron self-interaction present in the Hartree energy term is not completely canceled by the LDA exchange-correlation term [135] (see 2.5.4). The way the correlation term is treated precludes strong local correlation effects to be reproduced.

LSDA

The extension of the LDA to spin-polarized systems is the local spin density approximation (LSDA) which is used to describe magnetic and open-shell materials. The exchange and correlation functional for the two spin components is expressed separately because the exchange contribution is diagonal with respect to spin and it is obtained as an extension of the non-polarized case

$$E_x^{LSDA}[\rho] = \sum_\sigma \int F_x^{LSDA}[\rho^\sigma(\mathbf{r})]\, d\mathbf{r} = \sum_\sigma \frac{1}{2} \int F_x^{LDA}[2\rho^\sigma(\mathbf{r})]\, d\mathbf{r}, \tag{2.62}$$

where F_x^{LDA} is the non-spin-polarized functional. The correlation functional can be obtained by interpolating the homogeneous electron gas case with different spin polarizations and it depends on the charge density of both spins and on the magne-

tization $m(\mathbf{r})$

$$m(\mathbf{r}) = \mu_B[\rho^{\uparrow}(\mathbf{r}) - \rho^{\downarrow}(\mathbf{r})]. \tag{2.63}$$

The magnetic polarization is defined as

$$\xi(\mathbf{r}) = \frac{|m(\mathbf{r})|}{\mu_B \rho(\mathbf{r})}, \tag{2.64}$$

in such a way that $0 \leq \xi \leq 1$. The correlation contribution is given by

$$E_c^{LSDA}[\rho, \xi] = \int \left\{ \epsilon_c^U(\rho(\mathbf{r})) + f(\xi(\mathbf{r}))[\epsilon_c^P(\rho(\mathbf{r})) - \epsilon_c^U(\rho(\mathbf{r}))] \right\} \rho(\mathbf{r})\, d\mathbf{r}, \tag{2.65}$$

where $f(\xi)$ is an interpolation function with $f(0) = 0$ and $f(1) = 1$, and the functionals ϵ_c^P and ϵ_c^U are the correlation energy densities for the polarized and non-polarized system, respectively. The contribution of the exchange and correlation functionals to the Kohn-Sham potential corresponds to an effective magnetic field. By calculating the derivative of the functional with respect to the spin-polarization densities, two terms are obtained: the first is equal for both the polarization states while the second, which depends on the magnetization, has the same absolute value but a different sign according to the spin it is applied to. This last term introduces some differences into the effective fields, producing an imbalance between opposite spin states, and generating the magnetic properties of the system [136].

GGA

The generalized gradient approximation (GGA) [137] can be considered as the natural evolution of the LDA where the exchange-correlation energy is a functional of the local charge density and its own gradient

$$E_{xc}^{GGA}[\rho] = \int \epsilon_{xc}^{GGA}[\rho(\mathbf{r}), |\nabla\rho(\mathbf{r})|]\rho(\mathbf{r})\, d\mathbf{r}. \tag{2.66}$$

The GGA approximation has been developed in many different flavours [137–142] retaining the correct features of the LDA and combining them with the leading contribution originating from the inhomogeneity of the system. The general improvements due to the GGA (with its spin-polarized extension, $\sigma - GGA$) are mainly related to structural properties, binding energies and atomic energies. It also improves bond lengths and angles. Some transition metals, like bulk iron, are correctly described only within the GGA: GGA predicts the correct *bcc* ferromagnetic ground state while it is *fcc* antiferromagnetic within the LDA.

LSDA+U

The LSDA+U scheme [143–145] has been devised to overcome some of the limitations of the LDA/GGA, like the underestimation of the energy band gap and the inadequate description of strongly correlated materials. Transition-metal oxides and rare-earth compounds are characterized by well-localized d and f orbitals which lead to strong correlations effects; placing an electron where another electron is already localized will cost an additional energy U (Hubbard U) [146]. The correlation contribution to the energy is subtracted from the LSDA functional and added again as a Hubbard-like on-site repulsion term

$$E_{LSDA+U}[\rho(\mathbf{r})] = E_{LSDA}[\rho(\mathbf{r})] + E_{Hub}[f^{I\sigma}_{mm'}] - E_{dc}[f^{I\sigma}], \tag{2.67}$$

where $\rho(\mathbf{r})$ is the electronic density, $f^{I\sigma}_{mm'}$ is the occupation number of the atomic orbitals for the I^{th} "Hubbard" atom site I (the one with strongly correlated orbitals), $f^{I\sigma} = \sum_m f^{I\sigma}_{mm}$. Here $E_{LSDA}[\rho(\mathbf{r})]$ is the LSDA energy functional, $E_{Hub}[f^{I\sigma}_{mm'}]$ is the Hubbard corrected on-site correlation term while $E_{dc}[f^{I\sigma}]$ is the LSDA correlation.

The energy functional, according to Anisimov [143–145], can be written as

$$E = E_{LSDA} + \sum_{I} \left[\frac{U}{2} \sum_{m,\sigma \neq m'\sigma'} f_m^{I\sigma} f_{m'}^{I\sigma'} - \frac{U}{2} f^I (f^I - 1) \right], \tag{2.68}$$

where $f_m^{I\sigma} = f_{mm}^{I\sigma}$ and $f^I = \sum_{m,\sigma} f_m^{I\sigma}$. In Eq. (2.68) U is the Hubbard parameter describing the on-site correlation. The last two terms within the square brackets are, respectively, E_{Hub} and E_{dc}. The orbital energy is obtained by taking the derivative of the above equation with respect to the occupation number

$$\epsilon_m^{I\sigma} = \frac{\partial E}{\partial f_m^{I\sigma}} = \epsilon_{0_m}^{I\sigma} + U(\frac{1}{2} - f_m^{I\sigma}). \tag{2.69}$$

The LSDA orbital energy $\epsilon_{0_m}^{I\sigma}$ is shifted by $-U/2$ for the occupied orbitals and by $U/2$ for the empty ones ($f_m^{I\sigma} \sim 0$). The energy difference between occupied and empty orbitals is given by the Hubbard parameter U which provides a correct description of the band gap of Mott-Hubbard insulators. By defining the atomic orbital occupation as the projection of the occupied valence manifold over the corresponding atomic state

$$f_m^{I\sigma} = \sum_{\mathbf{k},n} \langle \psi_{\mathbf{k},n}^{\sigma} | P_m^I | \psi_{\mathbf{k},n}^{\sigma} \rangle, \tag{2.70}$$

the potential to be included within the Kohn-Sham equations reads

$$V_{LSDA+U} = V_{LSDA} + \sum_{I,m} U(\frac{1}{2} - f_m^{I\sigma}) P_m^{I\sigma}, \tag{2.71}$$

where $P_m^{I\sigma}$ are generalized projection operators on the localized electron manifold [136]. If the occupation of an atomic orbital is larger than 1/2 then the Hubbard contribution to the potential is attractive and the electron becomes localized. In contrast if the occupation is smaller than 1/2, the electron tends to be delocalized. In practice the results are not substantially affected by the initial conditions because the

occupation numbers are recalculated during the self-consistent cycles. Fractional occupations $f_m^{I\sigma}$ are often related to energy levels around the Fermi surface for metallic systems. Fractional occupations can also be obtained for localized electronic states, originating from hybridization of d orbitals with neighbouring atoms.

This simple scheme has been proven successful in capturing the main mechanism that could lead to gap opening in strongly correlated materials. On the other side it neglects the exchange coupling and the possible dependence of U on the magnetic quantum number m entering the model. Besides, the expression given in Eq.(2.68) is not invariant under rotation of the atomic orbital basis set used to define the occupancies $f_m^{I\sigma}$. An improved scheme, proposed by Anisimov and coworkers, introduced a basis set independent formulation of $LSDA + U$ [147–149]. A plane-wave pseudopotential formulation of the $LSDA + U$ is given in Ref. [150].

SIC

The self-interaction correction approximation (SIC) [135, 151–154] is aimed at correcting the spurious self-interaction between the charge of an electron and the potential (Hartree and exchange-correlation) that itself generates. While in the Hartree-Fock method the self-interaction of occupied orbitals is exactly cancelled by the exchange energy, this does not happen in the LDA/GGA formalism where the exchange-correlation term is approximated and an exact cancellation does not take place. Errors due to the self-interaction are usually small for materials with delocalized electrons while they can become quite significant for strongly correlated materials where electrons are localized. Several methods to remove the self-interaction have been proposed so far, starting from the work of Perdew and Zunger [135].

The pseudo-SIC [151–154] approximation introduces the occupation numbers for the Kohn and Sham orbitals and it incorporates the self-interaction correction within the pseudopotential formalism. The amount of the correction is rescaled through the

occupation numbers which are calculated self-consistently along with the evolution of the crystal structure relaxation procedure. In this manner localized orbitals, hybridized orbitals and delocalized orbitals can be discriminated and the occupation numbers can provide information about valence band and conduction band states so that only the first ones are corrected. Electrons in the conduction band are usually delocalized and the related self-interaction is negligible or absent. Furthermore they are empty so that no correction should apply. The SIC potential, applied to norm-conserving pseudopotentials, is a non-local projection operator replacing the non-local part of the pseudopotential

$$V^{\sigma}_{HXC}[\rho, m] \rightarrow V^{\sigma}_{HXC}[\rho, m] - \sum_{i} |\Upsilon_i\rangle V^{\sigma}_{HXC}[\rho^{\sigma}_i]\langle\Upsilon_i|, \tag{2.72}$$

where ρ and m are the charge density and the magnetization of the crystal respectively. The SIC term is expressed as a function of atomic quantities, $i = [(l_i, m_i), R_i]$ is a cumulative index incorporating the angular momentum quantum numbers and the atomic coordinates. Υ_i are projection functions (e.g. spherical harmonics), ρ^{σ}_i is the charge density of the (pseudo) atomic orbital ϕ_i

$$\rho^{\sigma}_i(\mathbf{r}) = p^{\sigma}_i |\phi_i(\mathbf{r})|^2, \tag{2.73}$$

p^{σ}_i are the orbital occupation numbers. The Bloch wave functions are projected on the density basis of the atomic orbitals ρ^{σ}_i through the potential $V^{\sigma}_{HXC}[\rho, m]$. For each projection, the Bloch state is corrected by a quantity corresponding to atomic SIC potential $V^{\sigma}_{HXC}[\rho^{\sigma}_i]$. This way enables us to apply the self-interaction correction without introducing any dependence of the Kohn-Sham Hamiltonian on the Bloch wave functions, i.e. the theory remains representation independent. The occupation numbers p^{σ}_i can be fractional because of hybridization, degeneracy or spin-polarization effects and are self-consistently calculated. Unlike LSDA+U, the

SIC method, does not require a choice of which orbitals to correct, nor the value of the J and U parameters. The SIC approach has been used successfully for a large variety of systems. It improves the band gap and band alignment of wide-gap semiconductors, Mott-Hubbard insulators and of transition metal oxides (e.g. cuprates) [155–161]. Furthermore it correctly describes the dissociative behaviour of symmetric radicals such as the H_2^+ molecule where LDA/GGA fail [162].

2.6 Electronic transport at the nanoscale

Nanoscale devices require a theoretical description of electronic transport which goes beyond Ohm's Law and accounts for quantum mechanical effects. Therefore, studying the electron transport when the length scale of a device is comparable with the electron's mean free path is a very challenging problem, and it needs a fully quantum mechanical description in terms of wave function scattering and transmission probabilities. Furthermore it has to account for the fact that the system is no longer in equilibrium. One of the most popular tools to investigate quantum transport is the non-equilibrium Green's function (NEGF) formalism [110, 163–167] combined with DFT. The electronic transport calculations presented in this work are performed within the NEGF framework implemented in the SMEAGOL code[2] [110,111]. SMEAGOL uses the SIESTA code[3] [168] to generate the density matrix. In this thesis we will use the plane-wave VASP code[4] [169–173] for structural relaxation.

2.6.1 Toy model for transport

The key concepts of the *ab initio* electronic transport are described through a toy model, following the guidelines given by Datta [109]. A bottom-up approach is used

[2]website: *www.smeagol.tcd.ie*
[3]website: *www.icmab.es/dmmis/leem/siesta/*
[4]website: *www.vasp.at*

to explain the main principles related to quantum transport, starting from a simple system such as a molecule. The first step is to define the conductance for such a small object by attaching it to two electrodes or leads across which a voltage can be applied. In order to model the current flow it is useful to draw an energy level diagram, where an electrochemical potential is defined for the left (μ_L) and right lead (μ_R). The difference between the two electrochemical potentials can be kept constant by connecting the leads to an external battery. The molecule is meant to have only one energy level, ε, in the region of interest. The maximum conductance G_0 for a one-level device is a fundamental quantity

$$G_0 \equiv \frac{2e^2}{h} = 12.9\, k\Omega^{-1} \tag{2.74}$$

where e is the electron charge and h is the Planck's constant. Let us consider a

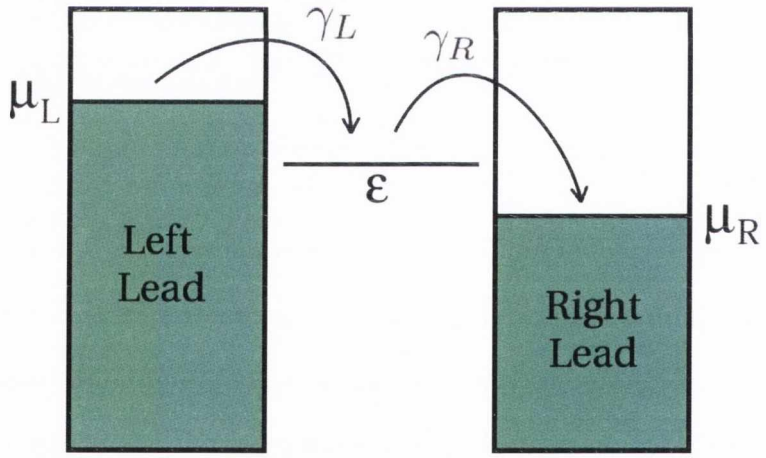

Figure 2.2: Toy model for transport.

system made of a molecule described by a single energy level, ε, and connected to two metallic leads with electrochemical potentials respectively μ_L and μ_R, with $\mu_L > \mu_R$ as in Fig.2.2. The assumption that the leads are metallic implies that they have a continuous distribution of states. When there is no voltage applied between the left (source) and right (drain) lead, it is possible to draw an equilibrium energy level diagram. If the source and drain are coupled to the molecule, electrons will

flow in and out of the molecule bringing them all into equilibrium with a common electrochemical potential μ, in the same way as two material in equilibrium acquire a common temperature T. At equilibrium, the average number of electrons occupying the energy level is given by the Fermi function

$$f_0(E-\mu) = \frac{1}{1+e^{[(E-\mu)/k_BT]}}, \tag{2.75}$$

where $f_0 = 1$ for energies far below μ and $f_0 = 0$ for energies far above μ. If a voltage V_D is applied, it maintains the leads to their relative chemical potentials, separated by qV_D

$$\mu_L - \mu_R = qV_D, \tag{2.76}$$

giving rise to two different Fermi distributions

$$f_L(E-\mu) = \frac{1}{1+e^{[(E-\mu_L)/k_BT]}}, \qquad f_R(E-\mu) = \frac{1}{1+e^{[(E-\mu_R)/k_BT]}}. \tag{2.77}$$

The system cannot reach the equilibrium if $V_D \neq 0$ because the source keeps pumping electrons into the molecule, while the drain is pulling them out of it. The molecule is then forced into a non-equilibrium state resulting in a current flux. The average number of electrons N_e at the steady state will be intermediate between $f_L(\varepsilon)$ and $f_R(\varepsilon)$. The net fluxes I_L from the left lead into the molecule and I_R from the molecule to the right lead are proportional, respectively, to $f_L(\varepsilon) - N_e$ and $N_e - f_R(\varepsilon)$ and are given by

$$I_L = e\frac{\gamma_L}{\hbar}[f_L(\varepsilon) - N_e], \qquad I_R = e\frac{\gamma_R}{\hbar}[f_R(\varepsilon) - N_e], \tag{2.78}$$

where $\gamma_L/\hbar$ and $\gamma_R/\hbar$ can be interpreted as the rates at which an electron, initially placed in the molecular level ε, escapes to the left-hand side or right-hand side lead. At the steady state one has the condition $I_L + I_R = 0$ and the number of electrons

can be written as

$$N_e = \frac{\gamma_L f_L(\varepsilon) + \gamma_R f_R(\varepsilon)}{\gamma_L + \gamma_R}, \tag{2.79}$$

meaning that the occupation N_e of the molecular energy level ε is a weighted average of f_L and f_R. The steady-state current (per spin) is given by

$$I = I_L = -I_R = \frac{e}{\hbar}\frac{\gamma_L \gamma_R}{\gamma_L + \gamma_R}\left[f_L(\varepsilon) - f_R(\varepsilon)\right]. \tag{2.80}$$

A current flowing from the left lead to the right lead requires the presence of states around $E = \mu$ and, of course, that $f_L(\varepsilon) \neq f_R(\varepsilon)$. Energy levels far away from the chemical potentials μ_L and μ_R do not contribute to the conduction process. If they are well below the chemical potentials of both the leads, then $f_L(\varepsilon) \sim f_R(\varepsilon) \sim 1$, while if they are well above $f_L(\varepsilon) \sim f_R(\varepsilon) \sim 0$.

The coupling of the molecular energy level with the leads causes the energy level to broaden because it acquires a finite lifetime. The broadening can be taken into account by introducing a Lorentzian function centered around $E = \varepsilon$, and whose integral over all energy is equal to one (the level has to contain one electron)

$$D_\varepsilon(E) = \frac{\gamma/2\pi}{(E-\varepsilon)^2 + (\gamma/2)^2}. \tag{2.81}$$

The broadening γ is proportional to the strength of the coupling and it is given by $\gamma = \gamma_L + \gamma_R$. From a quantum mechanical point of view, the broadening can be seen as due to the uncertainty principle that requires the product of the lifetime of a state and its spread in energy to be equal to $\hbar$ [174]. The occupation of the broadened level can be written as

$$N = \int_{-\infty}^{+\infty} dE\, D_\varepsilon(E)\frac{\gamma_L f_L + \gamma_R f_R}{\gamma}, \tag{2.82}$$

where we note that this simply generalizes Eq.(2.79). It is worthwhile to notice that

the electron charge density $n(E)$ can be written as

$$n(E) = D_\varepsilon(E)\frac{\gamma_L f_L + \gamma_R f_R}{\gamma}. \tag{2.83}$$

The expression for the current now becomes

$$I = \frac{e}{\hbar}\int_{-\infty}^{+\infty} dE D_\varepsilon(E)\frac{\gamma_L\gamma_R}{\gamma_L+\gamma_R}\left[f_L(E) - f_R(E)\right] = \frac{e}{\hbar}\int_{-\infty}^{+\infty} dE\,\bar{T}(E)\left[f_L(E) - f_R(E)\right], \tag{2.84}$$

where $\bar{T}(E)$ is defined as the transmission coefficient and it is given by

$$\bar{T}(E) \equiv 2\pi D_\varepsilon(E)\frac{\gamma_L\gamma_R}{\gamma_L+\gamma_R} = \frac{\gamma_L\gamma_R}{(E-\varepsilon)^2 + (\gamma/2)^2}. \tag{2.85}$$

At low temperatures we can assume that

$$f_L(E) - f_R(E) = \begin{cases} 1 & \text{if} \quad \mu_L > E > \mu_R \\ 0 & \text{otherwise} \end{cases}, \tag{2.86}$$

so that the expression for the current is simplified and the integration is restricted to the energy window between the chemical potentials of the leads

$$I = \frac{e}{\hbar}\int_{\mu_R}^{\mu_L} dE\,\bar{T}(E). \tag{2.87}$$

If the density of states and hence the transmission is constant over the energy window $[\mu_R, \mu_L]$ (small bias approximation) then the current is given by

$$I = \frac{e}{\hbar}[\mu_L - \mu_R]\frac{\gamma_L\gamma_R}{(\mu-\varepsilon)^2 + (\frac{\gamma_L+\gamma_R}{2})^2}. \tag{2.88}$$

Its maximum value is obtained when the molecular energy level coincides with the average of μ_L and μ_R, $\varepsilon = \mu$.

The previous equations can be recasted in terms of the single particle Green's function G

$$G(E) = \frac{1}{E - \varepsilon + i\gamma/2}. \tag{2.89}$$

The density of states and the electron charge density become

$$\begin{aligned} D_\varepsilon(E) &= \tfrac{1}{2\pi} G(E)\gamma(E)G^\dagger(E) = i[G(E) - G^\dagger(E)], \\ n(E) &= \tfrac{1}{2\pi} G(E)\gamma^{in}(E)G^\dagger(E), \end{aligned} \tag{2.90}$$

where $\gamma^{in} = \gamma_L^{in} + \gamma_R^{in}$ and $\gamma_{L,R}^{in} = \gamma_{L,R} f_{L,R}$. Similarly the current can be written as

$$I = \frac{e}{h} \int_{-\infty}^{+\infty} dE\, G(E)\gamma_L(E)G^\dagger(E)\gamma_R[f_L(E) - f_R(E)]. \tag{2.91}$$

2.6.2 Green's function formalism

The one level model is important to explain the main concepts underlying the flow of current through a conductor, such as the position of the equilibrium electrochemical potential μ relative to the density of states $D(E)$, the broadening of the level γ due to the coupling with the leads and the occupation N of the single energy level ε. In a more general model the electronic structure of the leads has to be taken in account and the molecular single energy level is replaced with a scattering region whose details are described by a Hamiltonian matrix. The typical model of a nanoscale device consists two semi-infinite leads and a scattering region sandwiched between them as shown in Fig. 2.3. The Hamiltonian describing the leads and the scattering region is infinite. The presence of the scattering region breaks the translation symmetry and Bloch's theorem cannot be applied (see section 3.3). The aim of using the non-equilibrium Green's function formalism (NEGF) is that of mapping the infinite system onto a finite one so that it can be solved numerically. As shown in Fig.2.3, the entire device is partitioned into three distinct regions: the left lead, the scattering

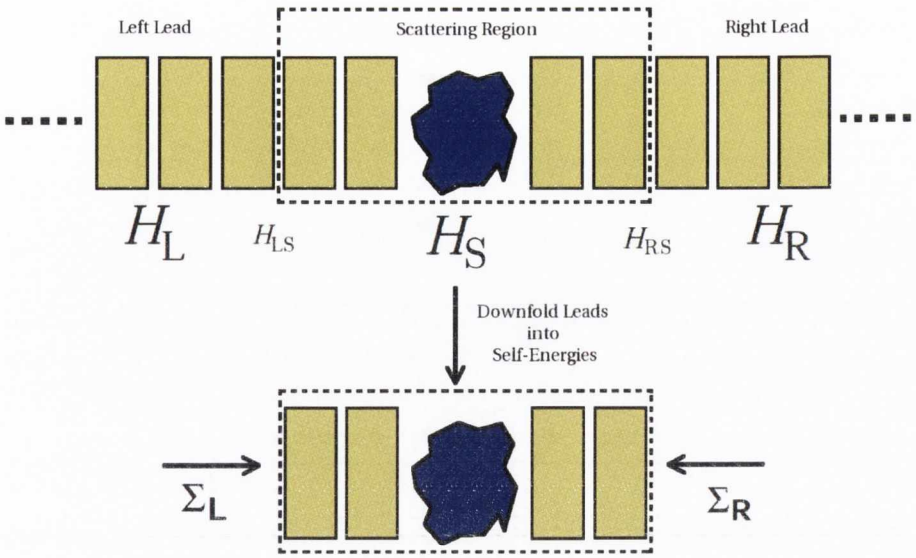

Figure 2.3: A schematic representation of an infinite nanodevice and its mapping onto an effective finite system. The left and right semi-infinite leads are described by the Hamiltonians H_L and H_R while H_S describes the scattering region identified with a dashed square. The Hamiltonian H_L and H_R, as the system contains an infinite number of degrees of freedom, are replaced by the self-energies Σ_L and Σ_R interacting with the finite Hamiltonian H_S of the scattering region.

region and the right lead. A certain number of layers of the leads, called "principle layers", are included in the scattering region in order to allow the charge density to relax to its bulk value. The scattering region described by the Hamiltonian matrix H_S and by the infinite Hamiltonian matrices H_L and H_R accounting for the leads can then be calculated independently. H_{LS} and H_{RS} are matrices describing the interaction between the leads and the scattering region so that the full Hamiltonian,

$\mathcal{H}$, for the infinite system can be written as

$$\mathcal{H} = \begin{pmatrix} . & . & . & . & . & . & . & . & . & . & . \\ . & 0 & H_{-1} & H_0 & H_1 & 0 & . & . & . & . & . \\ . & . & 0 & H_{-1} & H_0 & H_{LS} & 0 & . & . & . & . \\ . & . & . & 0 & H_{SL} & H_S & H_{SR} & 0 & . & . & . \\ . & . & . & . & 0 & H_{RS} & H_0 & H_1 & 0 & . & . \\ . & . & . & . & . & 0 & H_{-1} & H_0 & H_1 & 0 & . \\ . & . & . & . & . & . & . & . & . & . & . \end{pmatrix}, \tag{2.92}$$

where $H_{-1,1}$ is the interaction between principle layers. Reformulating it in a compact way

$$\mathcal{H} = \begin{pmatrix} H_L & H_{LS} & 0 \\ H_{SL} & H_S & H_{SR} \\ 0 & H_{RS} & H_R \end{pmatrix}. \tag{2.93}$$

The overlap matrix $\mathcal{S}$ can be written in the same fashion

$$\mathcal{S} = \begin{pmatrix} S_L & S_{LS} & 0 \\ S_{SL} & S_S & S_{SR} \\ 0 & S_{RS} & S_R \end{pmatrix} \tag{2.94}$$

The NEGF method enables us to generalize the equations written for the toy model to the more complicated electronic structure of real devices and to solve them with a self-consistent method. The electronic structure of the leads far from the interface is not influenced by that of the scattering region and then the semi-infinite Hamiltonian matrices H_L and H_R can be replaced by self-energies [175].

The Green's function $G(E)$ introduced with Eq.(2.89) can be generalized to a more detailed Hamiltonian H_S, that takes in account all the degrees of freedom of

the scattering region

$$G(E) = lim_{\eta \to 0}[(E + i\eta) - H_S - \Sigma_L - \Sigma_R]^{-1}, \tag{2.95}$$

where Σ_L and Σ_R are called self-energies and they are energy dependent matrices describing the electronic structure of the leads and their coupling to the scattering region. $G(E)$ is the Green's function associated to an effective Hamiltonian $H_{eff} = H_S + \Sigma_L + \Sigma_R$, where the self-energies can be considered as external potentials. The self-energies are, in general, complex quantities with the result that the total number of electrons in the scattering region is not conserved. They also possess a non-vanishing real part accounting for a shift of the energy level of the scattering region. The pure complex parts $\Gamma_{L,R}$ of the self-energies are a natural extension of the idea of transmission rate γ and they are usually called broadening matrices

$$\Gamma_L = i[\Sigma_L - \Sigma_L{}^\dagger], \qquad \Gamma_R = i[\Sigma_R - \Sigma_R{}^\dagger]. \tag{2.96}$$

The two terminal current can then be defined as

$$I = \frac{e}{h} \int_{-\infty}^{+\infty} dE\, Tr[G(E)\Gamma_L(E)G^\dagger(E)\Gamma_R(E)][f_L(E) - f_R(E)]. \tag{2.97}$$

This is an expression similar to the one derived for the toy model, where the total transmission coefficient is now defined as $T(E) = Tr[G\Gamma_L G^\dagger \Gamma_R]$ [176].

The current can be calculated once the Hamiltonian for the scattering region and the self-energies are known. The exact form of the scattering region Hamiltonian H_S is usually not known. However, because of its functional dependence on the electronic structure, it can be calculated self-consistently. By assuming that H_S depends on the single particle density matrix ρ associated to the scattering region, then $H_S(\rho)$ can be constructed by means of a single particle electronic structure method, such as

DFT. The density matrix ρ can be obtained from the Green's function $G(E)$ of the scattering region by integrating over energy. The energy dependent density matrix $n(E)$ is given by

$$n(E) = \frac{1}{2\pi} G(E)\Gamma^{in}(E)G^{\dagger}(E) = \frac{1}{2\pi} G(E)[\Gamma_L(E)f_L(E)+\Gamma_R(E)f_R(E)]G^{\dagger}(E), \quad (2.98)$$

and the density matrix is obtained by integration [177]

$$\rho = \frac{1}{2\pi} \int dE\, G(E)[\Gamma_L(E)f_L(E) + \Gamma_R(E)f_R(E)]G^{\dagger}(E). \quad (2.99)$$

The self-energies can be evaluated by considering the scattering region attached to only one lead. The Hamiltonian H for the system comprising the scattering region and the left-hand side lead is a semi-infinite matrix of the form

$$\begin{pmatrix} H_L & H_{LS} \\ H_{LS}^{\dagger} & H_S \end{pmatrix}. \quad (2.100)$$

The corresponding retarded Green's function $G = [E + i\eta - H]^{-1}$ can be partitioned in blocks and it can be obtained by formal inversion of the Hamiltonian:

$$G = \begin{pmatrix} G_L & G_{LS} \\ G_{SL} & G_S \end{pmatrix} = \begin{pmatrix} (E + i\eta)I + H_L & H_{LS} \\ H_{LS}^{\dagger} & EI + H_S \end{pmatrix}^{-1}. \quad (2.101)$$

The expression for G_S, the Green's function for the scattering region attached to the left lead, can be extracted from the previous equation

$$[(E + i\eta)I - H_L]G_{LS} + H_{LS}G_S = 0 \quad (2.102)$$

and

$$[EI - H_S]G_S + H_{LS}^{\dagger}G_{LS} = 0 \quad (2.103)$$

G_{LS} is then given by

$$G_{LS} = -g_L H_{LS} G_S, \tag{2.104}$$

where

$$g_L = [(E + i\eta)I - H_L]^{-1} \tag{2.105}$$

is the retarded Green's function for the semi-infinite left lead. The expression for the Green's function of the scattering region can then be written as

$$G_S = [EI - H_S - H_{LS}^{\dagger} g_L H_{LS}]^{-1}. \tag{2.106}$$

By comparing this equation with the equation (2.95) enables us to identify $H_{LS}^{\dagger} g_L H_{LS}$ as the self-energy Σ_L of the left lead. H_{LS} is in principle a $N \times N$ matrix where N is the number of the degrees of freedom in the scattering region, but in practice it accounts for the coupling of a limited number of atoms (surface atoms). The Green's function g_L can be identified with the surface Green's function of the left electrode because only surface atoms of the leads are relevant to calculate the product $H_{LS}^{\dagger} g_L H_{LS}$ [177].

Finite Bias

The expression for the current given in equation (2.97) involves the integration of the transmission coefficient $T(E) = Tr[G\Gamma_L G^{\dagger}\Gamma_R]$ over the bias window. A self-consistent evaluation of the potential drop can be obtained by considering the fact that the information about the charge density in the scattering region is now available. The bias can be introduced and the transmission coefficient $T(E)$ can be replaced by the bias-dependent counterpart $T(E, V)$. The potential drop is expected to affect only the scattering region (which includes few layers of the leads) because the leads are metallic and, due to the strong electron screening, the electrical potential relaxes rapidly to its bulk value away from the surface. The application of a

finite bias over the leads causes a shifting of their chemical potentials resulting in a relative displacement of the entire bands structure of the leads. When the bias V is applied, the Hamiltonian of the left lead is shifted rigidly by $+V/2$ and the one of the right lead by $-V/2$, so that

$$H_L \to H_L + \frac{V}{2} I; \qquad H_R \to H_R - \frac{V}{2} I. \tag{2.107}$$

In terms of self-energies this translates into the following expression

$$\Sigma_L(E) \to \Sigma_L(E - \frac{V}{2}); \qquad \Sigma_R(E) \to \Sigma_R(E + \frac{V}{2}). \tag{2.108}$$

The rigid shift of the leads potential sets the boundary conditions, while a convenient choice of the scattering region ensures that those boundary conditions can be matched by an appropriate electrostatic calculation. These two ingredients are enough to determine the potential drop by solving the Poisson equation for the scattering region. A conventional way to tackle the problem is to add a linear potential drop to the Hamiltonian of the scattering region

$$H_S(V) = H_S + \beta V I \tag{2.109}$$

and solve the equation with an iterative self-consistent procedure.

2.7 The SMEAGOL code

SMEAGOL (Spin and Molecular Electronics on Atomically Generated Orbital Landscape) [110, 111] is a fully spin-polarized code which combines the NEGF method with the DFT code SIESTA [168]. Since SIESTA is based on a non-orthogonal localized atomic orbital basis set [178] in conjunction with scalar relativistic Troullier-Martins pesudopotentials [179, 180] with non linear core corrections [181], it can

handle systems with a large number of degrees of freedom and it can be interfaced with SMEAGOL. SMEAGOL is an ideal tool for studying magneto-transport problem, including non-collinear spin magnetism and it has been used very successfully to describe transport properties of heterostructures [182], tunnel junctions [183,184], molecules [185, 186], DNA [157], point contacts [187], nanowires [188] and nanotubes [189] amongst others. SMEAGOL uses the Kohn-Sham Hamiltonian obtained by SIESTA and the leads self-energies determined by a pre-calculated bulk system. Then it constructs the effective NEGF Hamiltonian and generates the retarded Green's function for the scattering region.

2.8 Summary

This chapter has reviewed the basic theoretical framework necessary for finding an approximate solution to the quantum many-body problem of N interacting particles. The adiabatic approximation enabled us to separate the motion of nuclei, that can be treated in a classical way, from the motion of electrons, treated quantistically. The two-body nature of the electron-electron interaction has been approximated with a single particle picture by making use of the mean-field approximation. Finally, the density functional theory was applied to map the system of interacting fermions into a system of non-interacting particles that can be solved selfconsistently through the use of a computer.

A theoretical description of the main ideas behind the electronic quantum transport has been given.

The application of this framework in the context of periodic systems is the subject of the next chapter.

CHAPTER 3

Periodic Systems

3.1 Introduction

This chapter presents the general aspects involved in the practical, numerical problem of solving self-consistently the Kohn-Sham equations for an electronic system. The pseudopotential scheme which aims to simplify the description of the electron-nucleus interaction will be introduced in section 3.2. In section 3.3 the Bloch's theorem is presented. It provides a very powerful tool for describing periodic systems. It allows to map the calculation of the wave functions for all the electrons in an infinite solid onto the calculation of the wave functions within the unit cell, called first Brillouin zone. The plane waves and atom centered basis sets are also described. The Brillouin zone needs to be sampled over a finite number of k-points. Schemes have been developed to reduce the number of the k-points and find a convenient balance between computational demand and calculation accuracy. This is the subject of section 3.5. When dealing with surfaces or systems containing defects, the periodic

supercell approach is very useful. It is described in section 3.6.

Most of the calculations performed in this thesis have been done with the plane-wave code VASP. The main algorithms implemented in VASP are presented in section 3.7 together with the PAW pseudopotentials implemented in it.

***

The Kohn-Sham formulation of the density functional theory is an approximate scheme aimed to simplify the $3n$-dimensional many-body problem into a tractable one. Within the DFT scheme the following eigenvalue problem need to be solved

$$\left[-\frac{\hbar^2}{2m}\nabla^2 + V_{ext}(\mathbf{r}) + \int \frac{\rho(\mathbf{r}')}{|\mathbf{r}-\mathbf{r}'|} + \mu_{XC}(\rho)\right]\phi_i(\mathbf{r}) = \varepsilon_i\phi_i(\mathbf{r}), \tag{3.1}$$

where the one-electron density is given by

$$\rho(\mathbf{r}) = \sum_{i=1}^{n} f_i|\phi_i(\mathbf{r})|^2. \tag{3.2}$$

Here n is the number of electrons and f_i are the occupation numbers corresponding to the one-electron eigenstates. The external potential V_{ext} accounts for the interaction between electrons and nuclei and is given by

$$V_{ext}(\mathbf{r}) = -e^2\sum_{I=1}^{N}\frac{Z_I}{|\mathbf{r}-\mathbf{R_I}|}, \tag{3.3}$$

and one of the approximations discussed in section 2.5.4 are taken for the exchange-correlation potential.

3.2 Pseudopotential

The electron-nucleus interaction can be further simplified by considering different "classes" of electrons to be treated in a different way. Valence electrons actively participate in the chemical bond and require an accurate description, while core

electrons are tighly bound to the nuclei, do not participate in bonding and can be treated as frozen orbitals. There is, in principle, a third class of electrons, called semi-core electrons, which do not participate actively in bonding but feel the presence of the environment because their energy is close to the one of the valence electrons. Their wave functions polarize and they cannot be treated as frozen orbitals. The pseudopotential is an effective potential constructed to replace the atomic all-electron potential such that core states are eliminated and the valence electrons are described by nodeless pseudo-wavefunctions. Only the chemically active valence electrons are dealt with explicitly, while the core electrons are "frozen", i.e. they are considered together with the nuclei as rigid non-polarizable ion cores. The pseudopotential approximation [190–197] is based on the consideration that the quantities of interest for studying physical systems are mainly related to valence properties, where the effects of the core electrons are negligible. The potential due to the nucleus can then be replaced with an effective nuclear potential of charge $Z_V = Z - Z_{core}$ where Z_{core} is the charge associated to the core electrons. Core states are localized in the proximity of the nucleus where valence states oscillate in order to maintain orthogonality with the core functions. The valence electrons experience a large kinetic energy in the core region, which roughly cancels the large potential energy from the Coulomb interaction. Hellmann in 1935 replaced these effects by a pseudopotential, which is repulsive in the core region and therefore keeps the electrons out of the core (Pauli repulsion) [190, 198, 199]. The "real" wave functions are replaced by pseudo-wave functions (Fig.3.1) which are constructed in such a way to be nodeless in the core region, where the real wave functions have nodes induced by the orthogonality with core states, and to coincide with the all-electron wave functions in the valence region. The separation between these two regions is defined by a proper cutoff radius r_c (Fig.3.1). An important requirement for pseudopotentials is to be norm-conserving: by construction the pseudopotential has to preserve the norm of the

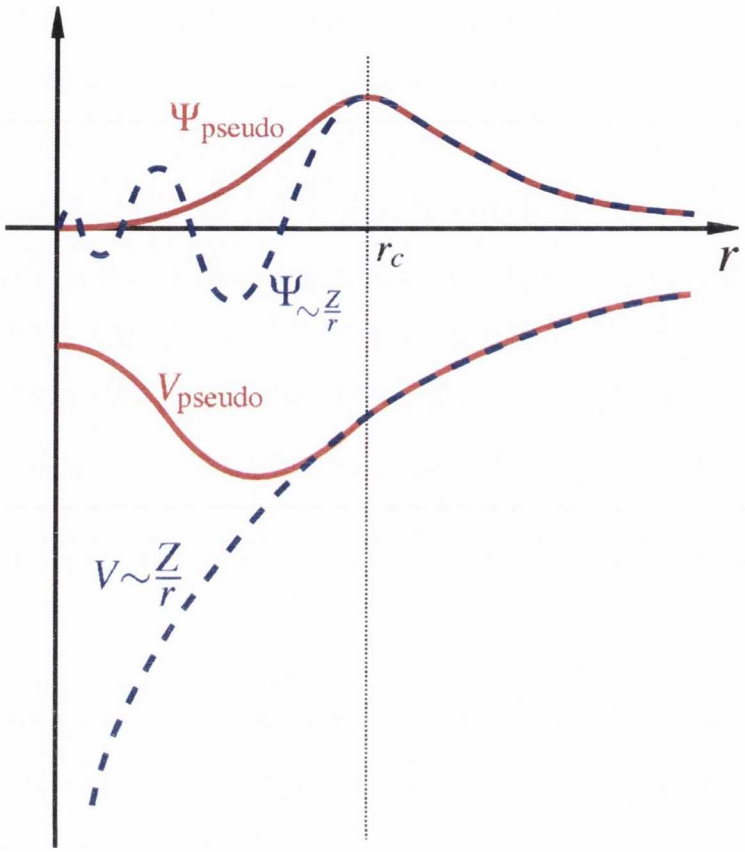

Figure 3.1: Schematic representation of the pseudopotential approximation. The wave function in the Coulomb potential of the nucleus (blue) is compared with the one in the pseudopotential (red). The real and the pseudo wave function and potentials match above a certain cutoff radius r_c.

wave function. This means that the pseudo-wave function conserves the electronic charge within the core region and let the pseudo-atom maintain the original scattering properties [200–202]. In order to correctly reproduce the wave function scattering properties of the all-electron system, the pseudopotential can be split into a local part $V^L(\mathbf{r})$, describing the potential far away from the core, and a non-local part $V^{NL}(\mathbf{r}, \mathbf{r}')$, inside the core region, which depends on the angular momentum

$$V^{PP}(\mathbf{r})\psi(\mathbf{r}) = V^L(\mathbf{r})\psi(\mathbf{r}) + \int d\mathbf{r}'\, V^{NL}(\mathbf{r}, \mathbf{r}')\psi(\mathbf{r}'). \tag{3.4}$$

The transferability is another requirements to keep into consideration when constructing pseudopotentials. This is the ability of the pseudopotential to repro-

duce the physical charateristics of the real systems in different chemical environments [181, 203]. A complete treatment of the pseudopotential formalism can be found here [190, 194].

3.3 Bloch's theorem

The investigation of the properties of crystalline solids by means of *ab initio* methods is based on the assumption that atoms belonging to a lattice are fixed in their equilibrium positions arranged in a periodic structure. This structure can be described by a small number of atoms (called the basis), periodically replicated along one, two or three directions in space. Despite the fact that the choice of the basis atoms is arbitrary, i.e. there are infinite ways of characterizing a crystalline solid, there is a minimal choice, corresponding to what is called the Wigner-Seitz cell. The repetition of this cell along the crystallographic directions reproduces the entire symmetry of the crystal. This cell, also called the unit cell, together with the lattice vectors and the directions of replication, contains all the information needed to reproduce the periodic crystalline structure. The vectors used to generate the periodic lattice from the unit cell are called primitive vectors. The set of points in space corresponding to integer combinations of the primitive vectors leads to 32 possible lattices in three dimensions, called Bravais lattices. The combination of the translational symmetry embodied in the Bravais lattice with the point group symmetry of the basis gives rise to 230 space groups, which classify all known crystalline solids with translational symmetry. If we call the primitive vectors a_1, a_2, a_3, then the volume of the unit cell is given by $\Omega = a_1 \cdot (a_2 \times a_3)$ and the Wigner-Seitz cell is the one enclosing the smallest possible volume. The external potential $V(\mathbf{r})$, due to the interaction between the ionic lattice and the electrons belonging to the crystal, has the same periodicity of the lattice

$$V(\mathbf{r} + \mathbf{R}) = V(\mathbf{r}), \tag{3.5}$$

where $\mathbf{R}$ is a vector of the lattice and can be expressed as a linear combination of primitive vectors. The electronic Hamiltonian, likewise the physical properties of the periodic system, share the same translation invariance of the lattice.

Bloch theorem [204] is a powerful tool for the study of periodic structures and connects the properties of the electrons in a periodic infinite system to those of the electrons in the unit cell. It states that

the wave function of an electron in a periodic potential can be written as the product of a function with the same periodicity of the potential, and a purely imaginary phase factor arising from the translational symmetry.

The solutions of the Schrödinger equation for the crystalline lattice are called Bloch functions and represent the single particle eigenstates for electrons in a periodic potential $V(\mathbf{r})$

$$\psi_{n,\mathbf{k}}(\mathbf{r}) = e^{i\mathbf{k}\cdot\mathbf{r}} u_{n,\mathbf{k}}(\mathbf{r}), \tag{3.6}$$

where $\mathbf{k}$ is the crystal momentum of the electron, n is the band index for states corresponding to the same $\mathbf{k}$ and $u_{n,\mathbf{k}}(\mathbf{r})$ is a periodic function on the lattice so that

$$u_{n,\mathbf{k}}(\mathbf{r}+\mathbf{R}) = u_{n,\mathbf{k}}(\mathbf{r}). \tag{3.7}$$

From Bloch's theorem it also follows that

$$\psi_{n,\mathbf{k}}(\mathbf{r}+\mathbf{R}) = e^{i\mathbf{k}\cdot\mathbf{R}} \psi_{n,\mathbf{k}}(\mathbf{r}). \tag{3.8}$$

This means that the Bloch wave functions gain a phase factor equal to $e^{i\mathbf{k}\cdot\mathbf{R}}$ when it is translated in real space by a vector $\mathbf{R}$. There is a particular class of vectors $\mathbf{k}$ such that $e^{i\mathbf{k}\cdot\mathbf{R}} = 1$, meaning that the wave function is in phase in all the periodic replicas of the unit cell. The set of three smallest independent vectors belonging to this class define the reciprocal lattice vectors, similarly to the primitive vectors in

the real space. The primitive vectors in the reciprocal space, $\mathbf{b_i}$, are defined by the relation $\mathbf{a_i} \cdot \mathbf{b_j} = 2\pi\delta_{ij}$. They are given by

$$\mathbf{b}_1 = 2\pi\frac{\mathbf{a}_2 \times \mathbf{a}_3}{\Omega}, \qquad \mathbf{b}_2 = 2\pi\frac{\mathbf{a}_3 \times \mathbf{a}_1}{\Omega}, \qquad \mathbf{b}_3 = 2\pi\frac{\mathbf{a}_1 \times \mathbf{a}_2}{\Omega}. \tag{3.9}$$

The primitive reciprocal lattice vectors define a cell in the reciprocal space of volume $\Omega_R = \mathbf{b_1}\cdot(\mathbf{b_2}\times\mathbf{b_3}) = (2\pi)^3/\Omega$ which is called the first Brillouin zone. Larger Brillouin zone (second, third...) can be constructed by considering the second or third shell of reciprocal lattice vectors. It is customary to fold all the wave vectors back to the first Brillouin zone by subtracting a reciprocal lattice vector. This scheme is called the reduced zone diagram. The expressions of the periodic potential and the periodic function for the reciprocal lattice is obtained by a Fourier expansion (plane-wave expansion)

$$V(\mathbf{r}) = \sum_{\mathbf{G}} V(\mathbf{G})\, e^{-i\mathbf{G}\cdot\mathbf{r}}, \tag{3.10}$$

$$u_{\mathbf{k}}(\mathbf{r}) = \sum_{\mathbf{G}} e^{i\mathbf{G}\cdot\mathbf{r}}\, C(\mathbf{k}+\mathbf{G}), \tag{3.11}$$

where $\mathbf{G}$ is the vector that defines the periodicity of the reciprocal lattice and is related to $\mathbf{R}$ by

$$\mathbf{R}\cdot\mathbf{G} = 2\pi m \qquad \text{with} \qquad m \in \mathcal{N}. \tag{3.12}$$

The single-electron orbital within the crystal can be then written as

$$\psi_{n,\mathbf{k}}(\mathbf{r}) = \sum_{\mathbf{G}} e^{i(\mathbf{k}+\mathbf{G})\cdot\mathbf{r}}\, C_{n,\mathbf{k}}(\mathbf{G}). \tag{3.13}$$

The calculation of the wave functions for all the electrons in an infinite solid is mapped, through Bloch's theorem, onto the calculation of the wave functions within the unit cell at an infinite number of $\mathbf{k}$ points within the first Brillouin zone. From the practical point of view a finite number of $\mathbf{k}$ vectors in the first Brillouin zone

has to be considered, and the number is reduced in order to find a balance between numerical accuracy and computational effort.

3.4 Basis set

Solving the electronic structure problem within DFT requires the choice of a mathematical representation for the one-electron orbitals. This representation is called basis set. A possibility is to represent the orbitals on a three-dimensional grid in real space, and to solve the partial differential equations using finite differences methods. However, more efficient alternatives are possible by making use of the specific characteristics of the system. Amongst the most popular basis set are the plane waves and the atom centered linear combination of atomic orbitals (LCAO). We limit our description to these two cases because they are the ones implemented in the simulation codes we utilized for the calculations. In particular VASP uses a plane waves basis set while a LCAO basis set is adopted by SIESTA and SMEAGOL.

3.4.1 Plane waves

Bloch's theorem prescribes that the wave functions must be composed of a phase factor and a periodic part that verifies $u_k(\mathbf{r}) = u_k(\mathbf{r} + \mathbf{a_i})$, with a_i any lattice vector. This property can be used to introduce naturally the basis set of plane waves (PW) which are solutions of the Schrödinger equation in the presence of a constant external potential. In general, any function in real space can be written as the Fourier transform of a function in reciprocal space

$$u_k(\mathbf{r}) = \int e^{i\mathbf{g}\cdot\mathbf{r}} u_k(\mathbf{g}) d\mathbf{g}, \tag{3.14}$$

but due to the periodicity of $u_k(\mathbf{r})$, the only allowed values of $\mathbf{g}$ are those that verify $e^{i\mathbf{g}\cdot\mathbf{a_j}} = 1$. This implies that the $\mathbf{g}$ vectors are restricted precisely to the reciprocal

lattice vectors **G** defined by Eq. 3.12. The general expression of the wave function for the different eigenstates j becomes

$$\psi_j^{(\mathbf{k})}(\mathbf{r}) = \frac{1}{\sqrt{\Omega}} \sum_{G=0}^{\infty} C_{j\mathbf{k}}(\mathbf{G}) e^{i(\mathbf{k}+\mathbf{G})\cdot\mathbf{r}}, \tag{3.15}$$

where the plane waves are suitably normalized in the supercell so that PWs corresponding to different wave vectors, $\mathbf{G} \neq \mathbf{G}'$, are orthogonal.

In principle, an infinite number of **G** vectors is required to represent the wave functions with infinite accuracy. In practice, however, the Fourier coefficients $C_{\mathbf{k}}(\mathbf{G})$ of the wave functions decrease with increasing $|\mathbf{k}+\mathbf{G}|$, so that the PW expansion can be effectively truncated at a finite number of terms. The expansion can be limited to all waves with kinetic energy lower than some energy cutoff E_{cut} so that

$$\frac{\hbar^2}{2m}|\mathbf{k}+\mathbf{G}|^2 < E_{cut}. \tag{3.16}$$

The value of E_{cut} has to be chosen case by case as the best compromise between numerical accuracy and computational cost.

3.4.2 LCAO

In the quantum chemistry and molecular physics communities the most common approach is to expand the one-electron wave functions in terms of atomic orbitals. Atomic orbitals are centered on the atomic nuclei, and can be represented in terms of basis functions with different functional forms. A suitable basis should be designed in order to provide a reasonable accuracy when a small number of basis functions are used and to allow a systematic improvement of its quality when the number of basis functions is incremented. Analytic functions such as Slater type orbitals or numerical atomic basis functions can be employed for the purpose. Tipically, the

eigenstates are expanded over a finite number of atom centered basis functions

$$\psi_j(\mathbf{r}) = \sum_{\alpha} C_{\alpha}^{j} \phi_{\alpha}^{I}(\mathbf{r}), \tag{3.17}$$

where $\phi_{\alpha}^{I}(\mathbf{r})$ is a generic basis function centered on atom I and α labels the type of basis functions. α usually corresponds to a set of indices $\alpha = (n, l, m)$ that indicate angular momentum (l,m) and radial orbital n. Since the molecular electronic distribution is largely dominated by atomic distributions, a natural choice is to optimize the basis functions to reproduce the atomic orbitals, and then export them to molecular systems or condensed phases. This scheme is called linear combination of atomic orbitals (LCAO). These atomic orbitals are the product of a radial function and a spherical armonic. For an atom I located at $\mathbf{R}_I$

$$\phi_{lmn}^{I}(\mathbf{r}) = \phi_{ln}^{I}(r_I) Y_{lm}(\mathbf{r}_I), \tag{3.18}$$

where $\mathbf{r}_I = \mathbf{r} - \mathbf{R}_I$ and $r_I = |\mathbf{r}_I|$.

The angular momentum (labelled by l,m) may be arbitrarily large and, in general, there will be several orbitals (labelled by index n) with the same angular dependence, but different radial dependence, forming what is conventionally called a multiple-ζ basis. The first-ζ orbital $\phi_l^{1\zeta}(r)$ is constructed as an eigenfunction of the pseudo-atom within a hard wall spherical potential of radius r_c. Higher ζ-functions are constructed in the spirit of the "split valence" scheme. For instance the second-ζ function $\phi_l^{2\zeta}(r)$ has the same tail as the $\phi_l^{1\zeta}(r)$ but it changes to a simple polynomial behaviour inside a "split radius" r_l^s

$$\phi_l^{2\zeta}(r) = \begin{cases} r^l(a_l - b_l r^2) & \text{if} \quad r < r_l^s \\ \phi_l^{1\zeta}(r) & \text{if} \quad r > r_l^s, \end{cases} \tag{3.19}$$

where a_l and b_l are determined by imposing the continuity of value and slope at

r_l^s. Polarization orbitals can also be included. They are constructed from a perturbed atomic Hamiltonian in order to account for the deformation induced by bond formation.

3.5 Brillouin zone sampling

For an infinite crystal the set of **k** points needed to describe the entire electronic structure forms a continuum; for a real lattice the number of **k** points depends on the boundary conditions and it is proportional to the number of atoms in the lattice ($\sim N_A$). For each **k** point the number of occupied electronic states is finite so that, by using the Bloch's theorem, the practical problem of evaluating the charge density is reduced to calculate a reasonably small number of Bloch wave function for a large number of **k** points. Some physical quantities, such as the density of states (DOS), are calculated by integration over the **k** points in the Brillouin zone (and over the band index n). From a computational point of view, it would not be feasible to calculate these quantities over all the **k** points and several methods have been developed to reduce this number by taking in account the symmetry of the system [205–207]. Moreover, the wave function is not expected to change considerably between close **k** points. The **k** points sampling scheme is a very efficient one for the description of semiconductors and insulators. Metals have to be treated carefully due to the dispersion of bands around the Fermi surface and they require an accurate **k** point sampling. In order to overcome this problem, a very dense **k**-point mesh can be used and a fictitious electronic temperature can be introduced in order to smear the weight of the states around the Fermi surface thus avoiding fluctuations [208]. From a practical point of view, the **k**-point mesh is taken by studying the convergence of quantities of interest such as the total energy, for successively denser meshes till the required accuracy is achieved. One of the most common scheme for **k**-mesh generation is the Monkhorst-Pack scheme [206]. The sampling point are defined in

the following manner

$$\mathbf{k}(n,m,l) = n\mathbf{b_1} + m\mathbf{b_2} + l\mathbf{b_3}, \qquad n,m,l = \frac{2r-q-1}{2q}; \qquad r = 1,2,3,...,q \quad (3.20)$$

where $\mathbf{b_i}$ are the reciprocal lattice vectors of the supercell and n, m and l are the mesh sizes for each reciprocal lattice vector direction. Therefore the total number of sampled $\mathbf{k}$-points is $n \times m \times l$. If, under the symmetries of the supercell, some of the points are found to be equivalent, then only the nonequivalent $\mathbf{k}$-points are considered to save computational time.

3.6 Periodic supercell

The periodicity of the system may break due to the presence of defects or if the system is a molecule or a cluster. Then Bloch's theorem cannot be applied. In the supercell approach, an artificial periodicity is imposed on the simulation cell to better model the continuum properties of the system and the Bloch theorem may then be applied to the wave functions. This enable us to reproduce the correct physical and chemical properties of such a class of systems. In the case of a point defect the supercell consists of a portion of bulk material big enough to avoid interaction between the defect and its periodic images. The supercell approach applied to surfaces consists of adding a large enough vacuum region to simulate the potential drop into the vacuum and to avoid interaction between adjacent periodic images. In the case of molecules, the supercell approach is mostly related to the use of plane-waves formalism. The plane waves fill the entire space occupied by the molecule and a surrounding vacuum region has to be accounted for in order to avoid interaction between neighbouring periodic images. In principle, a molecule can be described with a localized basis set where the periodic boundary conditions have been switched off, without making use of the supercell approach. The case of charged systems is generally treated by

including a uniformly spread compensating background charge with opposite sign.

3.7 VASP code

All the DFT calculations presented in this thesis were performed by using the Vienna Ab-Initio Simulation Package[1] (VASP) [169–173]. VASP is a complex package for *ab initio* quantum-mechanical simulations using the pseudopotential formalism and a plane wave basis set. The interaction between ions and electrons is described by ultra-soft Vanderbilt pseudopotentials (US-PP) [209, 210] or by the projector-augmented wave (PAW) method [211]. The combination of this scheme with efficient numerical methods leads to an efficient, robust and fast algorithm for evaluating the self-consistent solution of the Kohn-Sham problem. The implemented iterative matrix diagonalisation schemes (RMM-DISS, and blocked Davidson) are probably among the fastest schemes currently available for solving an eigenvalue problem and they are both implemented in VASP [212–214]. VASP includes a full featured symmetry algorithm, which automatically determines the symmetry of the system under study. The symmetry code is also used to set up a special grid of **k**-points, according to the Monkhorst Pack [206] scheme, which allows an efficient calculation of bulk materials and symmetric clusters. The integration of the band-structure energy over the Brillouin zone is performed with the smearing or the tetrahedron methods [215, 216]. For the tetrahedron method, Blöchl's corrections, which remove the quadratic error of the linear tetrahedron method, can be used resulting in a fast convergence with respect to the number of special **k**-points [217]. In any plane wave program, the execution time scales as N^3 for some parts of the code, where N is the number of valence electrons in the system.

[1] website: *www.vasp.at*

3.7.1 PAW pseudopotentials

The PAW scheme [211] combines the versatility of the linear augmented plane wave (LAPW) methods [218] with the formal simplicity of the plane-wave pseudopotential approach. The typical strategy of any augmented plane waves methods is to split the wave function into two parts: a partial-wave expansion within a sphere centered on the atom and an envelope function, expanded in plane waves, outside the sphere. The envelope function and the partial-wave expansions are matched with value and derivative at the sphere radius. The physically relevant wave functions in the Hilbert space of all the wave functions orthogonal to the core states, exhibit strong oscillations and are numerically difficult to treat. The main idea behind the PAW approach is to transform the wave functions of this Hilbert space into a pseudo Hilbert space. A linear transformation maps the physical valence wave functions onto the fictitious ones in the pseudo space, drastically reducing the computational effort. The pseudo-space wave functions will be identified with the envelope functions of the linear method or the wave functions of the pseudopotential approach. The physical quantities of interest can be obtained, knowing the transformation $\mathcal{T}$, as the expectation value of some operator A from the pseudo-space wave functions $|\tilde{\psi}\rangle$ directly after the transformation to the true all-electron wave functions $|\psi\rangle$

$$\langle A \rangle = \langle \psi | A | \psi \rangle \qquad \text{with} \qquad |\psi\rangle = \mathcal{T}|\tilde{\psi}\rangle, \tag{3.21}$$

or as the expectation value of a pseudo-space operator $\tilde{A}$ in the Hilbert space of the pseudo-space wave functions

$$\langle A \rangle = \langle \psi | \tilde{A} | \psi \rangle , \qquad \text{with} \qquad \tilde{A} = \mathcal{T}^{\dagger} A \, \mathcal{T}. \tag{3.22}$$

The total energy can be evaluated as a functional of the pseudo-space wave functions where the ground state of the pseudo-space wave functions can be obtained from

$$\frac{\partial E[\mathcal{T}|\tilde{\psi}\rangle]}{\partial\langle\tilde{\psi}|} = \varepsilon\,\mathcal{T}^{\dagger}\mathcal{T}|\tilde{\psi}\rangle. \tag{3.23}$$

The transformation $\mathcal{T}$ can be chosen in a way that it differs from the identity by a sum of local, atom-centered contributions, $\hat{\mathcal{T}}_R$, such that

$$\mathcal{T} = 1 + \sum_R \hat{\mathcal{T}}_R, \tag{3.24}$$

where each local contribution $\hat{\mathcal{T}}_R$ acts only over some augmentation region Ω_R enclosing the atom. The all-electron and pseudo-space wave functions coincide outside the augmentation regions. The local terms $\hat{\mathcal{T}}_R$ are defined for each augmentation region by specifying the target functions $|\phi_i\rangle = (1 + \hat{\mathcal{T}}_R)|\tilde{\phi}_i\rangle$ orthogonal to the core states within Ω_R. The initial states $|\tilde{\phi}_i\rangle$ are called pseudo-space partial waves, corresponding to the all-electron partial waves $|\phi_i\rangle$. The partial waves $|\phi_i\rangle$ can be the solutions of the Schrödinger equation for the isolated atom which are orthogonalized to the core states. The index i refers to the atomic sites R, the angular momentum quantum numbers $L = (l, m)$, and an index n to label different partial waves with the same angular momentum. The functions $|\phi_i\rangle$ and $|\tilde{\phi}_i\rangle$ have to be identical outside the augmentation region and have to form a complete set within it. Every pseudo-space wave function can be expanded into pseudo-space partial waves within Ω_R

$$|\tilde{\psi}\rangle = \sum_i c_i|\tilde{\phi}_i\rangle. \tag{3.25}$$

Since $|\phi_i\rangle = \mathcal{T}|\tilde{\phi}_i\rangle$ then

$$|\psi\rangle = \mathcal{T}|\tilde{\psi}_i\rangle = \sum_i c_i|\phi_i\rangle, \tag{3.26}$$

with identical coefficients c_i. The all-electron wave function can be then written as

$$|\psi\rangle = |\tilde{\psi}\rangle - \sum_i c_i|\tilde{\phi}_i\rangle + \sum_i c_i|\phi_i\rangle, \tag{3.27}$$

where c_i have to be determined. Since the transformation $\mathcal{T}$ is linear, the coefficients c_i must be linear functionals of the pseudo-space wave functions

$$c_i = \langle\tilde{p}_i|\tilde{\psi}\rangle, \tag{3.28}$$

where $\langle\tilde{p}_i|$ are one for each pseudo-space partial wave and they are called projector functions. Each projector must fulfill the condition

$$\sum_i |\tilde{\phi}_i\rangle\langle\tilde{p}_i| = 1 \qquad \text{within} \quad \Omega_R \quad \Rightarrow \quad \sum_i |\tilde{\phi}_i\rangle\langle\tilde{p}_i|\psi\rangle \equiv |\psi\rangle \quad \Rightarrow \quad \langle\tilde{p}_i|\tilde{\phi}_j\rangle = \delta_{ij}. \tag{3.29}$$

The linear transformation between the valence wave functions and the fictitious pseudo-space wave functions is finally given by

$$\mathcal{T} = 1 + \sum_i (|\phi_i\rangle - |\tilde{\phi}_i\rangle)\langle\tilde{p}_i|. \tag{3.30}$$

The all-electron wave functions can be obtained from the pseudo-space wave function by

$$|\psi\rangle = |\tilde{\psi}\rangle + \sum_i (|\phi_i\rangle - |\tilde{\phi}_i\rangle)\langle\tilde{p}_i|\tilde{\psi}\rangle. \tag{3.31}$$

This transformation requires the knowledge of three quantities: (i) the all-electrons partial waves $|\phi_i\rangle$, obtained from the Schrödinger equation; (ii) one pseudo-space partial wave $|\tilde{\phi}_i\rangle$ for each $|\phi_i\rangle$, where the two must coincide outside some augmentation region; (iii) one $|\tilde{p}_i\rangle$ for each $|\tilde{\phi}_i\rangle$ within the augmentation region, satisfying $\langle\tilde{p}_i|\tilde{\phi}_j\rangle = \delta_{ij}$. The partial waves are functions defined on a radial grid, multiplied with spherical harmonics, while the pseudo-space wave functions are expanded into

plane waves. The projectors are calculated as radial functions times spherical harmonics and then expanded in plane waves. The number of plane waves used in the expansion is set by the so called cut-off energy. A cut-off energy of 400 eV is enough, in most cases, to guarantee the convergence of the energy functional.

3.8 Summary

This chapter has reviewed some practical schemes aimed to simplify the numerical self-consistent solution of the Kohn-Sham equations for an electronic system. The concept of pseudopotential has been introduced to reduce the computational demand when calculating the electron-nucleus interaction. The Bloch's theorem provides a powerful tool for describing periodic systems. The supercell approach enabled us to treat systems with a reduced periodicity, e.g. due to the presence of defects. A brief overview of the VASP code has also been given. These tools are normaly included in the most popular *ab-initio* simulation codes and have been used to perform the calculations presented in the subsequent chapters.

CHAPTER 4

Single Hydrogen atom on Si(100) surface: local approach

4.1 Introduction

The bonding configuration and the charge state of a single Hydrogen atom deposited on a bare Si(100)-$c(4 \times 2)$ surface are investigated by means of density functional theory simulations and compared to cryogenic scanning tunneling microscopy/spectroscopy (STM/STS) experiments. In this chapter I will describe the local approach meaning that I will consider only the informations that can be obtained when the STM tip is at a spatial position corresponding to the reacted dimer and its surroundings. In the following chapter the non-local approach will be described, where the ex-situ informations are used to characterize the bonding and charging state of the adsorbed Hydrogen.

Two adsorption configurations for the H atom on the Si surface are considered. These are shown in fig. 4.1. The H-bottom configuration (H_B) consists of the H atom sitting on the bottom atom of the Si surface dimer, while in the H-top one

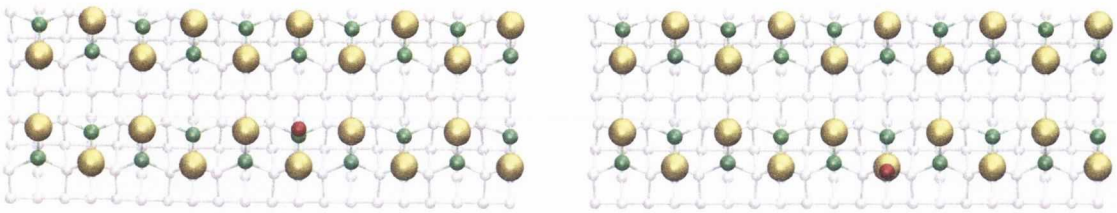

(a) H BOTTOM (b) H TOP

Figure 4.1: Schematic top view representation (XY plane) of the H_B (a) and H_T (b) supercell configurations. The supercell is 10 dimers long along the X direction. Yellow and green atoms are, respectively the top and the bottom atom of the surface Si dimers while the red color is used for the H atom.

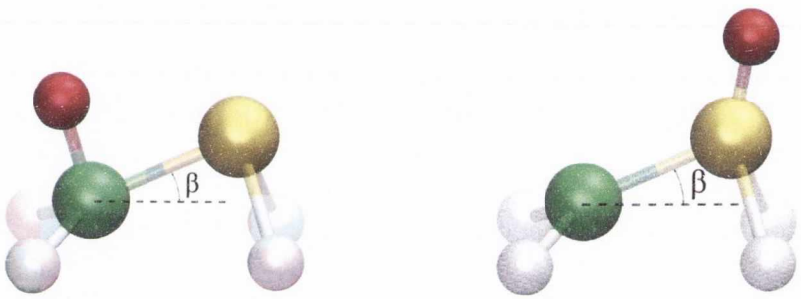

(a) H_B configuration (b) H_T configuration

Figure 4.2: Perspective view of a balls-and-sticks model of the reacted surface Si dimer in the H_B (a) and H_T (b) configurations. The yellow and green atoms are, respectively, the Si top and bottom atom of the surface dimer. The red atom is the deposited H.

(H_T) the H atom is sitting on the top atom of the dimer. These two configurations are studied for the undoped case (Section 4.2) and for heavily *p*- and *n*-doped systems (Section 4.3). First principles calculations are performed with the density functional theory VASP package [169–173], using projected augmented wave (PAW) pseudopotentials [211] together with the generalized gradient approximation (GGA-PBE) to the exchange and correlation functional [137, 139]. The electronic properties of the $c(4\times2)$ reconstructed surface are calculated with a supercell apporach and periodic boundary conditions. The supercell contains 441 atoms arranged over 9 Si layers, one H passivating layer at the bottom of the cell and a 12 Å vacuum region at the top in order to avoid interaction between periodic images. The supercell is 15.132 Å wide in the direction perpendicular to the dimer rows and it extends 37.83 Å along the

direction of the dimer rows. This corresponds to five repeated primitive unit cells of the $c(4\times2)$ reconstructed surface (each of which has a length of 7.566 Å and contains 88 atoms) along the dimer rows resulting in two rows of 10 alternating dimers forming the topmost surface layer (see Fig. 4.1). The buckling angle β is defined as the angle formed between the dimer bond direction and the plane parallel to the surface [orthogonal to the (100) direction]. For the bare surface β=19.7 degrees (see table 4.1). The geometry optimization of the supercell was performed with a force tolerance of 0.02 eV/Å. The number of Si layers in the supercell was chosen by considering the displacement of the atoms from their original bulk positions after a full geometry optimization. We performed some test by using two supercells containing 9 and 11 Si layers, respectively. In both cases the displacement of the atoms belonging to the bottom Si layer with respect to the bulk was negligible and the band structure and DOS of the two systems almost indistinguishable. This justifies the choice of using the 9 layers supercell which reduces the computational effort. All the calculations were carried out by keeping fixed the positions of the bottom Si layer and the H passivating layer. The cutoff radius for the plane-waves expansion of the basis set is fixed to 500 eV. This value was determined by testing the convergence of the total energy with respect to the cutoff radius to be lower than 10 meV. A further increase in the cutoff radius does not improve significantly the precision of the calculations. The same method was used to estimate the optimal k-mesh. A $3\times3\times1$ k-point mesh was used to span the Brillouin zone. It provides the required accuracy in the total energy and it enables us to calculate the DOS with the tetrahedron method [217], one of the most accurate schemes available.

Doping is introduced by adding (or subtracting) one unit charge to the supercell and by compensating the extra charge with a neutralizing uniform positive (or negative) background. This is a standard procedure in charged periodic systems studied with the supercell approach. The total energy of a charged supercell replicated by

periodic boundary contitions will diverge if no neutralizing background is applied. Another problem that needs to be addressed is the Coulomb interaction between the defect and its periodic replicas. In general, for bulk systems, this spurious Coulomb interaction can be corrected by adding a term given by $(e^2q^2\alpha)/(L\epsilon)$, where q is the net charge of the system, α is the Madelung constant of a point charge q placed in a homogenous background charge $-q$ and ϵ is the dielectric constant of the system. In the case of periodic charged slabs, however, the total energy cannot be corrected since a charged slab results in a growing electrostatic potential with the distance from the slab. As a result of the interaction between the charged slab and the compensating background, the total energy depends linearly on the width of the vacuum region. In order to be sure that the amount of vacuum does not affect the results, we performed total energy calculations for the two H configurations with a different amount of vacuum in the direction perpendicular to the surface. The calculations, executed with an amount of vacuum ranging from 10 Å to 15 Å, show very small variations in the total energy differcence (within 10%), confirming the reliability of the results.

The topographic images were obtained by simulating a constant-current (variable height) scanning mode within the Tersoff-Hamann approximation [70, 76] following a similar procedure to the one described in Ref. [104]. In practice the local DOS (from which the current is obtained), calculated by integration over an energy range around the Fermi level E_{F}, is evaluated at a variable distance from the surface in order to take in account the surface corrugation due to the adsorbed species. The average distance between the tip and the surface can be determined by choosing a convenient DOS isosurface. The isosurface can be selected by setting an isovalue that, in our case, corresponds to a distance of about 4 Å between the tip and the surface, a reasonable value considering the general DFT trend of overestimating the wavefunction decay in vacuum. The procedure we follow to calculate the STM topographies and STS maps,

i.e. the constant current mode, enables us to compare directly our results with the experiments. The DOS values are mapped on a greyscale (where the black and white colors correspond to no DOS and high DOS, respectively) and the final simulated topographic image is then elaborated with an image manipulation software to apply a gaussian blur filter.

The simulated color DOS plots (LDOS) are obtained by assigning a coloured pixel to each atom position and for each energy value. The colour scale is set by the maximum (dark red) and minimum (blue) value of the DOS. The pixel is represented by a gaussian along the energy axis with a broadening of 0.01 eV. The broadening along the X axis is automatically applied by the image visualization software and it is a common interpolating procedure. These parameters do not affect the features of the plots from a qualitative point of view.

I will refer to the first row of the surface as the one containing the reacted dimer while the second row is the bare one. In all the figures of this chapter I will use a color code for the balls-and-sticks supercell models where the yellow and green balls represent, respectively, the top and the bottom atoms of the surface Si dimers. The red color is used for the H atom on the surface. When a H atom is placed over the dimer, it passivates one of the dangling bonds of the surface Si dimer, breaking the Si-Si dimer π-bond and leaving an isolated dangling bond on the other side of the dimer. I will refer to the isolated dangling bond as the single dangling bond (SDB) [51]. The SDB is depicted in the balls-and-sticks models as a blue protrusion [e.g. in Fig. 4.3(a)] where the small black balls are the electrons occupying it. The adsorption of the H atom can be performed by using the tip of a STM microscope: the STM probe can be operated to pick up the H atom from some region of the sample and then release it at the desired specific position with atomic precision. The details of the electronic states originating from the SDB depend on the configuration of the H, namely H_B and H_T, the doping of the sample and the surface strain due to

a change in the bond configuration of neighbouring dimers.

Radny *et al.* studied the chemisorption of a single H atom on the *n*-type Si(100) surface by means of first principles DFT calculations and STM microscopy [219]. They used the term "hemihydride" to refer to the reacted dimer containing the adsorbed H. Their results were obtained in different experimental conditions and calculations setup with respect to our settings. The measurements shown in Ref. [219] were taken at room temperature and refer to *n*-doped samples with a resistivity of 1 Ωcm. Our measurements were taken at 77 K and the *n*-doped samples we used have a resistivity which is three order of magnitude smaller. Radny *et al.* solely made use of STM topographic images, corroborated by first-principles DFT calculations while we utilized also STS spectroscopic images to address the position of the dangling bond state with respect to the Fermi level and its charging state. The computational setting they employed for the DFT simulations included a 4×4 supercell which is much smaller than the 10×4 supercell we used. By taking in account the periodic boundary conditions, it implies a much higher H coverage of the surface, resembling an array of H atoms more than an isolated H. They performed additional calculations on 2×4, 2×6 and 6×6 supercells but these supercell are not all commensurate to reproduce the c(4×2) reconstruction we focused on. In the work of Radny *et al.*, 4 to 6 layers of Si atoms, in the direction perpendicular to the surface, were used to simulate the slab. We used 9 layers to better take in account the relaxation of the surface. They investigated two H configurations. The HH2 that corresponds to the one we called H_T [see Fig. 4.1(b)], and the HH1, corresponding to the one we called H_{3DIM} [see Fig. 4.15(b)] that was never observed experimentally. Surprisingly, the configuration we named H_B [see Fig. 4.1(a)] was not taken in consideration in their study.

Reusch *et al.* presented a STM study of the occupation of a single dangling bond on a Si(100) surface under *n*- and *p*-doping conditions [220]. While the resistivity

of the *p*-doped samples was very similar to the one of our samples ($\sim 10^{-3}$ Ωcm), the resistivity of their *n*-doped samples was three order of magnitude bigger. STM topographic images (some are the same as in Ref. [219]!), were compared with DFT cluster calculations. No STS spectroscopic images were used. The cluster used for the simulation is equivalent to a 5×2 supercell where H atoms passivate all the dangling bonds, except for the surface ones. For size and symmetry reason this supercell cannot reproduce the c(4×2) reconstruction of the Si(100) surface. A comparison between our results and the ones obtained from Radny *et al.* and Reusch *et al.* will be pointed out throughout the text.

4.2 Undoped system

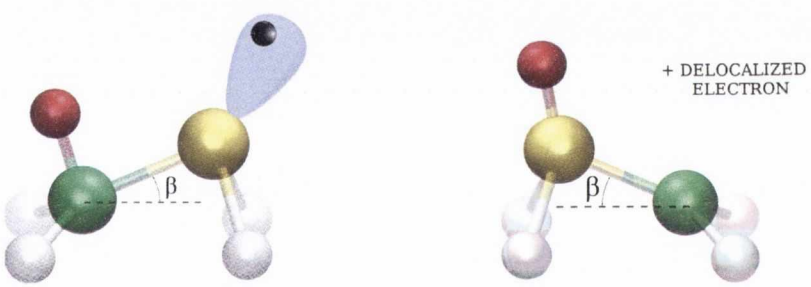

(a) H_B configuration (b) H_T configuration

Figure 4.3: Schematic representation of the reacted dimer for the undoped H_B and H_T configurations. The electron coming from the SDB site is localized at the reacted dimer site in the case of the H_B configuration (a), while it is delocalized on the surface for the H_T one (b).

Total energy calculations show the H_B configuration to be lower in energy by 26 meV with respect to the H_T one (see table 4.1). Reusch *et al.* found a comparable total energy for a similar configuration [220] and a similar trend was also found for Ge(001) [221]. The band structure plots show two different scenarios: the H_B configuration has a spin-polarized ground state with a localized spin split state at the SDB site. The spin up state is partially filled with one electron and it lies around 0.4 eV under the Fermi level E_F as shown in Fig. 4.4(a) (black filled circles). The

spin down state is empty and it lies around 0.1 eV above the Fermi level (blue filled circles in Fig. 4.4(a)). The spin polarized bands coming from the SDB are almost dispersionless and this gives a clear indication that such a state is mostly localized at the SDB site and contains only one electron.

In contrast, the ground state of the H_T configuration is not spin polarized and the band structure shows a band crossing the Fermi level (black filled circles in Fig. 4.4(b)). This band is dispersed along the $\Gamma - J$ (and $K - J'$) direction, which is the direction along the dimer rows, meaning that the electron originating from the SDB state is delocalized over the neighbouring dimers while the dispersion is negligible along the direction perpendicular to the dimers row. This result is in agreement with the band structure calculated by Radny *et al.* for the HH2 configuration (see Ref. [219]).

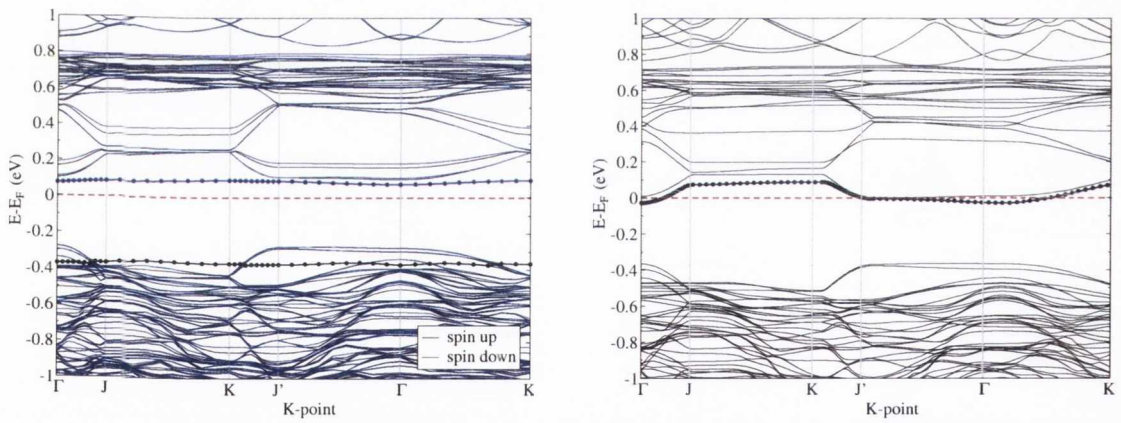

(a) H_B configuration (b) H_T configuration

Figure 4.4: Band structure of the H_B (a) and H_T (b) configurations. (a): the filled circles bands are the majority (black) and minority (blue) spin polarized states related to the single dangling bond, which is partially occupied by one electron. (b): the filled circles band is due to the electron coming from the dangling bond state which is delocalized on the surface.

The simulated local density of states (LDOS) of the first row of the H_B configuration, for the majority and minority spin states, are shown in Fig. 4.5. The DOS is plotted as a function of position and energy (in eV), where the position has to be considered along the dimers row direction. The plots use a color scale with blue

meaning low DOS and red corresponding to the maximum DOS. The underlying balls-and-sticks model indicates the position of the H atom and, consequently, of the SDB. Due to the periodic boundary conditions used here, the system is equivalent to a ~40 Å long quantum well with the reacted dimers acting as potential barriers. The local DOS shows a partially filled spin up level lying 0.4 eV below E_F and an empty spin down level at around 0.1 eV above E_F. Both these levels are mostly localized at the site facing the H atom, as it can be seen from the DOS projected on the atomic sites (PDOS)(see Fig. 4.6). No evident band bending is present at the SDB site, suggesting that this keeps its neutral charging (one electron). The peak in the LDOS located at around 0.15 eV and present for both the spin channels, is the first quantum well standing wave state which originates from our periodic boundary conditions. In the minority spin channel this is partially hybridized with the state localized at the SDB site. The buckling angle β of the reacted dimer is around 0 degrees suggesting a bonding configuration of mixed symmetry, intermediate between sp^2 and sp^3, in agreement with the partial occupation of the SDB site [222].

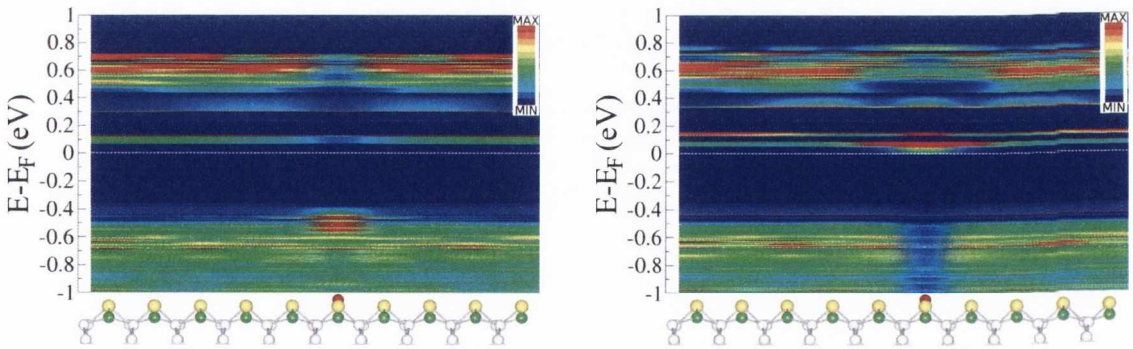

(a) Majority spin LDOS

(b) Minority spin LDOS

Figure 4.5: Local density of states (LDOS) for the majority (a) and minority (b) spin states of the H_B configuration (first row). According to the color scale, the blue color corresponds to zero DOS and the red color to a value of the DOS higher than 2 states/eV per supercell. a) The red spot located at around 0.4 eV under the Fermi level at a spatial position corresponding to the H site is associated to the SDB spin up state, which is singly occupied. b) The minority (spin down) state is empty and it lies around 0.1 eV above E_F.

The local DOS for the H_T configuration is shown in Fig. 4.7(a). The state as-

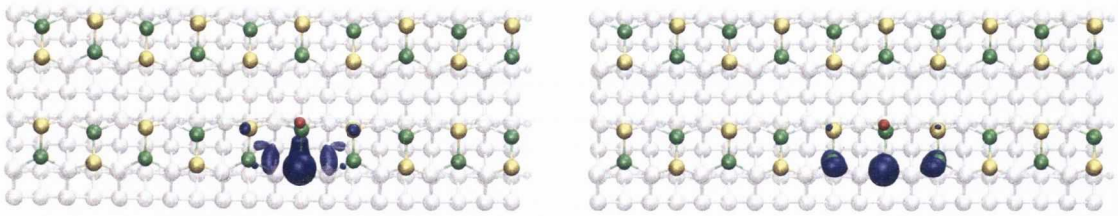

(a) Majority spin PDOS (b) Minority spin PDOS

Figure 4.6: Projected density of states (PDOS) for the majority (a) and minority (b) spin states of the SDB in the H_B configuration. Both states are mainly localized at the SDB site and they correspond to the filled circle bands shown in Fig. 4.4(a). (a): Partially filled spin up state; (b): empty spin down state.

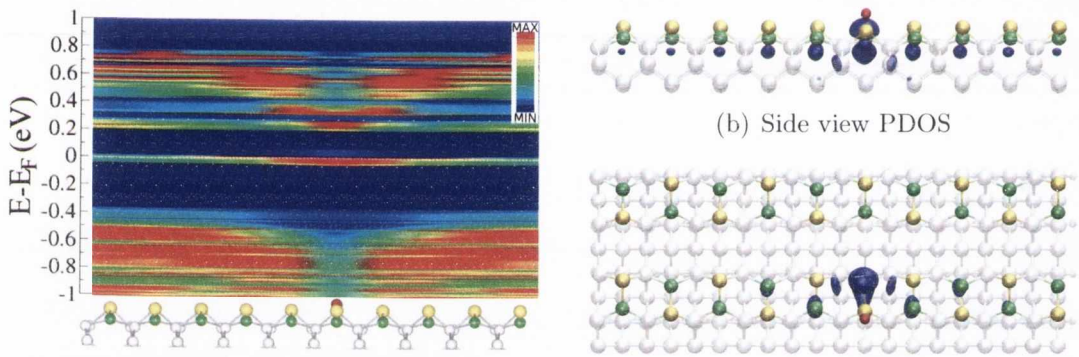

(a) H_T configuration (b) Side view PDOS (c) Top view PDOS

Figure 4.7: (a): LDOS of the first row of the H_T configuration. The extended feature across the Fermi level indicates that the electron coming from the SDB state is delocalized on the surface resulting in a positive charging at the SDB site and a consequent downward band bending in the valence band. According to the color scale, the blue color corresponds to zero DOS and the red color to a value of the DOS higher than 2 states/eV per supercell. The side view (b) and top view (c) of the PDOS shows the SDB state to be mostly delocalized over the dimers row so that the SDB state can be considered as empty.

sociated to the SDB is now located across the Fermi energy and it appears more delocalized than the H_B case, as can also be seen from the PDOS [Figs. 4.7(b) and 4.7(c)]. A downward band bending is noticeable around the SDB site, suggesting that the dangling bond site may be positively charged. This confirms the idea that the electron coming from the SDB site is delocalized on the surface resulting in a locally positive charging of the SDB site (less than one electron). The buckling angle β of the reacted dimer is around 10 degrees (see table 4.1) suggesting that the bonding configuration of the Si atom hosting the dangling bond is sp^2-like and the

Config	Energy (meV)	H Dimer (deg)	Mag.Mom.
bare surface	-	19.7	0
H_B	0	-0.106	0.95
H_T	+26	10.167	0
H_B +1e	0	7.896	0
H_T +1e	+136	2.279	0.79
H_B -1e	0	-10.612	0
H_T -1e	-111	11.198	0

Table 4.1: Total energy differences, buckling angles and magnetic moments for different configurations. The total energies are always taken with respect to the energy of the H_B configuration.

dangling bond is empty [222]. These results are in good agreement with the "HH2" antiparallel configuration described by Radny *et al.*, who found a buckling angle of 9.6 degrees [219].

4.3 Effect of doping

The doped systems are obtained by adding or subtracting an extra electron to the supercell used in the calculations. The supercell has the same size of the one described in the introduction. It consists of 441 atoms where the topmost Si layer forms 10 dimers along the dimer row direction. This translates to a nominal doping of the order of 10^{20} cm^{-3}. A full relaxation was performed after adding the extra charge while the position of the bottom Si layer and the passivating H layer were kept fixed.

The results will be compared to experimental STM/STS data, performed using a Createc cryogenic system described elsewhere [66]. Both *n*-type (As, 0.001-0.005 Ωcm) and *p*-type (B, 0.001-0.005 Ωcm) Si(100) samples used are mounted on a triple sample holder containing also a Pt surface for tip preparation and recovery. In-situ Pt-inked tungsten probe [223] is used in the STM. Sub-monolayer atomic hydrogen coverage is deposited on the clean surface at 200 K via a heated tungsten capillary. The H atoms are manipulated by transferring them on and from the STM probe

applying high biases (5-6V) with different polarities. The spectroscopic results are obtained through variable-height scanning tunneling spectroscopy (VH-STS) [66] at 77 K.

4.3.1 *n*-doping

(a) *n*-doped H_B (b) *n*-doped H_T

Figure 4.8: Schematic representation of the reacted dimer for the *n*-doped H_B and H_T configurations. The SDB site is localized at the reacted dimer site and doubly occupied in the case of the H_B configuration (a). The H_T one (b) shows a complex scenario: one electron is delocalized on the surface as in the neutral case while the electron coming from the doping is localized at the SDB site.

The experimental STM topographs of both filled-state and empty-state for the H_B and H_T configurations are now compared with the simulated one. The experimental images are recorded at a constant current of 20 pA and sample bias of +0.5 V and -1.0 V for the empty and filled states, respectively. The corresponding simulated topographies are calculated with sample biases of +0.5 V and -0.5 V. By observing the experimental topographs, the reacted site can be identified as a bright spot assosciated with the SDB in the filled-states images and its exact position within the dimer can be determined by comparing it with the unreacted region of the surface. In an unreacted region of the surface, bottom atoms of the dimers appear as bright spots in the empty-states images, while top atoms appear as bright spots in the filled-states images [224, 225]. This let us map the location of lower and upper atoms of the tilted Si dimers.

The filled-state panel in Fig. 4.9(a) depicts the upper unreacted dimer atoms

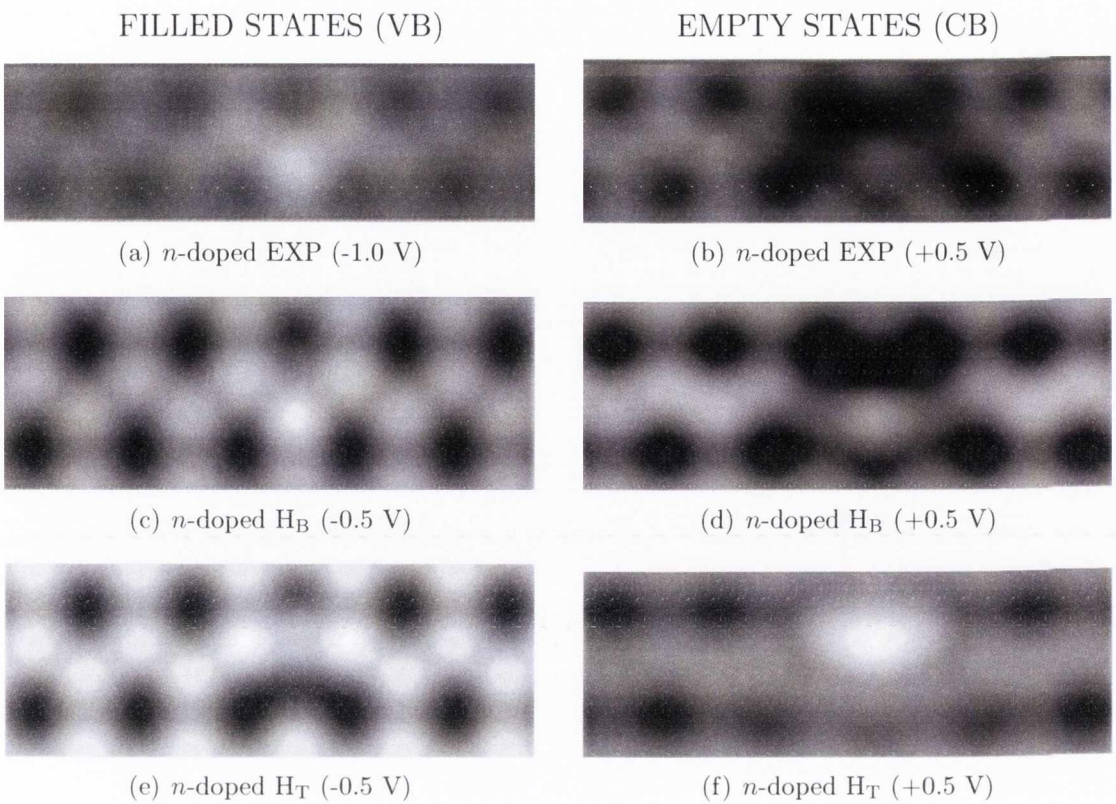

(a) n-doped EXP (-1.0 V) (b) n-doped EXP (+0.5 V)

(c) n-doped H_B (-0.5 V) (d) n-doped H_B (+0.5 V)

(e) n-doped H_T (-0.5 V) (f) n-doped H_T (+0.5 V)

Figure 4.9: Top panels (a) and (b) are the experimental topographic images for filled and empty states acquired for a sample bias of -1.0 V and +0.5 V respectively. Panels (c) and (d) are the corresponding simulated topographs for the n-doped H_B configuration. Panels (e) and (f) are the simulated topographs for the n-doped H_T configuration. The simulated data are referred to the reacted row (1^{st} row) of the 10×4 supercell and are obtained by considering a bias of -0.5 V and 0.5 V for filled and empy states, respectively. Bright areas correspond to a high DOS, while dark areas to low or null DOS. Only the H_B images match the experimental data.

and shows that the maximum associated with the SDB at the reacted dimer site is in phase with the dimer tilting either side of the reacted dimer. The image differs from that of the bare surface only by the increased brightness of the reacted dimer. The empty-states panel in Fig. 4.9(b) depicts the bottom atom of the unreacted dimers and the reacted site appears as an M-shaped dark feature in which the SDB maximum is out of phase with the tilting pattern of the lower dimer atoms. A comparison between Fig. 4.9(a) and 4.9(b) reveals the same pattern of dimer tilting so that a change in the tunneling polarity does not induce this pattern to flip. From

the previous consideration, it can be deduced that the SDB sits on the top atom of the dimer while the H atom is on the bottom atom of the dimer. This configuration was experimentally found to be the most abundant on the surface by at least one order of magnitude, and it is named as the majority species.

The experimental images are compared with the simulated ones for the H_B and H_T configurations, shown in Fig. 4.9. Only H_B matches experiments as it can be noticed by comparing Fig. 4.9(c) with Fig. 4.9(a) for the filled-states and Fig. 4.9(d) with 4.9(b) for the empty ones. This let us establish that the majority species identified in the experiments is the H_B configuration [226]. The ground state of the H_B

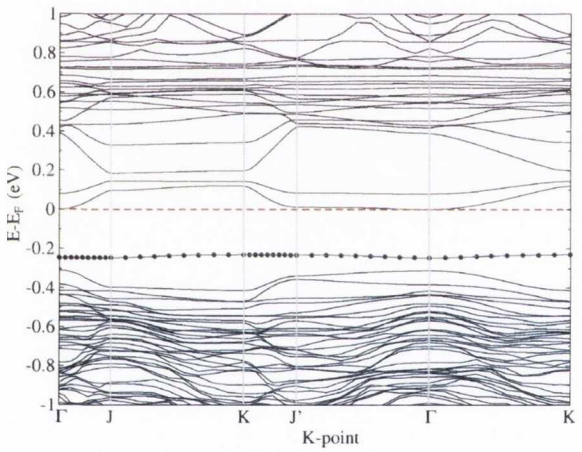

(a) n-doped H_B configuration

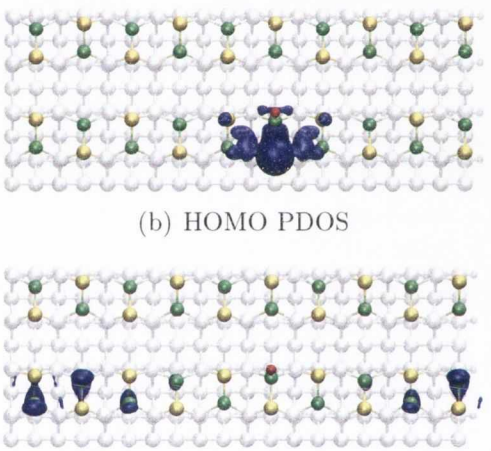

(b) HOMO PDOS

(c) LUMO PDOS

Figure 4.10: Calculated band structure (a) for the n-doped H_B configuration. The flat band at around 0.25 eV below E_F (filled dots) is localized at the SDB site and it is doubly occupied, as confirmed by the PDOS in (b). Panel (c) shows the first nodeless quantum well state, due to the periodic boundary conditions. The maximum amplitude of the PDOS is located at the farthest site (within the unit cell) from the reacted dimer which acts as confining barrier.

configuration is not spin polarized and the calculated band structure [Fig. 4.10(a)], shows a single flat band at around 0.25 eV below E_F. The PDOS relative to the same band indicates that such a state is mainly localized at the SDB site, suggesting it is doubly occupied [Fig. 4.10(b)]. The simulated LDOS [see Fig. 4.11(a)] is in a good agreement with the experimental one [Fig. 4.11(b)]. The experimental peak coming from the SDB is located at around 0.3 eV below E_F. Both the images show

a upward band banding due to the extra charge present at the SDB site, which is negligible for the undoped case [compare Fig. 4.11(a) with Fig. 4.5]. Note that the calculated band curvature is more marked then expected due to periodic boundary conditions. Another effect of the boundary conditions is the fact that the simulated cell is equivalent to a quantum well, with the reacted dimers acting as potential barriers. The state at around 0.1 eV above E_F in Fig. 4.11(a) is the first quantum well state and the corresponding PDOS has the shape of a nodeless standing wave [Fig. 4.10(c)]. This explains why such a state is not present in the experimental LDOS of Fig. 4.11(b).

The effect of the electrostatic repulsion due to the extra charge located at the SDB site and the change in the hybridization configuration of the dimer are reflected in the structural properties of the system. The dimer bond length increases from 2.397 Å to 2.453 Å and the buckling angle β goes from almost 0 to around 8 degrees (see Tab. 4.1 for structural data). When going from single to double occupation the Si atom hosting the dangling bond changes his bonding configuration from a mixed sp^2-sp^3 hybridization to a prevalent sp^3 character [222].

Experimental topographs for the minority species (appearing with a frequency smaller then 1%) are shown in Fig. 4.12. The filled-states data for the minority species [Fig. 4.12(a)] looks identical to that of the majority species of Fig. 4.9(c). However, the empty-states image [Fig. 4.12(b)] shows that the SDB is in phase with the pattern of adjacent tilted dimers. The bright spot at the reacted dimer in the empty-states is sitting on the bottom atom of the dimer, meaning that H is on the top atom of the dimer. A comparison of the unreacted dimers on either side of the minority site reveals a change in the pattern of dimer tilting, so that a change in the tunneling bias polarity causes the entire dimer row to flip. As a consequence, the experimental data for the minority species match the simulated H_B configuration for the filled-states and the H_T one for the empty-states [226]. The same dimer-row

(a) n-doped H_B configuration

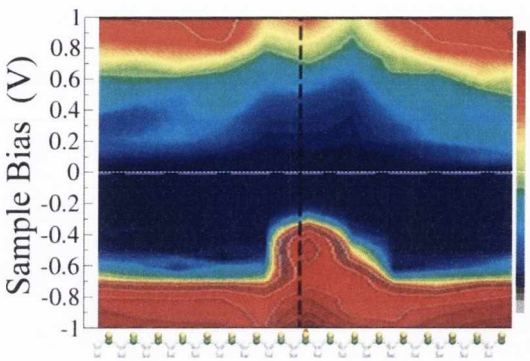

(b) EXP n-type majority specie

Figure 4.11: Simulated (a) and experimental (b) LDOS for the n-doped H_B configuration. The state located at around 0.25 eV below the Fermi level is due to the SDB and it is doubly occupied. The extra charge at the SDB site causes the upward band banding at top of the valence band. The state lying at around 0.1 eV above E_F, not present in the experimental data, is the first quantum well state and it is introduced in the calculation by the periodic boundary conditions. According to the color scale, the blue color corresponds to zero DOS (10^{-5} states/eV in the experiment) and the red color to a value of the DOS higher than 20 states/eV per supercell (0.1 states/eV in the experiment).

flipping event was previously reported in the works of Reusch *et al.* [220] and Radny *et al.* [219]. In contrast to the results shown here, their measurements were performed under RT STM imaging conditions and referred to low-doped Si(001) samples.

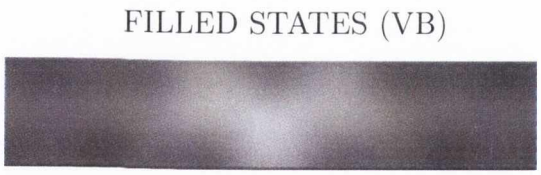

(a) EXP n-doped minority specie (-1.0 V)

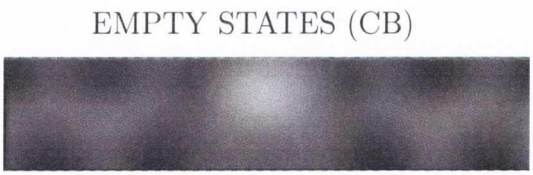

(b) EXP n-doped minority specie (+0.5 V)

Figure 4.12: Experimental topographic images for filled (a) and empty (b) states of the minority species. The filled-states image matches the H_B configuration while the empty-states one matches the H_T one (compare with Fig. 4.9). The change of the bias polarity is causing the entire dimer row to flip.

The n-doped H_T configuration shows a more complex scenario compared to the previous cases. The extra electron introduced by the doping gives rise to a spin polarized state located at the SDB site. The spin up and spin down levels are visible in the calculated band structure plot in Fig. 4.13, respectively as black filled and blue

filled circles. The spin up band is located at around 0.35 eV below the Fermi energy while the spin down one is at around 0.35 eV above it. The LDOS plot in Fig. 4.14

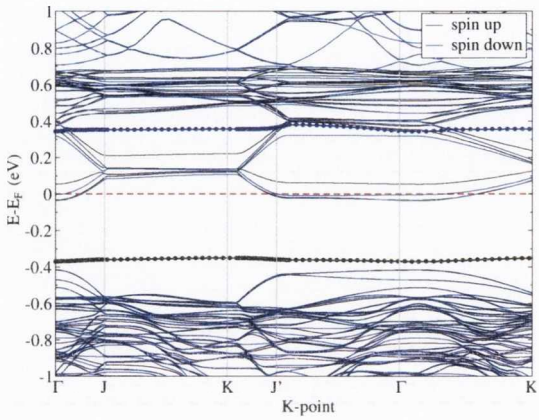

Figure 4.13: Calculated band structure for the n-doped H_T configuration. The filled circles bands are the spin polarized states coming from the extra electron introduced with the doping, and are mostly localized at the SDB site. The band crossing the Fermi level is the same found for the intrinsic case and it is due to an electron delocalized on the surface [see Fig. 4.4(b)].

shows the spin split states localized around the reacted dimer and a delocalized state around the Fermi energy. No band bending is visible, meaning that the SDB state is occupied with one electron [222]. The band across the Fermi energy has a very small spin splitting, that can be explained with the Stoner criterion [227].

DFT total energy calculations for n-doping conditions reveal that the H_B configuration is lower in energy by 136 meV with respect to the H_T one. This demonstrates that the majority configuration is indeed the lower-energy state, and that the minority one is metastable and stabilized by the pinning effect of neighboring defects. The stability of the majority species is not expected to vary for lower dopant concentrations, since calculations on the intrinsic neutral system still show the H_B lower in energy by 26 meV (see Tab. 4.1) [226]. These results are consistent with the results obtained by Reusch *et al.* [220] where, based on cluster calculations, the H_B configuration was found lower in energy by 260 meV and 30 meV for n-type and intrinsic conditions, respectively. Thus, while DFT topography and total-energy simulations provide a unique interpretation of the STM data for the H/Si(100) system, in the

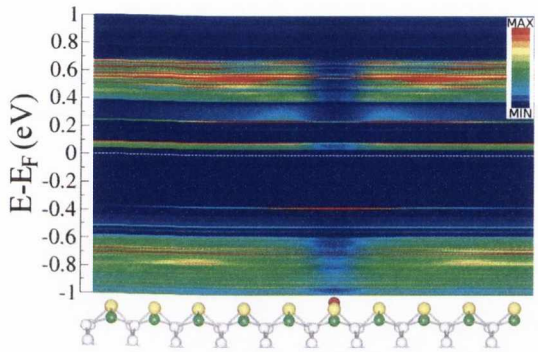

(a) n-doped H_T, spin-up LDOS

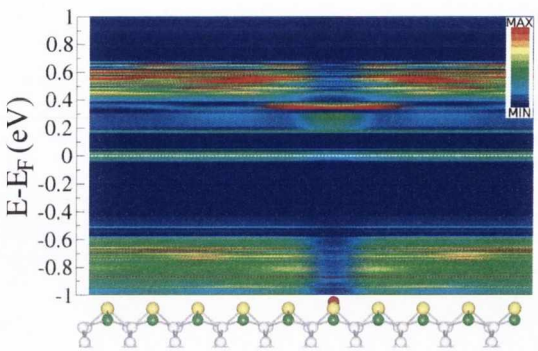

(b) n-doped H_T, spin-down LDOS

Figure 4.14: Spin up (a) and spin down (b) LDOS for the first row of the n-doped H_T configuration. No band bending is visible in the valence band, suggesting the SDB to be singly occupied. The spin split states, mostly localized at the SDB site, appear as a red spots at around 0.35 meV below E_F for the majority spin in (a), and around 0.35 meV above E_F for the minority spin in (b). According to the color scale, the blue color corresponds to zero DOS and the red color to a value of the DOS higher than 2 states/eV per supercell.

more general case, different adsorbate configurations may not show significantly different STM topographic signatures. Hence these necessitate a more detailed investigation of the electronic structure [226].

4.3.2 p-doping

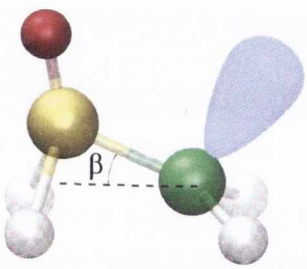

(a) p-doped H_T

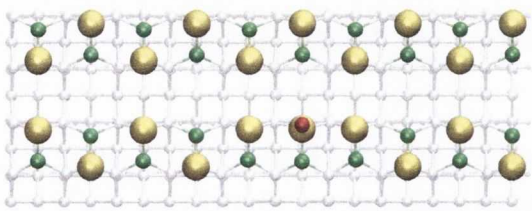

(b) H_{3DIM} configuration

Figure 4.15: Schematic representation of the reacted dimer for the p-doped H_T configuration (a). The dangling bond is empty. The p-doped H_B configuration relaxes into the H_{3DIM} one (b), with the reacted dimer tilted in phase with its nearest neighbours.

STM experiments of Si-Si-H hemihydrides on the Si(100) surface show the dangling bond appearing as a bright protrusion, while a depression is present on the

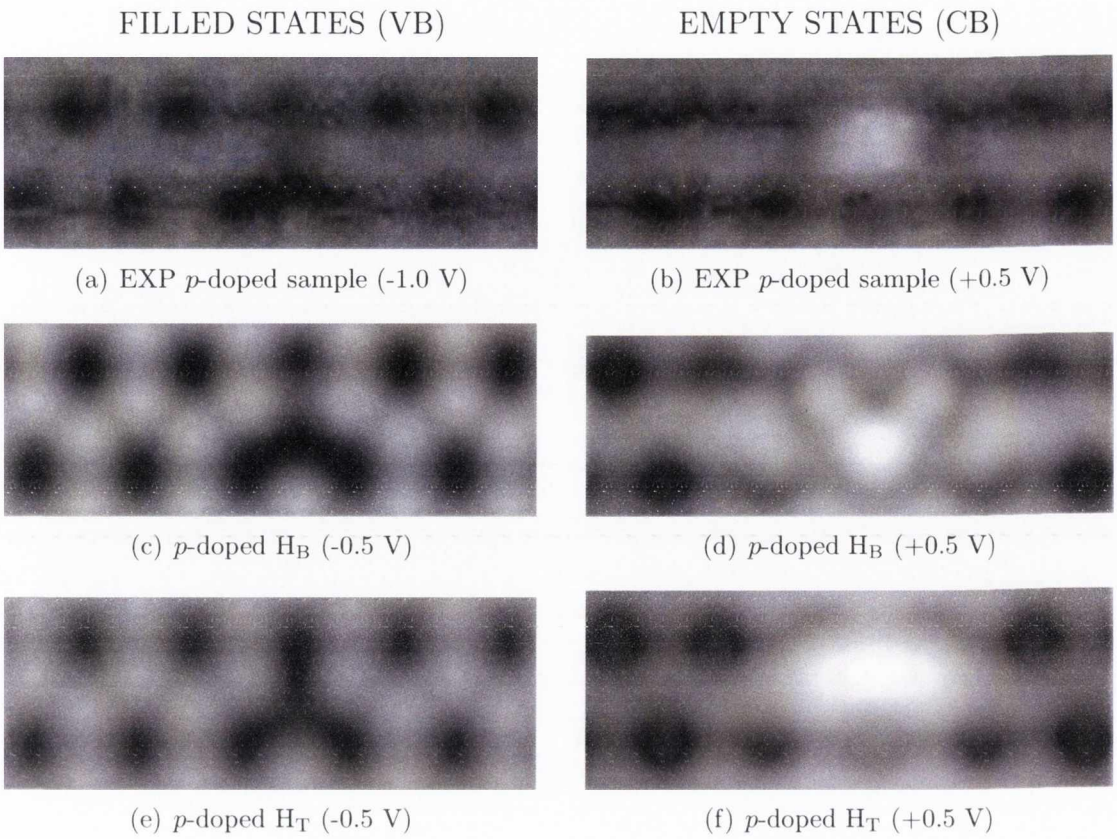

(a) EXP p-doped sample (-1.0 V)

(b) EXP p-doped sample (+0.5 V)

(c) p-doped H_B (-0.5 V)

(d) p-doped H_B (+0.5 V)

(e) p-doped H_T (-0.5 V)

(f) p-doped H_T (+0.5 V)

Figure 4.16: Top panels (a) and (b) are the experimental topographs for filled and empty states of the p-doped samples acquired for a sample bias of -1.0 V and +0.5 V respectively. Panels (c) and (d) are the corresponding simulated topographs for the H_B configuration. Panels (e) and (f) are the simulated topographs for the H_T configuration. The simulated data are referred to the reacted row (1^{st} row) of the 10×4 supercell and are obtained by considering a bias of -0.5 V and 0.5 V for filled and empy states, respectively. Bright areas correspond to a high DOS, while dark areas to low or null DOS. Only the H_T configuration reproduces the experimental empty states topography.

opposite side of the dimer, for both filled and empty states [224, 225]. A comparison between the experimental and the computed topographic images for p-doped systems shows the H_T configuration to best match the data (Fig. 4.16). In fact, although the simulated images for the filled states reveal that both H_T and H_B may agree with the experiments [compare Figs. 4.16(c) and 4.16(e) with Fig. 4.16(a)], only H_T reproduces the measured empty states topography as it can be seen by comparing Fig. 4.16(f) with Fig. 4.16(b). Our calculations show that, after a full relaxation, H_B undergoes an inversion in the dimer buckling, as reported in Tab. 4.1. Such a

new relaxed structure, called hereafter H_{3DIM} [see Fig. 4.15(b)], presents the reacted dimer tilted in phase relatively to its nearest neighbours. Total energy calculations predict H_T to be 111 meV lower than H_{3DIM} in good agreement with an energy difference of 140 meV previously reported [220]. This energy difference is mostly due to the structural distortion induced by the H_{3DIM} configuration, which is less efficient in accommodating the surface strain. This configuration has never been observed experimentally. The calculated local DOS and the STS image are in a good agreement and establish that the single dangling bond state is empty (Fig. 4.17). This is

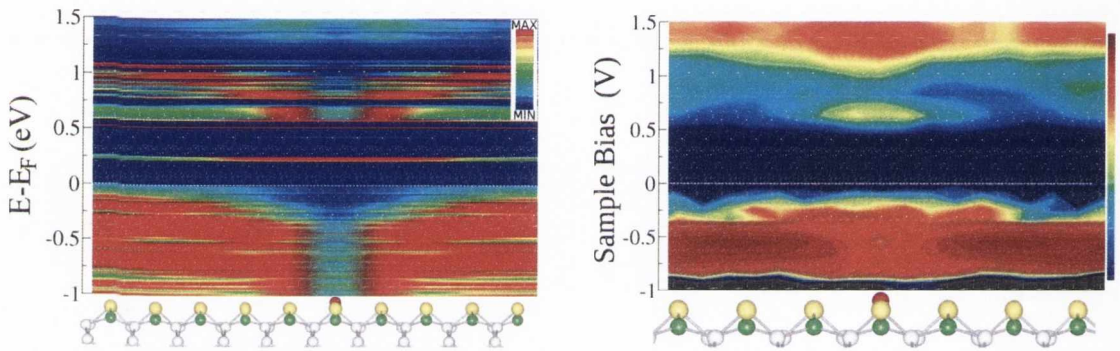

(a) p-doped H_T configuration (b) EXP p-doped sample

Figure 4.17: Calculated (a) and experimental LDOS (b) for the p-doped H_T configuration. The downward band bending of the valence band at the reacted dimer site is induced by a local positive charge, suggesting the SDB state to be empty. The SBD state is indeed located in the conduction band at around 0.2 eV above E_F for the calculated LDOS (a) and around 0.5 eV above E_F for the experimental one. According to the color scale, the blue color corresponds to zero DOS (10^{-5} states/eV in the experiment) and the red color to a value of the DOS higher than 1 states/eV per supercell (0.1 states/eV in the experiment).

confirmed by a pronounced downward band bending which is expected due to the positive charge around the SDB site (Fig. 4.17). The SDB state appears as a bright red spot around 0.2 eV above E_F for the calculated LDOS and around 0.5 eV in experiments at a spatial position corresponding to the H site (0 of the X axis in Fig. 4.17). The buckling angle of $\sim 11°$ suggests that the bonding configuration of Si atoms at the SDB site is sp^2-like, due to the absence of electrons at the SDB state [222].

4.4 Conclusion

In conclusion, DFT calculations together with STM/STS experiments allowed us to unequivocally characterize the geometry and the charging state of SDB on the Si(100) surface in different doping conditions. For *n*-doped conditions the H-produced SDB is doubly occupied with the H_B configuration being the lowest in energy. This configuration coincides with the majority species found in low temperature STM experiments. For *p*-doped samples the H_T configuration is the lowest in energy and the SDB state is empty. Finally, according to our calculations, the H_B configuration is still the lowest in energy for the neutral intrinsic case and the SDB state is partially occupied and spin-polarized. The buckling angle of the reacted dimer and, correspondingly, the bonding character of the Si atoms at SDB site reflects the occupation of the SDB state: i) an sp^3-like symmetry is found when the SDB is doubly occupied; 2) an sp^2-like symmetry corresponds to an empty SDB state; 3) a hybrid configuration in between the two is found for a partial occupation (one electron in the SDB state). Such an interplay between charging and geometry might open the interesting prospective of fabricating an atomic-scale switching device. In fact by tuning the surface doping from *p*-type to *n*-type one may switch between the two H configurations. These have distinct scattering and transport properties [226], thus the switch can be detected electrically. The surface doping can be tuned by a local gating of the SDB, for example by using the STM tip as an electrode. Another possibility is to create a depletion region in the surroundings of the SDB by applying an electric field through an electrode positioned at the bottom of the slab. It would work in the same fashion as the gate electrode of a FET transistor.

The scattering properties of the two configurations are discussed in the next chapter.

CHAPTER 5

Non-local approach and gating effects

5.1 Introduction

In this chapter the bonding configurations of a single H atom deposited on a bare Si(100)-c(4×2) surface will be described using the non-local approach (sec. 5.2), a general non intrusive method for studying the electronic structure and configuration of adsorbates on surfaces. The method makes use of the simulated and measured non-local DOS to map the scattered standing waves originating from the presence of adspecies. The simulated data are computed either with and without periodic boundary conditions along the dimer rows direction, by means of the VASP [169–173] and the SMEAGOL [110, 111, 168, 228] code, respectively.

The details of the calculations performed with VASP with periodic boundary conditions are the same as stated in Chapter 4.

The calculations with open boundary conditions were performed with a newly implemented order-N version of SMEAGOL which combines DFT with a recursive non-

equilibrium Green's function scheme built in the spirit of the embedding-potential method [229]. In this work we use the code only at equilibrium (0 bias) with the aim to avoid periodic boundary conditions along the dimer row direction, and therefore to simulate single impurities. The unit cell is constructed from the VASP-relaxed coordinates and it is 204.28 Å long along the dimer row direction (2377 atoms). The basis set includes a double ζ for the Si-s, Si-p, and H-s orbitals, and single ζ for the Si-d and H-p orbitals. No explicit doping is performed within the SMEAGOL code. Charge localization effects related to the doping are mainly determined by the details of the relaxed structure (e.g. dimer tilting angle), obtained by VASP. The system mantains its neutrality and a compensating neutralizing charge (with the opposite sign) can be found in a spread region in the proximity of the localized charge. This can be seen by comparing the total charge density for the undoped and doped relaxed structures.

In all the figures of this chapter I will use a color code for the balls-and-sticks supercell models where the yellow and green balls represent, respectively, the top and the bottom atoms of the surface Si dimers. The red color is used for the H atom on the surface. The simulated color DOS plots (LDOS) are obtained by assigning a coloured pixel to each atom position and for each energy value. The colour scale is set by the maximum (dark red) and minimum (blue) value of the DOS. The pixel is represented by a gaussian along the energy axis with a broadening of 0.01 eV. The broadening along the X axis is automatically applied by the image visualization software and it is a common procedure to all this kind of software. These parameters do not affect the features of the plots from a qualiltative point of view.

When a H atom is placed over the dimer, it passivates one of the dangling bonds of the surface Si dimer, breaking the Si-Si dimer π-bond and leaving an isolated dangling bond on the other side of the dimer. I will refer to the isolated dangling bond as the single dangling bond (SDB) [51]. The reacted dimer acts as a single scattering

center on the Si(100) surface when no periodic boundary conditions are applied. In contrast, the potential barrier originating from it gives rise to a quantum well when the system is treated with periodic boundary conditions. The reacted dimer induces gating effects on the adjacent rows of the reconstructed surface and the magnitude of the gating actions depends on the particular adsorption configuration. The results concerning the gating are discussed in section 5.3.

The results presented in Sec. 5.2 are calculated solely with the SMEAGOL code, by making use of the open boundary conditions. All the other results obtained from *ab initio* calculations, for each of the considered configurations, will be presented through this chapter according to the following order: firstly, the LDOS calculated with the VASP code, taking in account the periodic boundary conditions, will be presented, together with the PDOS bubble plots. Secondly, the LDOS calculated with the SMEAGOL code, without periodic boundary conditions, will then be presented.

5.2 Non-local approach

Many materials exhibit surface states that are effectively electronically decoupled from the bulk. The presence of surface adspecies induces scattering and the formation of standing-wave patterns in the local density of states (LDOS). This phenomenon was first demonstrated on the Cu(111) surface through the pioneering work of Eigler *et al.* [230] and Avouris *et al.* [231]. In this chapter I will consider a non-local approach to the general problem of identifying the bonding configuration of adspecies on surfaces. It consists of performing a spatial mapping of the amplitude and phase of the standing waves, a scheme which is extremely sensitive to the precise nature of the adsorption configuration. This method is based on measuring and computing the nonlocal DOS around the reacted site, and it is useful to build up a comprehensive picture of the adsorbate electronic structure and configuration. I will apply the method to the case of a single H atom on the n-doped Si(100)-c(4×2) surface, for

which, in principle, there exist two different adsorption configurations, H_B and H_T, described in the previous chapter and shown in Fig. 4.1. Both the species are also distinguishable using a combination of nonlocal, spatially resolved, scanning tunneling spectroscopy (STS) and density functional theory (DFT) simulations. This provides a new nonlocal approach for investigating surface structure and reactivity. Notably, a nonlocal measurement is less intrusive than a local one as the interaction between the scattering center and the STM tip is significantly reduced. As such, scattering centers, which switch at high frequency between different geometries under the influence of the STM tip, can be observed as stable in a nonlocal measurement [226]. Recent theoretical advances in the acquisition of the local electron density of states

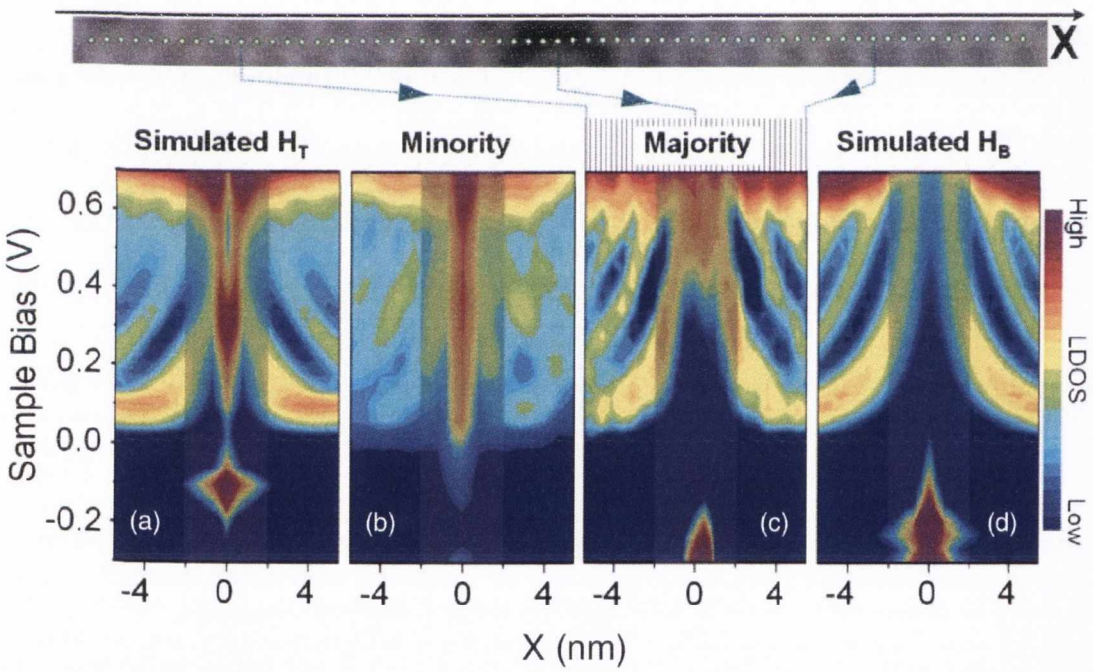

Figure 5.1: Spatial LDOS maps of the π^* standing waves along the Si dimer row with single-hydrogen occupied dimer at x = 0. The map of the majority species (c) was constructed from LDOS spectra recovered [66] from experimental dI/dV measurements taken on each point of the topographic image along the dimer row (x coordinate). The map of the minority species (b) was constructed as in (c). The same intensity (color) scale as in (b) and (c) was applied for the corresponding simulated LDOS maps for the n-doped H_T (a) and n-doped H_B (d) configurations [226].

(LDOS) from the STS data enable the direct comparison of spectra recorded at dif-

ferent lateral locations and tip-sample distances [66, 67]. This approach consists in constructing spatial LDOS maps, shown in Figs. 5.1(b) and 5.1(c), along the dimer rows that contain the reacted sites and over an energy range associated with the surface π^* band [66]. The band is split off from the bulk DOS and disperses strongly along the dimer row direction [see first LUMO band in Fig. 4.10(a)]. Hence it is sensitive to the presence of reacted scattering sites.

Experimental STM/STS measurements were performed using a Createc cryogenic system described elsewhere [66]. Both n-type (As, 0.001-0.005 Ωcm) and p-type (B, 0.001-0.005 Ωcm) Si(100) samples used are mounted on a triple sample holder containing also a Pt surface for tip preparation and recovery. *In-situ* Pt-inked tungsten probe [223] is used in the STM. Sub-monolayer atomic hydrogen coverage is deposited on the clean surface at 200 K via a heated tungsten capillary. The H atoms are manipulated by transferring them on and from the STM probe applying high biases (5-6 V) with different polarities. The spectroscopic results are obtained through variable-height scanning tunneling spectroscopy (VH-STS) [66] at 77 K. The LDOS maps were recovered from dI/dV measurements [64, 66], where the scans were made along the middle of the dimer row.

The experimental LDOS maps in Fig. 5.1 [panels (b) and (c)] show that the π^* band is strongly scattered by both types of H-atom species where Fig. 5.1(b) corresponds to the H_T and Fig. 5.1(c) to the H_B configuration. We simulate the LDOS of both by plotting the SMEAGOL density of states as a function of the atomic position, and present them in Figs. 5.1(a) and 5.1(d), for the H_T and H_B configurations, respectively. In the calculations, the DOS of the top and bottom Si dimer atoms are combined to reflect the experimental conditions, in which the measurements are made along the middle of the dimer row. Additionally, the theoretical bands in Fig. 5.1 have been shifted downwards by 0.125 eV in order to align the bottom of the calculated conduction band with the experimental one. For the H_B site, a compar-

ison between experiments and simulations[(Figs. 5.1(c) and 5.1(d)] reveals identical standing-wave patterns, produced by a potential barrier, and the presence of an intense doubly occupied single dangling bond (SDB) signature. This is consistent with the n-doping condition of the Si substrate [26].

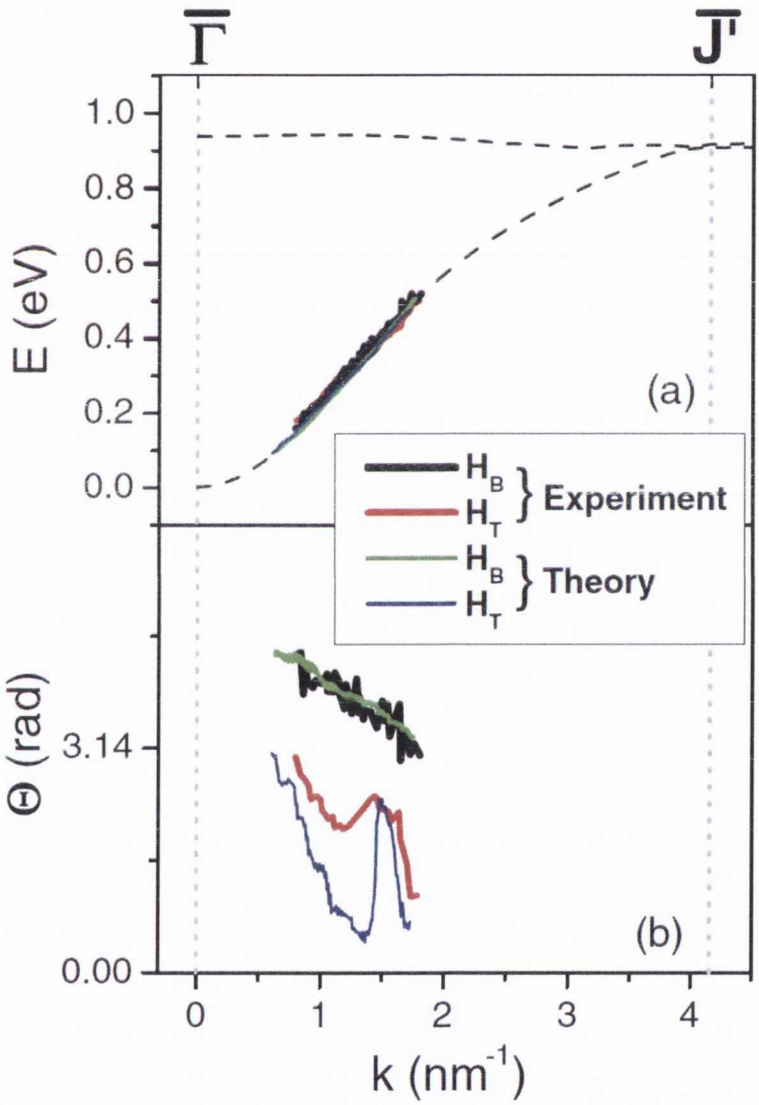

Figure 5.2: Fitting parameters for the standing waves. The energy dispersion $E(k)$ and the phase-shift dependence $\Theta(k)$ obtained by fitting the results in Fig. 5.1 are shown in (a) and (b), respectively. In (a), the simulated band dispersion for the bare surface is also presented (dashed line). The theoretical spectra have been shifted to align the bottom of the conduction band at 0 eV. Black, red, green, and blue lines are used for the results obtained from the LDOS maps in Figs. 5.1(c), 5.1(b), 5.1(d) and 5.1(a), respectively [226].

In the case of the H_T site, however, the SDB is singly occupied, as evidenced by

the filled and empty DB features in Figs. 5.1(a) and 5.1(b). The associated standing-wave pattern is significantly altered, revealing a nonmonotonic phase variation of the scattered waves that suggests the presence of a resonance in the potential barrier at the energy close to the half-empty SDB state. Again, the shape and position of the experimental H_T pattern in Fig. 5.1(b) matches the simulated one in Fig. 5.1(a). The excellent agreement between theory and experiments for the nonlocal characteristics of the surface further strongly supports the assignment of the majority sites to the H_B configuration [compare Figs. 5.1(c) and 5.1(d)] and the minority sites to the H_T configuration [compare Figs. 5.1(b) and 5.1(a)]. The absence of detected structural changes (dimer flipping) in the negative bias region in the spectra of the H_T configuration [see Fig. 5.1(b)] is due to the fact that the threshold for dimer flipping observed in the topographs [Figs. 4.9(e) and 4.9(f)] occurs at negative biases greater than -0.3 V sample bias [26].

In order to definitively establish the identity of the majority and minority species, it is possible to extract quantitative information from the LDOS scattering maps. By measuring the wavelength of the oscillations in the LDOS for different energies, E, in Fig. 5.1, we can obtain the band dispersion $E(k)$ and phase shift $\Theta(k)$.

To give an example of the procedure that our experimental collaborators followed to extrapolate such informations, let us consider the simulated LDOS image of the n-doped H_B configuration shown in Fig. 5.3(a). The LDOS profile can be extracted for a given energy (the black dashed line) and it is plotted in Fig. 5.3(b). By repeating the same procedure in the energy window where the standing waves are, it is possible to obtain the phase shift by fitting the LDOS profiles to the following expression

$$LDOS \propto |\psi(x)|^2 \propto 2A^2 \left[1 + 2cos(2kx + \Theta)\right] + e^{-\frac{x}{L}}, \tag{5.1}$$

where ψ is the surface state wave function with amplitude A and $x = 0$ is set at the position of the H atom. The exponential term accounts for the decay of the wave

function far away from the scattering center (L is the length of the sample/supercell). The equation used for the fitting can be easily derived by considering the standing wave pattern obtained by solving the Schrödinger equation for a potential step[1].

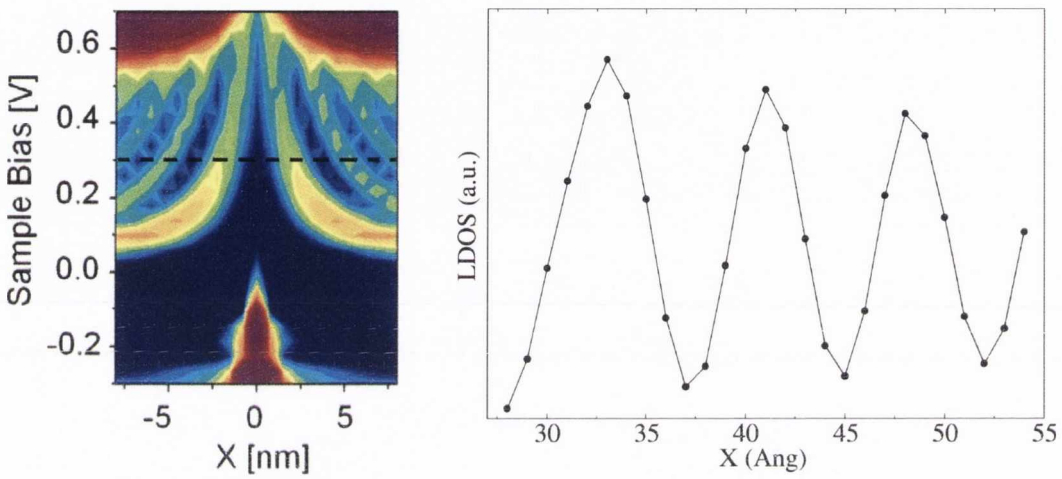

(a) Color DOS (b) DOS profile

Figure 5.3: Simulated color DOS of the first row of the n-doped H_B configuration, calculated without periodic boundary conditions (a). The DOS profile can be extracted for each value of the energy (b). By fitting the DOS profile with a cosine function, it is possible to extract information about the band dispersion and the phase shift of the standing waves.

The dispersion $E(k)$ is plotted in Fig. 5.2(a) for the data obtained from the maps of Figs. 5.1(a)-5.1(d). The theoretical π^* band dispersion along the dimer row for the bare surface is also plotted (dashed line) in Fig. 5.2(a). The dispersions obtained for the majority and minority sites agrees well with each other and the simulation for the H_B and H_T configurations, demonstrating that the scattering phenomena is an intrinsic property of the π^* band. However, the phase shifts $\Theta(k)$ of the wave function scattered from the majority and minority sites are dramatically different and provide a unique signature, which allows us to distinguish between the two H configurations. The majority-site phase shift [black spectrum in Fig. 5.2(b)] decays monotonically with k, whereas the minority species [red curve in Fig. 5.2(b)] show a different slope and a pronounced minimum associated with a resonance in the scattering barrier. A

[1]A detailed derivation is given in appendix A

comparison with the simulated phase shifts associated with scattering from the H_B (green) and H_T (blue) sites establishes once again that these configurations can be assigned to the majority and minority species, respectively. The observed differences between the experiment and simulated phase shift for the minority site likely reflect the need for a stabilizing defect in the adjacent area, which was not accounted for in these simulations. The experimental (black) and the simulated (green) results for the majority species show a $\Theta(k)$ dependence that is approximately linear with negative slope, suggesting a triangular-shaped barrier, in agreement with the displacement of the conduction-band edge around the scattering site [Figs. 5.1(c) and 5.1(d)]. For the minority configuration, the strong resonance in the barrier [see Figs. 5.1(a) and 5.1(b)] is clearly detected in the phase-shift spectrum [red and blue curves in Fig. 5.2(b)] and underlines the increased transmission coefficient at the resonance position, leading to significant reduction of the phase shift. Clearly, the latter reflects the fact that in the case of H_T configuration, the dangling bond is half filled, causing it to interact with the scattered charge density [226].

5.3 Gating Effects

Gating is usually referred to the ability of changing, in a controlled manner, the electronic properties of a device. By applying a voltage to the gate electrode of a MOSFET transistor, for example, it is possible to switch it on and off. In this case the gating effect is due to an electric field, originated by the applied bias, that allows or impedes the flow of carriers along the channel connecting source and drain. This type of gating allows a direct and full control of the device. Our definition of gating assumes a more general meaning. We define the gating effect as a way of modifying the electronic porperties of a system in a measurable way even if the exact details related to the magnitude of the effect are not known.

Different charging configurations of the SDB modify the electronic properties of

the adjacent (bare) row giving rise to gating effects of different magnitude. These variations in the electronic properties of the system can be measured and assigned to different configurations. One should be able, in principle, to control the charging state of the SDB and hence to control, in an indirect way, the electronic properties of the bare dimer row by switching it between different configurations.

The reacted dimer induces gating on the bare dimer rows adjacent to that containing the scattering center. This depends on the H adsorption configuration and hence the nature of the SDB. The gating effect is remarkable in the case of the n-doped H_B configuration, while it is less effective in the case of the n-doped H_T configuration and it is negligible in the case of the p-doped H_T. When considering the supercell used for the simulations, I will refer to the first row as the one containing the reacted dimer, while the second row is the bare one just adjacent to it as in Fig. 4.1. The LDOS plots, shown in Fig. 5.4, let us compare the LDOS measured on the first and the second row of the n-doped H_B configuration, respectively. The pronounced upward band bending [Fig. 5.4(a)] present in the first row at the

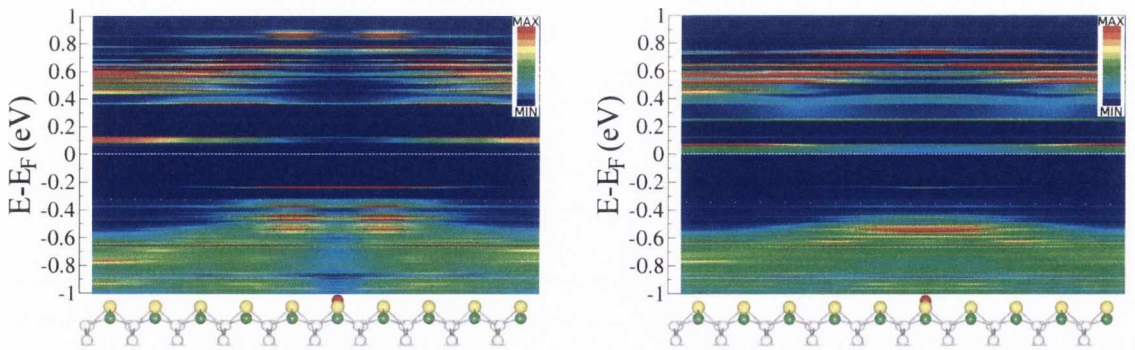

(a) Reacted row (b) Bare row

Figure 5.4: LDOS of the first (a) and second (b) row of the n-doped H_B configuration, calculated by taking into account the periodic boundary conditions. A noticeable band bending is induced in the second row, due to the extra charge at the SDB site in the first row. A modulation of the DOS intensity is visible also for the first LUMO state in the second row, suggesting the effectiveness of the gating effect in this configuration. According to the color scale, the blue color corresponds to zero DOS and the red color to a value of the DOS higher than 80 states/eV per supercell.

site position corresponding to the reacted dimer, extends to the second row, meaning that the effect of the extra charge of the SDB influences the adjacent row [see Fig. 5.4(b)]. The LDOS relative to both the dimer rows exhibit a modulation of the first LUMO states in the conduction band (Fig. 5.4) suggesting that the effects of the confining potential due to the reacted dimer are affecting the adjacent row. This is confirmed by the PDOS standing wave pattern for the reacted and bare dimer row shown in Fig. 5.5. Due to periodic boundary conditions the potential barrier

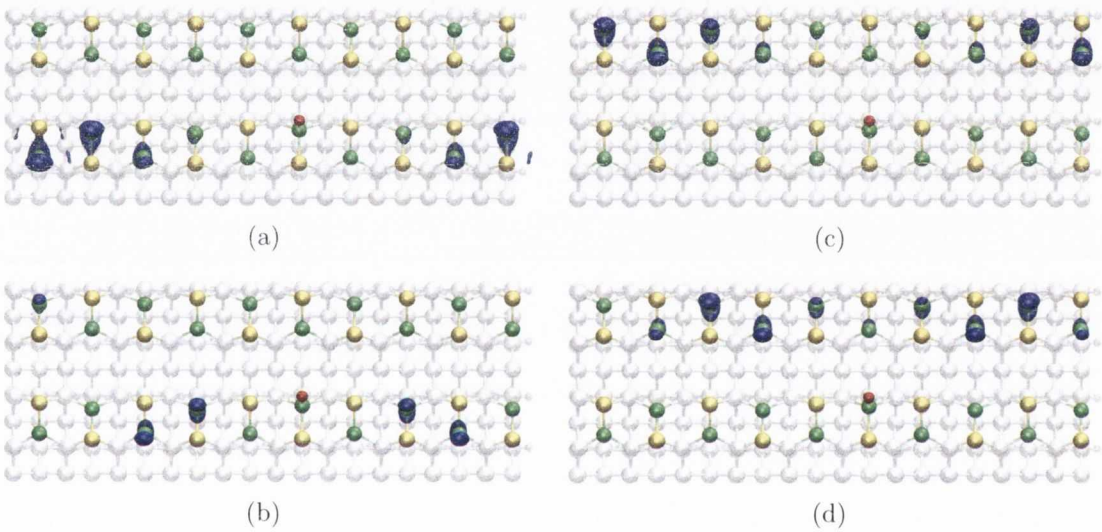

Figure 5.5: PDOS of the n-doped H_B configuration calculated by taking into account the periodic boundary conditions. The potential barrier originating from the reacted dimer, together with its periodic image, gives rise to quantum well states in the conduction band associated to the first dimer row. The first and the second quantum well states are shown in panel (a) and (b), respectively. The similar standing wave pattern in the second row [panel (c) and (d)] originates from a remarkable gating effect induced by the tail of the confining potential created by the reacted dimer in the first row.

gives rise to quantum well states: the PDOS of the first LUMO states corresponds, respectively, to the first nodeless quantum well state [Figs. 5.5(a) and 5.5(c)] and the one-node standing wave [Figs. 5.5(b) and 5.5(d)]. These results are confirmed by the simulations performed without boundary conditions along the dimer rows, where the reacted dimer acts as a single scatterer.

The simulated LDOS for the first and second row are shown in Figs. 5.6(a)

and 5.6(b), respectively. The supercell used for the calculations comprises two dimer rows likewise the one shown in Fig. 4.1, and it is 12 *nm* long. Several orders of standing waves can be observed. The band bending due to the extra charge at the reacted site and the gating effects are visible and in good agreement with the calculations previously shown [222].

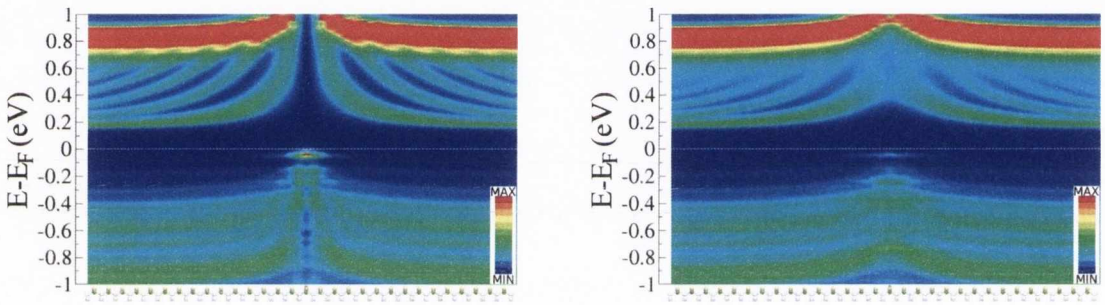

(a) Reacted row (b) Bare row

Figure 5.6: LDOS of the first (a) and second (b) row of the *n*-doped H_B configuration, calculated without periodic boundary conditions. The reacted dimer acts as a single potential barrier for the conduction band states. The upward band bending and the standing wave pattern present in both the dimer rows witness a remarkable gating effect. According to the color scale, the blue color corresponds to zero DOS and the red color to a value of the DOS higher than 1 state/eV per supercell.

The gating effect is less pronounced in the case of the *n*-doped H_T configuration. The LDOS plots for the first and second dimer rows are shown in Figs. 5.7(a) and 5.7(c) for the majority spin and in Figs. 5.7(b) and 5.7(d) for the minority spin states. No band banding is present, in agreement with the single occupation of the SDB state. A modulation of the LDOS is visible in the first LUMO states of the first dimer row, while it is much less pronounced in the adjacent row. The PDOS pattern shows the fingerprint of the first quantum well state (nodeless standing wave) in the LUMO states localized in the first row [see Fig. 5.8(a)]. The HOMO and LUMO levels around the Fermi energy on the second row, show a slightly modulated pattern of the PDOS, which cannot be addressed to quantum well states [Figs. 5.8(c) and 5.8(d)].

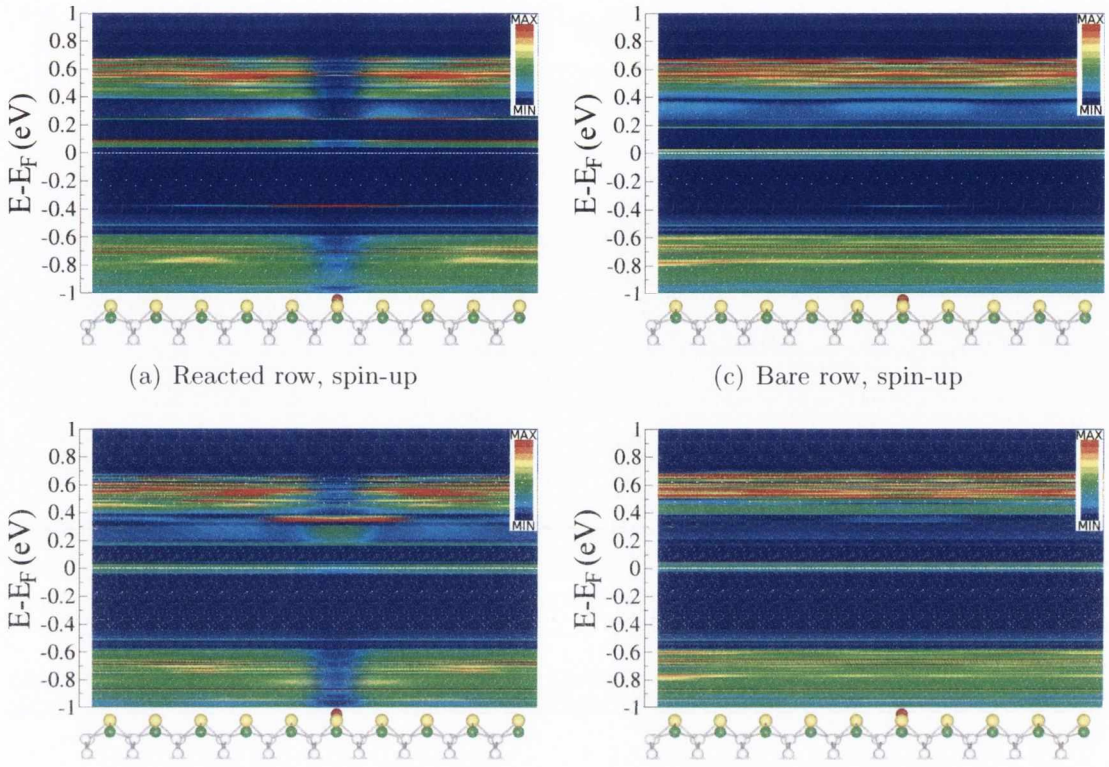

(a) Reacted row, spin-up

(c) Bare row, spin-up

(b) Reacted row, spin-down

(d) Bare row, spin-down

Figure 5.7: LDOS of the n-doped H_T configuration, calculated with periodic boundary conditions. The spin-up LDOS is shown for the first (a) and second (c) row. The spin-down LDOS for the first and second row is shown in (b) and (d) respectively. No band bending is visible in the plots and the modulation of the LDOS in the first LUMO states of the conduction band is much less pronounced with respect to that observed for the H_B configuration. This suggests a negligible gating between the reacted dimer row and a bare adjacent one. According to the color scale, the blue color corresponds to zero DOS and the red color to a value of the DOS higher than 5 states/eV per supercell.

The LDOS plots for the first [Fig. 5.9(a)] and second [Fig. 5.9(b)] dimer rows, calculated without periodic boundary conditions, show standing wave patterns at the reacted row while the same pattern is much less pronounced in the bare adjacent row. This confirms the reduced gating activity of this configuration with respect to n-doped H_B.

The gating effect is absent in the case of the p-doped H_T configuration. The LDOS for the first row, shown in Fig. 5.10(a), exhibits a downward band bending in agreement with the positively charged SDB. A downward band bending of reduced

Figure 5.8: HOMO and LUMO states around the Fermi energy for the n-doped H_T configuration, calculated with periodic boundary conditions. A pattern modulation, corresponding to the first quantum well state, can be seen in the first row LUMO state (a). The magnitude of the pattern modulation is quite reduced in the HOMO (d) and LUMO (c) states on the second row and no standing wave pattern can be identified.

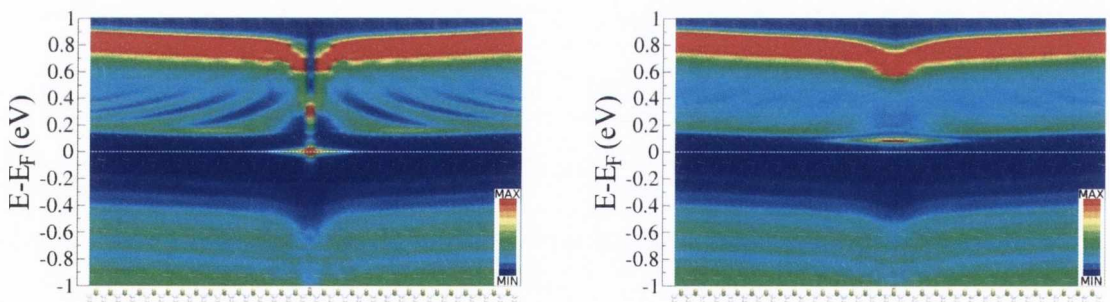

(a) Reacted row (b) Bare row

Figure 5.9: LDOS of the first (a) and the second (b) row of the n-doped H_T configuration calculated without periodic boundary conditions. The standing wave pattern in the first row is not clearly identifiable in the second row, meaning that the gating effect is much less pronounced in this configuration with respect to the n-doped H_B one. According to the color scale, the blue color corresponds to zero DOS and the red color to a value of the DOS higher than 1 state/eV per supercell.

magnitude is also visible in the second row [see Fig. 5.10(a)] meaning that the potential due to the positively charged SBD is somehow affecting the adjacent row. Apart from the band bending, the second row does not show any sign of intensity modula-

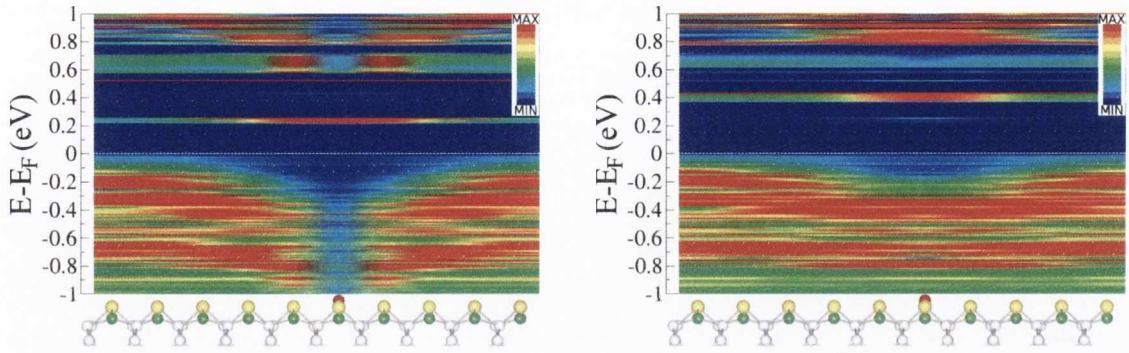

(a) Reacted row (b) Bare row

Figure 5.10: LDOS of the first (a) and second row (b) of the *p*-doped H_T configuration, calculated by making use of the periodic boundary conditions. The second row shows an induced band bending due to the potential originating from the positively charged SDB at the first row. The modulation of the intensity of the LDOS for the first LUMO states cannot be addressed to any standing wave feature. According to the color scale, the blue color corresponds to zero DOS and the red color to a value of the DOS higher than 2 states/eV per supercell.

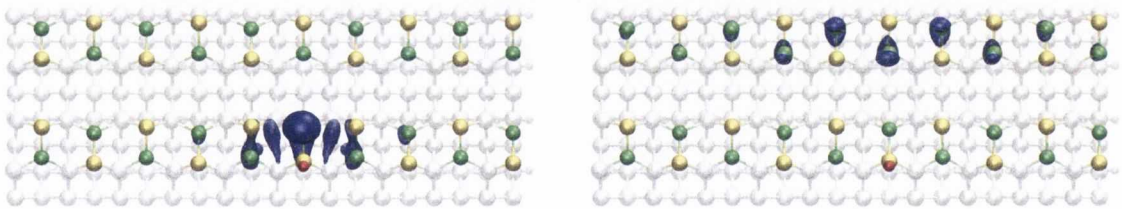

(a) (b)

Figure 5.11: PDOS of the first LUMO states of the *p*-doped H_T configuration, calculated with periodic boundary conditions. The first LUMO state (a) is mostly localized at the SDB site. The second LUMO state (b), in the second row, shows its maximum intensity at a position corresponding to the SDB, excluding the possibility of any gating effect.

tion of the DOS that can be attributed to standing wave states. This is confirmed by the PDOS, calculated for the first LUMO states and shown in Figs. 5.11. The first LUMO state is mostly localized at the SDB site [see Fig. 5.11(a)] while the second one, on the second row, shows a maximum at the position corresponding to the SDB. At this position an effective gating, originating from the reacted dimer at the first row, would produce a depletion zone in the LDOS which is absent in Fig. 5.11(b). This is a clear indication that there is no confining potential affecting the second

row, and thus, no gating effect is detected.

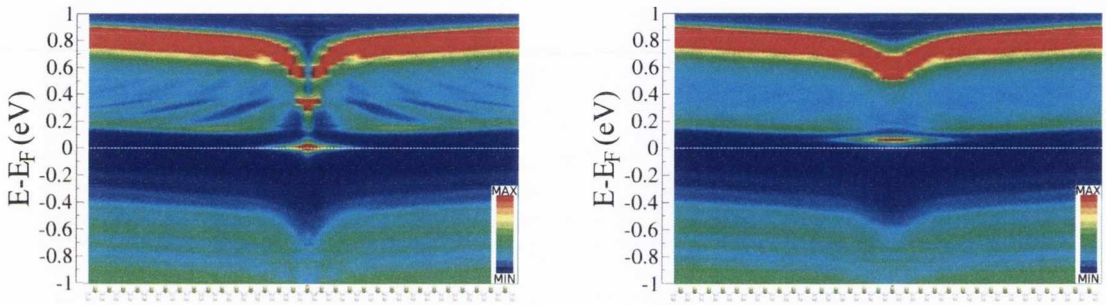

(a) Reacted row (b) Bare row

Figure 5.12: LDOS of the first (a) and second (b) row of the *p*-doped H_T configuration calculated without periodic boundary conditions. The standing wave pattern on the first row is not identifiable in the second row, suggesting a nearly absent gating effect. According to the color scale, the blue color corresponds to zero DOS and the red color to a value of the DOS higher than 1 state/eV per supercell.

The calculated LDOS without periodic boundary conditions for the first and second row are shown in Figs. 5.12(a) and 5.12(b), respectively. In agreement with the results previously shown, no gating effect is seen.

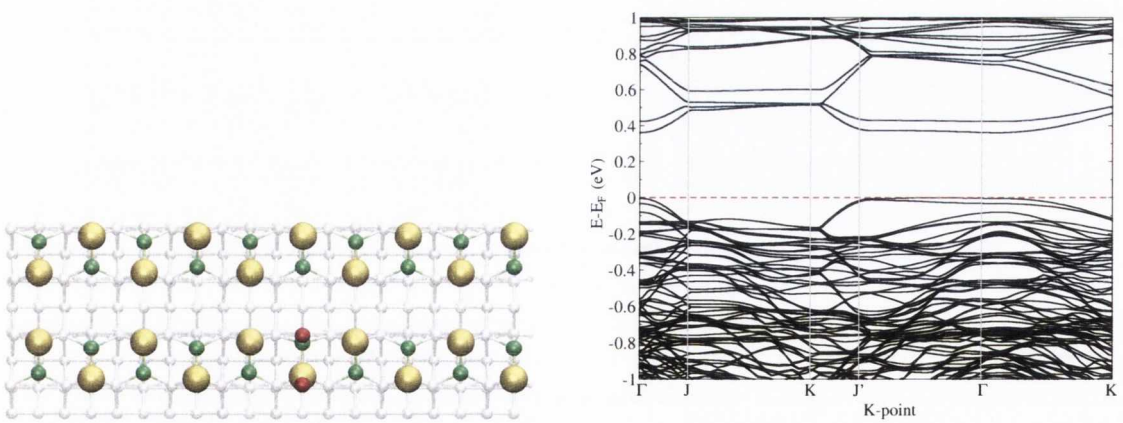

(a) 2H configuration (b) Band structure

Figure 5.13: Balls-and-sticks model (a) and band structure (b) of the 2H configuration. A surface dimer is completely passivated with two H atoms.

It is worth to compare the previous configurations with what it is named the 2H configuration, where both the Si atoms of the same dimer are passivated with H [see Fig. 5.13(a)]. This configuration has no SDB associated to the reacted dimer

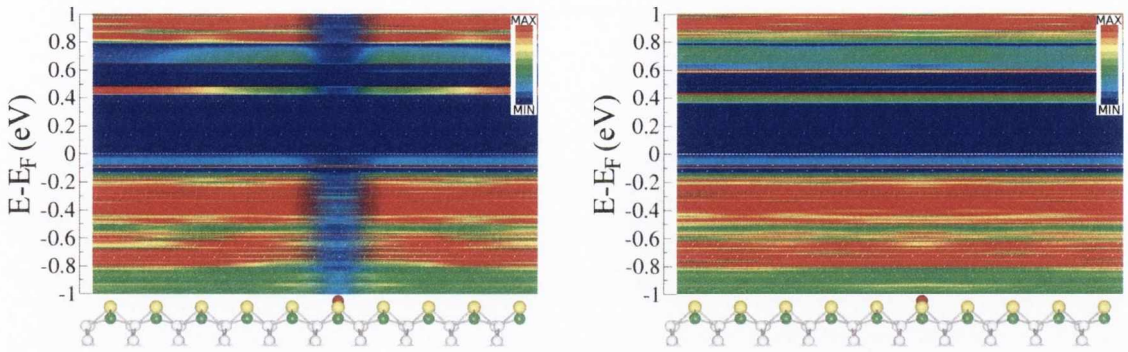

(a) Reacted row (b) Bare row

Figure 5.14: LDOS of the first (a) and the second row (b) of the 2H configuration, calculated with periodic boundary conditions. The DOS of the first LUMO states is modulated by the confining potential of the reacted dimer in the first row (a). No gating effect, and consequently, no modulation of the DOS is detectable in the second row (b). According to the color scale, the blue color corresponds to zero DOS and the red color to a value of the DOS higher than 2 states/eV per supercell.

and the LDOS for the first and the second row, shown respectively in Figs. 5.14(a) and 5.14(b), exhibit a modulation of the first LUMO states only in the first row while it is negligible in the second one. This is confirmed from the PDOS plots of the first LUMO states (Fig. 5.15).

The first and the second quantum well states are clearly identifiable on the first row [Figs. 5.15(a) and 5.15(b)], indicating that the reacted dimer is acting as a potential barrier. The modulation of the PDOS on the second row [plots 5.15(c) and 5.15(d)], does not possess any standing wave feature, indicating that the tail of the confining potential on the first row is not affecting the second one. The LDOS calculated with the SMEAGOL code, without periodic boundary conditions along the dimer rows, shows a clear standing wave pattern in the first row [Fig. 5.16(a)], confirming the fact that the reacted dimer is acting as a potential barrier for the π^* surface electrons. Such a pattern is not clearly identifiable in the second row or its magnitude is much lower than the one found for the single H configurations, suggesting that the gating effect on the adjacent row is neglibible [Fig. 5.16(b)].

While the passivating H ions at the reacted dimer, together with the charge

Figure 5.15: PDOS for the first LUMO states of the 2H configuration. The first (a) and the second (b) quantum well states are clearly identifiable on the first row. The modulation of the PDOS on the second row (plots (c) and (d)), does not possess any standing wave feature, indicating that there is no gating between adjacent rows.

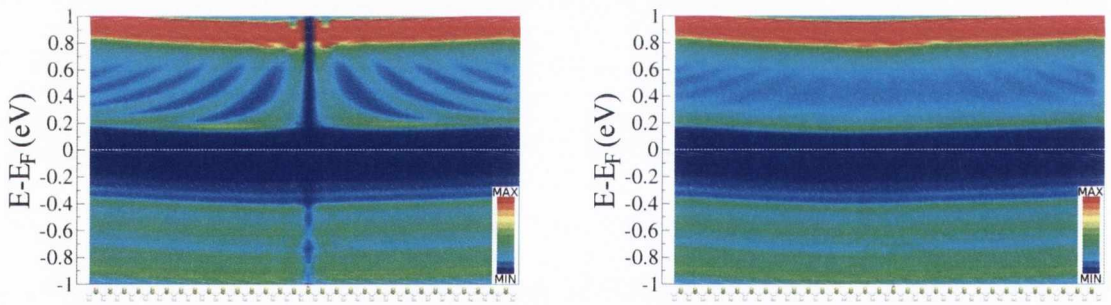

(a) Reacted row (b) Bare row

Figure 5.16: LDOS of the first (a) and the second row (b) of the 2H configuration, calculated without boundary conditions. A clear standing wave pattern is visible in the first row (a), due to the reacted dimer acting as a potential barrier. This potential barrier is not gating the second row (b), where the amplitude of the standing wave pattern is negligible. According to the color scale, the blue color corresponds to zero DOS and the red color to a value of the DOS higher than 1 state/eV per supercell.

present at the SDB, are responsible for creating a potential barrier that scatters the π^* surface electrons in the reacted row, the gating effect can only be attributed to the SDB state. The single dangling bond is then responsible for the gating effect on the adjacent row and the magnitude of the gating is related to the symmetry and

the charging of the dangling bond orbital.

In the case of the n-doped H_B configuration, the SDB orbital has a p-character, it is doubly occupied and its lobe shape is pointing towards the adjacent row. The effect of the Coulombic repulsion due to the extra charge extends to the adjacent row, generating a potential barrier for the electrons travelling along that row. In contrast, the SDB orbital has a s character in the n-doped H_T configuration and it is singly occupied. Due to the less directional nature of the s orbital and the reduced Coulombic repulsion coming from the only electron occupying the SDB state, the gating effect on the bare adjacent row is less pronounced if compared to the H_B case. The SDB orbital is empty for p-type system and it has no preferable direction (spheric symmetry). This, together with the lack of Coulombic repulsion due to the absence of negative charge at the SDB site, results in a negligible gating on the adjacent dimers row [232]. The 2H configuration has no SDB associated and, indeed, no gating effect is detectable.

5.4 Conclusions

In this chapter I have described the nonlocal approach to the investigation of the electronic and structural properites of surface adspecies and its ability to characterize adsorbates by means of the nonlocal spatial LDOS mapping. This nonlocal technique has been applied to study the majority and minority H-atom species adsorbed on the n-type Si(100)-$c(4 \times 2)$ surface. The combined results obtained from experimental STS and DFT simulated data are supported by the local approach (adspecies electronic structure) and STM data described in chapter 4. This novel nonlocal spatial LDOS mapping technique is a powerful addition to the standard STM tools, with the significant advantage of being able to characterize systems in their nonperturbed states, i.e. when the tip little affects the measurements. As such, it is expected to be useful for the investigation of molecule and complex-surface

configurations, where the topographic signatures of different configurations are indistinguishable or in instances where there are no STM-accessible states within the tunneling energy window. Furthermore, as the nonlocal approach barely perturbs the scattering center, it can be used to characterize adsorbate geometries that are mechanically unstable under the STM tip.

The configuration and charging state of the SDB is responsible for gating the bare adjacent row. The magnitude of the gating is proportional to the charging of the SDB and to the directionality of the SDB orbital. The n-doped H_B configuration is doubly occupied and the p character of the SDB orbital results in a pronounced gating effect on the adjacent dimer row. This effect is less pronounced in the n-doped H_T case, where the SDB is singly occupied and the orbital has an s symmetry. Finally, the gating effect is almost absent in the p-doped H_T case due to the lack of negative charge at the SDB site. The fact that the gating effect is due to the single dangling bond is confirmed by comparison with the 2H configuration.

CHAPTER 6

Topological Insulators

6.1 Introduction

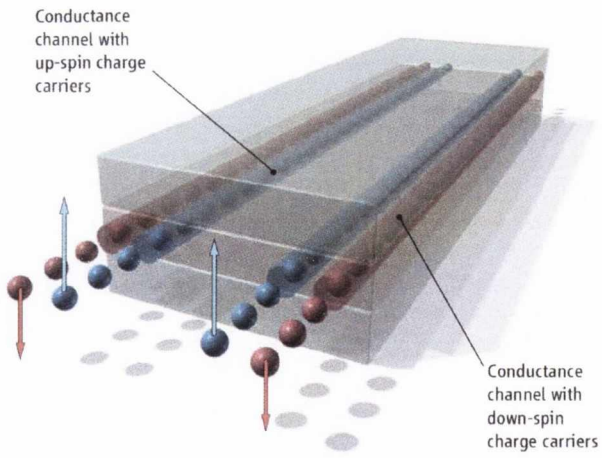

Figure 6.1: Schematic representation of the spin-polarized edge channels in a quantum spin Hall insulator [233].

Topological insulators (TI) are a new class of materials that have been attracting the interest of condensed matter physicists in the past years due to their peculiar properties and very promising variety of applications [233–246].

In the last part of this thesis I will discuss preliminary results on the electronic properties of a Bi_2Se_3-based systems, classified as a second generation topological insulator [247]. The work is still in progress and consists in determining the electronic properties of a thin film of Bi_2Se_3, epitaxially grown on a single layer Graphene substrate. I will present some preliminary result aimed to study the evolution of the band structure in such a system as a function of the separation distance of the interface, without entering into the details related to the determination of the topological invariants. The graphene-Bi_2Se_3 heterostructure has been investigated by means of *ab initio* DFT-based calculation, performed with the VASP code. First of all, I will present a very general overview of the properties of this new class of materials.

Topological insulators (TIs) are a new class of materials that show a bulk band gap like an ordinary insulator but have protected conducting states at their edges or surfaces. The surface (or edge in 2D) of a TI has gapless states, protected by time-reversal symmetry leading to a conducting state that has no equal in any other known 1D or 2D electronic system. In addition to their fundamental interest, these states are predicted to have special properties that could open interesting perspectives in a wide range of applications, ranging from spintronic to quantum computation [248].

Until 1980 the spontaneous breaking of symmetry (translational, rotational, etc) has been used as a criterion to classify all the different known states of matter such as crystalline solids, magnets and superconductors. In 1980, the quantum Hall (QH) state was discovered and it provided the first example of a quantum state without a spontaneous symmetry break [249]. Subsequently a new class of topological states emerged, called quantum spin Hall (QSH) or topological insulators [250, 251]. These have been theoretically predicted and experimentally observed in a number of systems such as HgTe quantum wells [233, 241], $Bi_{1-x}Sb_x$ alloys [236, 242] and both Bi_2Se_3 and Bi_2Te_3 bulk crystals [244–246, 252]. QSH systems are insulating in the bulk with

an energy gap between the highest occupied state and the lower unoccupied state but they have gapless edges or surface states at the boundary. These are topologically protected by time-reversal (TR) symmetry and immune to impurities or geometric perturbations [234, 237, 238, 240, 251, 253–255]. While in the case of QH states an external magnetic field is required to break the time-reversal symmetry, the QSH states are time-reversal invariant and do not require an external field [256].

6.2 From quantum Hall to quantum spin Hall

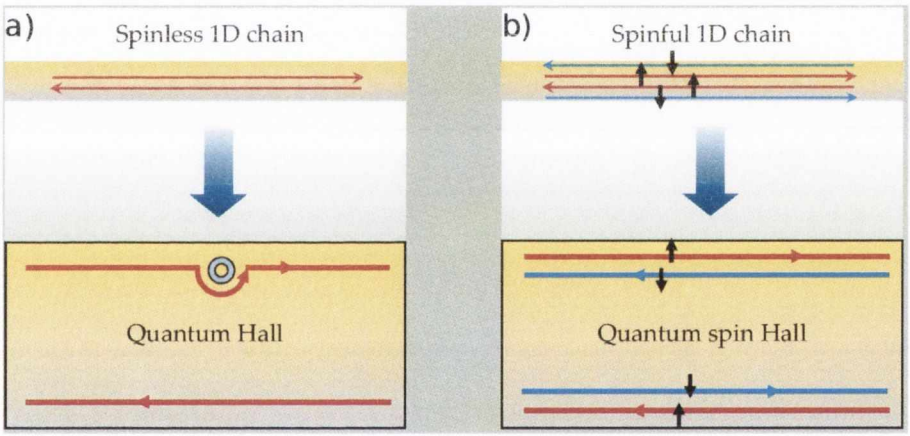

Figure 6.2: Carriers spatial separation is at the basis of both the quantum hall and quantum spin hall effects. (a) A spinless 1D system has two basic degrees of freedom corresponding to electrons moving forward and backward. They are spatially separated with the forward mover at the upper edge of the sample and the backward mover at the lower edge. These states are robust against scattering and the mover is able to go around an impurity without scattering. (b) A spinful 1D system has four basic channels, corresponding to forward and backward movers with up and down spin. These channels are spatially separated in a QSH bar, the upper edge containing a forward mover with spin up and a backward mover with spin down at the upper edge. The opposite happens at the lower edge [256]. Image from Ref. [256].

The QH effect occurs when a strong magnetic field is applied to a 2D gas of electrons in a semiconductor [249, 257, 258]. At low temperature and high magnetic field, electrons traveling along the edge of the semiconductor, are spatially separated in two counterflows located at the top and bottom edge of the sample. Compared

with a 1D system with electrons propagating in both directions, each edge of a QH bar contains half the degrees of freedom, as shown in Fig. 6.2(a). This separation of "lanes" is the key reason for the robustness of the QH state. Let us consider an electron belonging to an edge state and moving from left to right like in Fig. 6.2(a). When the electron encounters an impurity, it takes a detour around it and still keeps going in the same direction. The back scattering is indeed impeded by the applied magnetic field [259] (see the bottom panel of Fig. 6.2). The applicability of this dissipationless transport mechanism, extremely useful for semiconductor devices, is limited by the requirements of a large magnetic field.

In a real 1D system, forward and backward moving electrons for both spin up and spin down give rise to four channels as shown in Fig. 6.2(b). In a QSH state the lanes for the electrons can be split in a TR-invariant fashion due to the spin-orbit interaction, which plays the role of the external magnetic field in the QH state [234, 251, 253]. In the QSH state the spin up forward mover and the spin down backward mover are located at the top edge of the sample while the other two electrons corresponding to the remaining channels move at the bottom edge. QSH states are protected against backscattering from nonmagnetic impurities. By analogy with a photon, that can be reflected by a surface, an electron can be reflected by an impurity and different reflection paths can interfere with each other. In the case of an antireflection coating, the light beams reflected from the top and the bottom surfaces interfere with each other destructively, leading to zero net reflection and perfect transmission [Fig. 6.3(b)]. An electron in a QSH state can detour the non magnetic impurity by taking a clockwise or anticlockwise turn. Along the turn its spin rotates by an angle of π or $-\pi$ depending on the direction of rotation, as shown in Fig. 6.3(a). Consequently the two paths, related by TR-symmetry, differ by a 2π rotation of the electron spin in such a way that they interfere destructively according

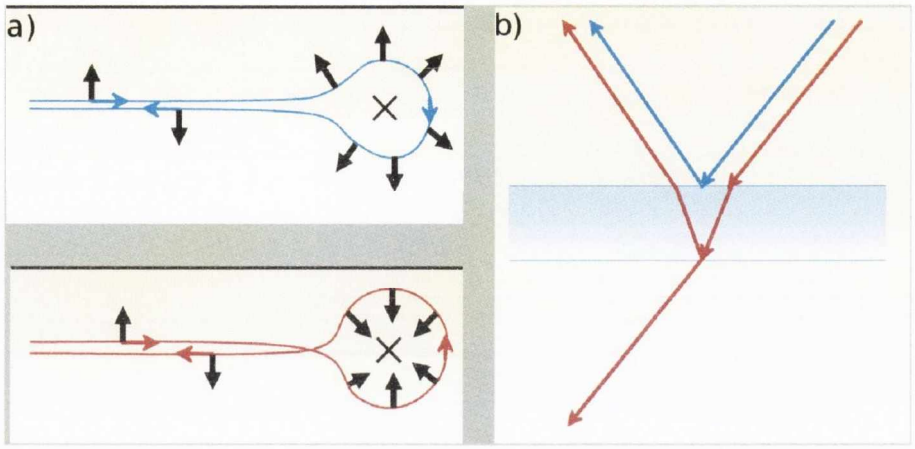

Figure 6.3: A quantum spin Hall edge state can be scattered in two directions by a nonmagnetic impurity (a). Going clockwise along the blue curve, the spin rotates by π; counterclockwise along the red curve, by $-\pi$. A quantum mechanical phase factor of -1 associated with a difference of 2π leads to destructive interference of the two paths. In this way the backscattering of electrons is suppressed similarly to what happens to photons off an antireflection coating (b) [256]. Image from Ref. [256].

to a principle of quantum mechanics[1], leading to a perfect transmission. In the case of magnetic impurities, the TR symmetry is broken and the two reflected waves no longer interfere destructively. In that sense the robustness in the QSH state is protected by the TR symmetry [256]. There is another requirement for the QSH state to conserve its robustness: the edge states must consist of an odd number of forward movers and an odd number of backward movers. If there are two forward movers and two backward movers, like in the 1D system of Fig. 6.2(a), the electron can be scattered from a forward to a backward moving channel without reversing its spin so that the interference is no longer destructive. The odd-even effect is characterized by a so called Z_2 topological quantum number and this is the reason why the QSH insulators are referred as topological insulators [234, 253, 256, 260–262].

A strong spin-orbit coupling is a key ingredient to obtain a topological insulator but it is not a sufficent one. A criterion to identify topological insulators was proposed by Bernevig *et al.* [241]. This is based on the idea of band inversion in which the

[1]A principle of quantum mechanics states that the wave function of a spin-1/2 particle obtains a negative sign upon a full 2π rotation.

usual ordering of the conduction band and the valence band is inverted by spin-orbit coupling [236, 241]. In the most common semiconductor the valence and the conduction bands are formed from electrons in p and s orbitals, respectively. In certain heavy elements the spin-orbit coupling is strong enough to invert the bands, so that the p-orbital band is pushed over the s-orbital one. This mechanism was predicted theoretically [241] for HgTe quantum wells (sandwiched between CdTe layers) and experimentally demonstrated [233] (Fig 6.4).

The edges states provide a direct way to discern a QSH insulator from a trivial insulator from an experimental point of view. The two edge states of a 2D topological insulator act as two conducting 1D channels, each contributing one quantum of conductance, e^2/h. In contrast a trivial insulator is characterized by a vanishing conductance. This different in the conductance can be measured experimentally and it is one fingerprint to distinguish a topological insulator. In a 2D topological insulator the two 1D edge states cross at $k = 0$ in the Brillouin zone, showing a linear dispersion around this point. The linear dispersion can be described by the Dirac equation for a massless relativistic fermion in 1D and hence it can be used to describe the QSH edge state. The same concept can be generalized to 3D topological insulators, where the surface state consists of a single 2D massless Dirac fermion and the dispersion forms what is known as a Dirac cone, as shown in (Fig. 6.5).

The crossing point (the tip of the cone) is located at a TR-invariant point of the Brillouin zone such as $k = 0$, and the degeneracy is protected by TR symmetry. The alloy $Bi_{1-x}Sb_x$ was first predicted [236] and then experimentally proven with angle-resolved photoemission spectroscopy [242] to be a 3D topological insulator in a special range of x. The layered compounds Bi_2Se_3, Bi_2Te_3 and Sb_2Te_3 were also predicted [245] to be 3D topological insulators and they have been defined as the second generation of TIs [247]. The non trivial topology in this family of materials is due to band inversion between two orbitals with opposite parity, driven by the strong

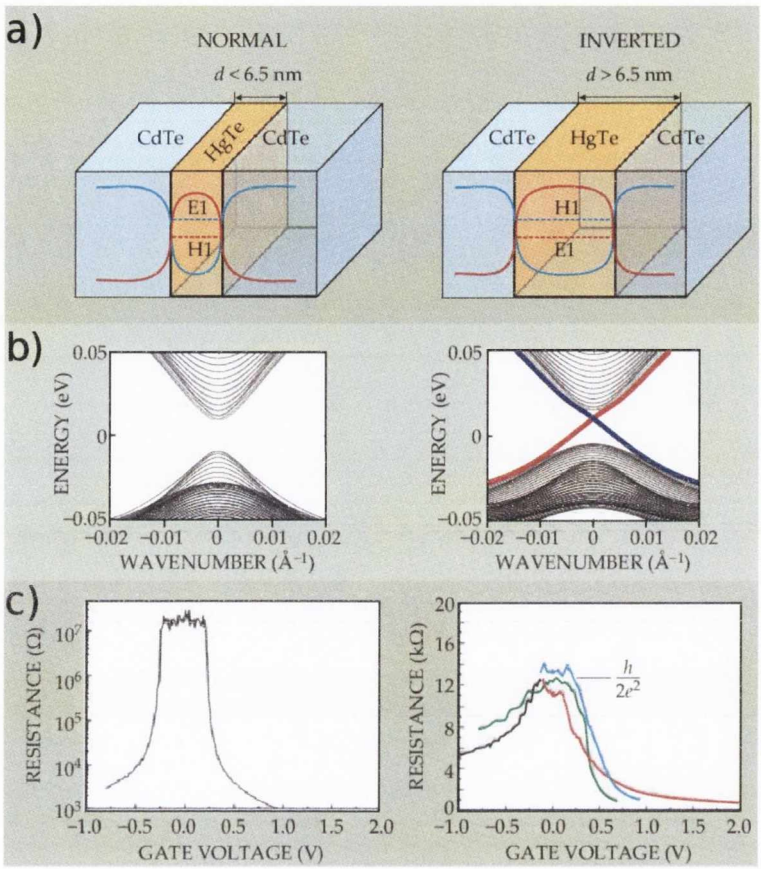

Figure 6.4: HgTe 2D quantum wells are topological insulators. At a critical value of the thickness $d_c = 6.5nm$ there is a band inversion. If the thickness d of the quantum well is lower than d_c then the energy of the lowest energy conduction band (E1) is higher than the one of the highest energy valence band (H1). The situation is inverted for $d > d_c$. The band structure of the HgTe quantum well in the two cases are shown in (b). The thin quantum well has an insulating band gap, while the thick one has conducting edge states (blue and red lines). Experimental measurements of the resistance, shown in (c), are able to discriminate the two cases. The thin quantum well has nearly infinite resistance in the band gap while the thick one exhibit a quantized resistance plateau at $R = h/2e^2$. This plateau is unchanged for different widths [blue and red lines in Fig. (c)] [256]. Image from Ref. [256].

spin-orbit coupling of Bi and Te. First principle calculations show that a surface state forms a single Dirac cone and that the spin of such state is always perpendicular to the momentum, as shown in Fig. 6.5 [245]. These results were confirmed by angle-resolved photoemission spectroscopy (ARPES) experiments [256]. The single Dirac cone surface state with linear dispersion around the Γ point ($k = 0$) has been observed in Bi_2Se_3 and Bi_2Te_3. In addition, spin-resolved measurements showed that

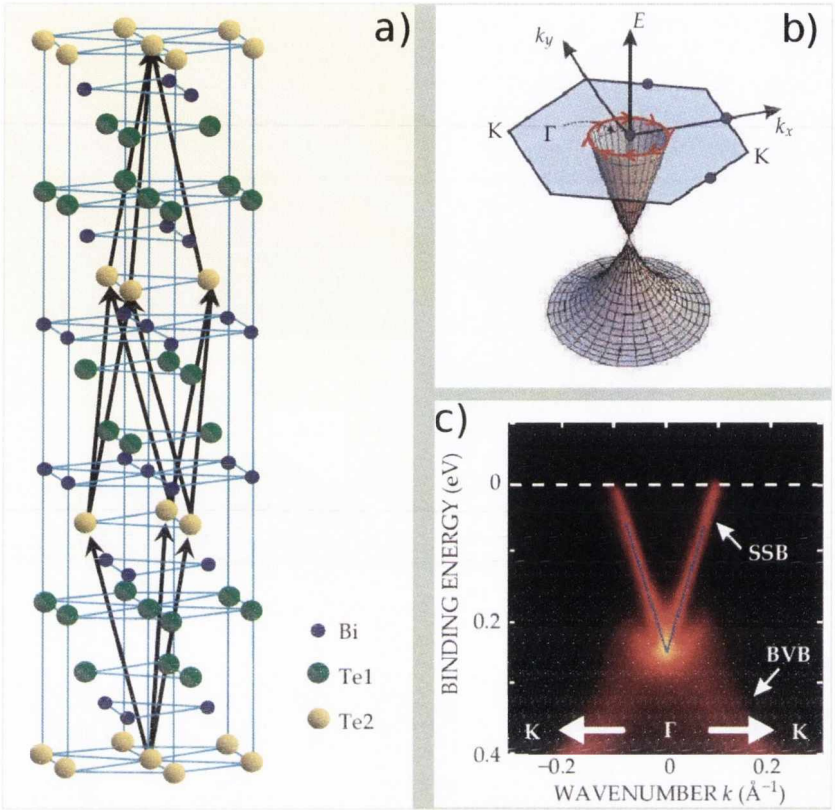

Figure 6.5: The second generation family of topological insulators has a layered structure like the one of Bi_2Te_3, shown in Fig. (a). The linearly dispersing edge states of Fig. 6.4b become surface states described by a Dirac cone. Spin-dependent ARPES measurements reveals that the spins [red arrows in Fig. (b)] of the surface states lie in the surface plane and they are perpendicular to the momentum [244, 252]. Moreover, the linear dispersion around the Γ point experimentally revealed,as shown in Fig. (c) [246, 256].

the electron spin lies in the plane of the surface and it is always perpendicular to the momentum [244, 246, 252]. It was also shown that the single Dirac cone is impossible to be constructed in a pure 2D system (like graphene or 2D HgTe quantum wells) and it is always related to novel topological properties [237–239, 254, 255].

6.3 Topological classification of insulators

Topological materials in general, and topological insulators in particular, can be defined by physically measurable topological invariants in topological field theories. Kane and Mele first introduced the topological band theory of TR-invariant QSH

insulators in 2D and they showed that they fall into two distinct topological classes, referred to as the Z_2 classification [234,253]. The theory also was extended to the 3D TIs [237–239] but its main limit lies in the fact that it is formulated in terms of non interacting electrons filling a certain number of bands of an approximate insulator model. The topological field theory was developed to extend the classification to the most general class of insulators, the interacting (real) insulators, and to introduce some quantity experimentally measurable [254,255]. Inside an insulator, the electric field $\mathbf{E}$ and the magnetic field $\mathbf{B}$ are well defined quantities. In the Lagrangian-based field theory, the electromagnetic response of an insulator can be described by an effective action

$$S_0 = \frac{1}{8\pi} \int d^3x\, dt \left(\epsilon\, \mathbf{E}^2 - \frac{1}{\mu}\, \mathbf{B}^2 \right), \tag{6.1}$$

where ϵ is the electric permittivity and μ is the magnetic permeability, from which Maxwell's equations can be derived. The integrand depends on the geometry, so it is not topological. The action S_0 can be recast in term of the 4D electromagnetic field tensor $F_{\mu\nu}$

$$S_0 = \frac{1}{16\pi} \int d^3x\, dt F_{\mu\nu}\, F^{\mu\nu}. \tag{6.2}$$

The implied summation over μ and ν depends on the metric tensor, i. e. the geometry. There is, however, another possible term in the action of the electromagnetic field

$$S_\theta = \frac{\theta\alpha}{4\pi^2} \int d^3x\, dt \mathbf{E}\cdot\mathbf{B} \equiv \frac{\theta\alpha}{32\pi^2} \int d^3x\, dt \epsilon_{\mu\nu\rho\tau} F^{\mu\nu} F^{\rho\tau} = \frac{\theta}{2\pi} \frac{\alpha}{4\pi} \int d^3x\, dt \partial^\mu \epsilon_{\mu\nu\rho\tau} A^\nu \partial^\rho A^\tau, \tag{6.3}$$

where $\alpha = e^2/\hbar c \approx 1/137$ is the fine-structure constant, θ is a parameter, and $\epsilon_{\mu\nu\rho\tau}$ is the fully asymmetric 4D Levi-Civita tensor. Unlike the Maxwell action, S_θ is a topological term, i.e. it does not depend on the geometry (independent of the metric) [245]. Since $\mathbf{E}$ is invariant under TR whereas $\mathbf{B}$ changes sign, S_θ breaks TR symmetry. By considering a periodic system, there are two values of

θ, namely 0 and π, that preserve the TR symmetry [254, 255]. By integrating all the microscopic fermionic degrees of freedom, the effective action S_θ is obtained. It allows us to classify all the nonmagnetic insulators into two distinct topological classes, described by effective topological field theories with $\theta = 0$ or $\theta = \pi$. The θ parameter is physically measurable and the two possible values, 0 and π, define the topologically trivial and nontrivial nature of the insulators, respectively (in analogy to the Z_2 classification). The coefficient $\theta = \pi$ translates into a Hall conductance of $1/2e^2/h$, half the conductance of the first QH plateau. That value is uniquely associated with the single Dirac cone on the surface of topological insulators. The Hall conductance of the system can change, due to random disorder, only by an integer multiple of the quantum of conductance e^2/h. This means that the half-QH conductance $(1/2)(e^2/h)$ can never be reduced to zero by disorder, leading to topologically robust surface states.

6.4 Preliminary results: Bi_2Se_3 on graphene

6.4.1 Bi_2Se_3

The topological insulator Bi_2Se_3 [244, 245, 252] has a rhombohedral crystal structure with the space group D^5_{3d} ($R\bar{3}m$) with five atoms in one unit cell. The material consists of five-atoms layers arranged along the z-direction, known as quintuple layers (QLs). Each quintuple layer consists of five atoms per cell with two equivalent Se atoms [Se1 and Se1' in Fig. 6.6(c)], two equivalent Bi atoms [Bi and Bi' in Fig. 6.6(c)] and a third Se atom [Se2 in Fig. 6.6(c)]. The atomic layers interact strongly within a QL while the interaction between QLs is much weaker, predominantly of the van der Waals type.

The GGA calculated band structure of a slab of Bi_2Se_3 with a variable number of QLs (one to five) is shown in Fig. 6.7(a) [263]. The band gap is suppressed for 3QLs

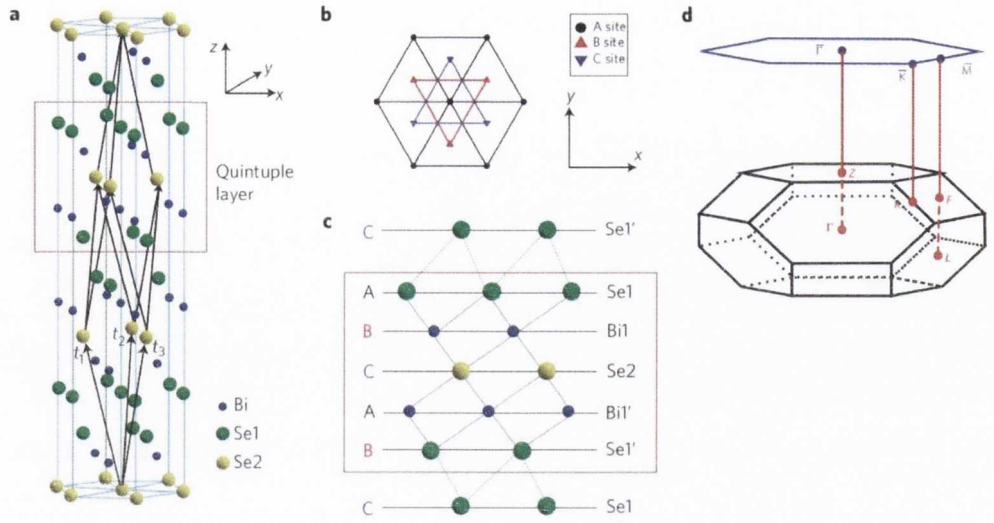

Figure 6.6: (a) Crystal structure of the layered compound Bi_2Se_3 with three primitive lattice vectors denoted as $\mathbf{t}_{1,2,3}$. A quintuple layer is indicated by a red square. (b) Top view along the z direction. (c) Side view of the quintuple layer (QL) structure. (d) Brillouin zone for Bi_2Se_3. The blue hexagon shows the 2D Brillouin zone of the projected [1 1 1] surface in which the high-symmetry $\mathbf{k}$-points are labelled [245].

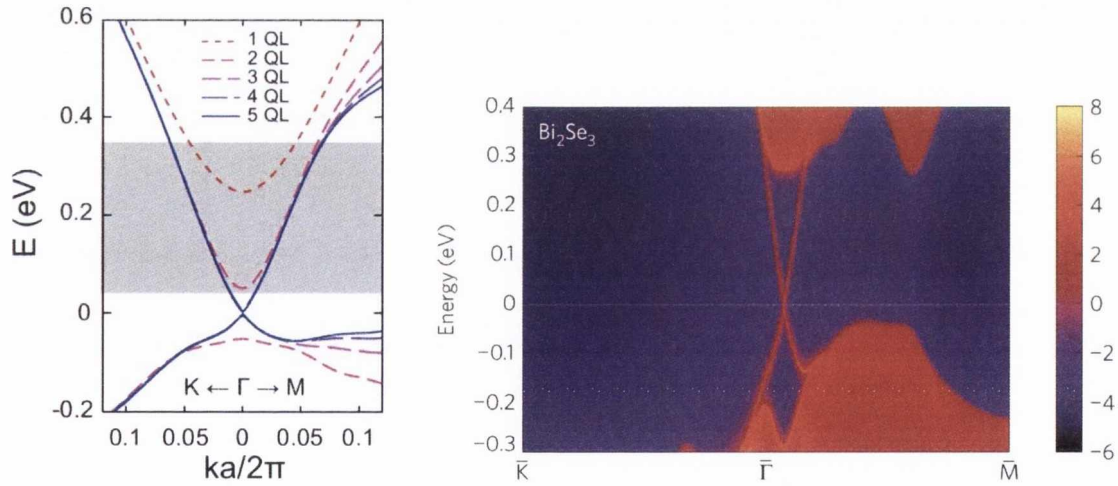

(a) (b)

Figure 6.7: (a) Band structure of a slab of Bi_2Se_3 as a function of the number of QLs. It can be noticed that for three QLs the band gap is suppressed and the Dirac cone is visible at the Γ point. The plot is rescaled in energy to the position of the Dirac cone [263]. (b) Energy and momentum dependence of the LDOS for Bi_2Se_3 on the [111] surface, obtained with ARPES measurements [245].

and beyond and the Dirac cone, originating from the topologically protected surface states, is visible at the Γ point. The zero of the energy is not referred to the Fermi

level, but it has been aligned to the position of the Dirac cone [263]. By comparison, the experimental bands dispersion obtained with angle resolved photoemission spectroscopy (ARPES) is shown in Fig. 6.7(b) [245].

6.4.2 Graphene

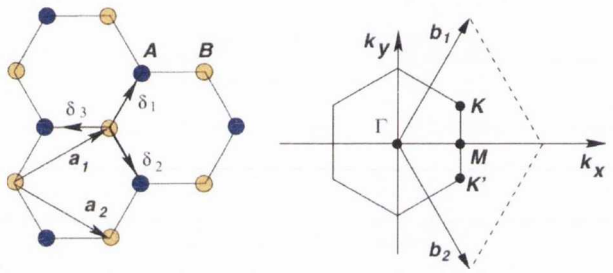

Figure 6.8: The honeycomb lattice of graphene is shown on the left-hand side with the corresponding Brilloiun zone (right-hand side). The Dirac cones are located the K and K' points of the Brillouin zone [264].

Graphene, a flat monolayer of sp^2-bonded carbon atoms arranged on a hexagonal lattice, is a very promising material for the next generation of nanoelectronics. Theoretically predicted around sixty years ago [265–268], graphene was discovered in 2004 with the experiments performed by Geim and Novoselov who were awarded the 2010 Nobel Prize in Physics [14, 269]. The popularity of graphene rapidly increased after several experiments confirmed that its charge carriers indeed behave as massless Dirac fermions [270, 271]. The structural flexibility of graphene is reflected in its electronic properties. The sp^2 hybridization between one s orbital and two p orbitals leads to a trigonal planar structure (honeycomb lattice) with a formation of a bond between carbon atoms separated by 1.42 Å (see Fig.6.8). Such a band (known as σ band) is responsible for the robustness of the lattice structure in all allotropes (fullerenes, nanotubes, graphite). Due to the Pauli principle, these bands have a filled shell and, hence, they are deep in the valence band. The remaining p orbital, which is perpendicular to the planar structure, can bind with neighboring carbon atoms, leading to the formation of an additional band. Since each p orbital

has one extra electron, the band is half filled. The electronic properties of graphene

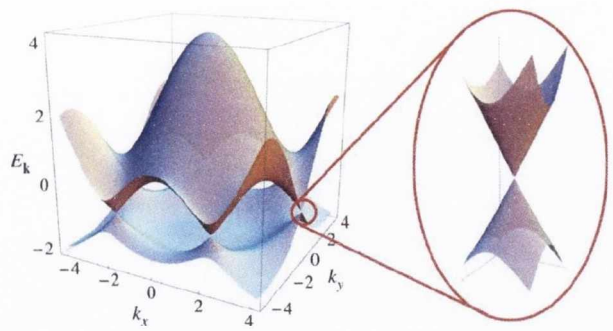

Figure 6.9: 3D representation of the electronic structure of graphene with the 6 Dirac cones. Only two of them are non-equivalent [264].

differ from most conventional three-dimensional materials. Intrinsic graphene is a semi-metal or zero-gap semiconductor with a linear dispersion relation near the six corners of the two-dimensional hexagonal Brillouin zone (see Fig. 6.9), leading to zero effective mass for electrons and holes. Due to this linear dispersion relation at low energies, electrons and holes near these six points, two of which are non-equivalent, behave like relativistic particles described by the Dirac equation for spin 1/2 particles (although the group velocity is significantly smaller than the speed of light) [272, 273]. Hence, the electrons and holes are called Dirac fermions, and the six corners of the Brillouin zone are called the Dirac points.

Graphene exhibits a remarkably high electron mobility of 15,000 $cm^2V^{-1}s^{-1}$ at room temperature, confirmed by transport measurements [274]. In addition, the symmetry of the experimentally measured conductance indicates that the mobility for holes and electrons should be nearly the same. It is almost independent of temperatures between 10 K and 100 K [270,275,276], which implies that the dominant scattering mechanism is defect scattering. Scattering by the acoustic phonons of graphene places intrinsic limits on the room temperature mobility to 200,000 $cm^2V^{-1}s^{-1}$ at a carrier density of 10^{12} cm^{-2} [276, 277]. The corresponding resistivity of the graphene sheet would be 10^{-6} Ωcm. This is less than the resistivity of silver, the lowest resistivity substance known at room temperature [276].

However, several experiments show that these properties can very significantly due to the presence of defects and impurities and to the interaction with the substrate [278–285]. When graphene is deposited on SiO_2 substrates, for instance, the scattering of electrons by optical phonons originating from the substrate is a larger effect at room temperature than scattering by graphenes own phonons. This limits the mobility to 40000 $cm^2V^{-1}s^{-1}$ [276]. Due to its very flexible nature, graphene layers tend to exhibit ripples after deposition on substrates, which affect the electronic properties [286, 287].

The high sensitivity to impurities and disorder is an intrinsic limit of graphene, due to its pure two-dimensional nature. Hence, the criterion of reproducibility of material properties in electronic devices can not be easily met when considering graphene as a material for electronic devices. This limits the applicability of such promising material and is the main reason that lead us to model an interface between graphene and the topological insulator Bi_2Se_3. Topological insulators have TR protected surface states and our aim is to model a heterostructure showing how the topological nature of this states is transferred to the interface states of graphene.

6.4.3 Graphene-Bi_2Se_3 heterostructure

The model structure investigated consists of 3QLs thin film of Bi_2Se_3 epitaxially grown on a graphene monolayer, as shown in Fig. 6.10. The unit cell of Bi_2Se_3, in its hexagonal setting, is commensurate with 3 unit cells of graphene in such a way that the elementary unit cell of the composite structure contains a full graphene carbon ring (see Fig. 6.10). The tensile stress on the Bi_2Se_3 corresponds to a lattice mismach of about 2.3%. The choice of 3QLs is justified by the fact that this is the minimal thickness for which the Bi_2Se_3 films shows topologically protected surface states [245, 263]. The Se atom at the interface with graphene sits in the hollow site of graphene (i.e. the center of the ring) [see Fig. 6.10(b)]. The lattice parameter along

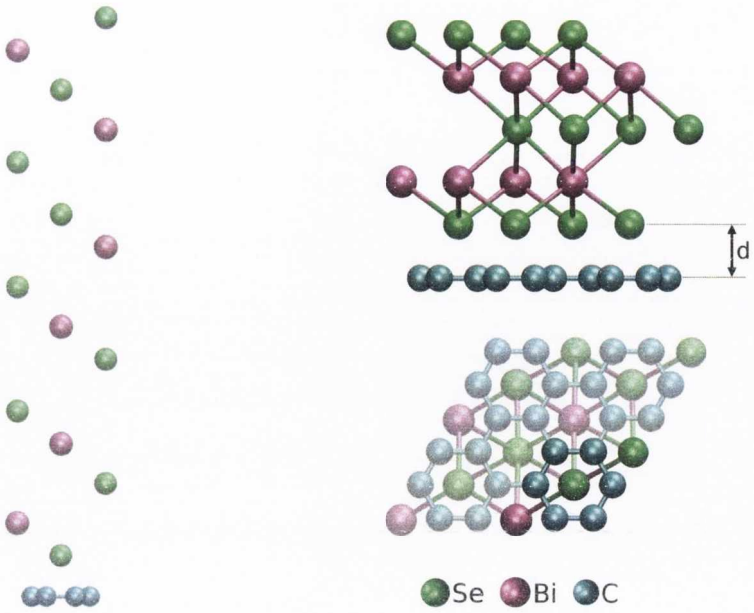

(a) (b)

Figure 6.10: Balls-and-sticks model of the graphene-Bi_2Se_3 supercell. It consists of 3 quintuple layers of Bi_2Se_3 and 6 carbon atoms (a). (b) Side (top panel) and top view (bottom panel) of a 2×2 supercell enable us to evaluate the two commensurate sublattices.

the hexagonal plane parallel to the interface is 4.26 Å, which is by only 2.3% larger than the lattice parameter of bulk Bi_2Se_3 [288]. The lattice parameter perpendicular to the interface amounts to 40 Å, where more than 10 Å simulate the vacuum region between the unit cell and its periodic images.

Similar epitaxial heterostructures have been obtained experimentally by molecular beam epitaxy techniques [289, 290].

The calculations were performed with the VASP code. The cutoff radius for the plane-waves expansion of the basis set is fixed to 400 eV. This value was determined by testing the convergence of the total energy with respect to the cutoff radius to be lower than 10 meV. A further increase in the cutoff radius does not improve significantly the precision of the calculations. The same method was used to estimate the optimal k-mesh. A $11 \times 11 \times 1$ k-point mesh was used to span the Brillouin zone. It provides the required accuracy in the total energy and it enables us to calculate the

DOS with the tetrahedron method [217], one of the most accurate schemes available. The positions of the atoms were kept at the values given from experiments and no relaxation of the atomic coordinates was performed. The reason for this relies on the fact that QLs interact between each other (and with the graphene layer) through Van Der Waals forces, which are due to charge fluctuations that can be described as non-local correlation effects. The exchange-correlation potential used in DFT is local (LDA) or semi-local (GGA) and not capable of capturing this effect. We overtook this limitation by calculating the evolution of the band structure for a wide range of separation between the TI and the graphene layer going from 2.0 Å to 3.2 Å.

The spin-orbit interaction is a relativistic effect whose magnitude increases with the atomic number. Consequently it provides negligible contributions to the electronic structure of individual atoms and bulk materials made of light elements while it has a significant impact on the physics of heavier elements such as Bi. The spin-orbit interaction is, indeed, one of the key ingredient to correctly describe the physics of TIs because it is responsible of generating the local magnetic field that originates the band inversion. The spin-orbit coupling effect was included in our calculations as implemented in the VASP code by Kresse and Lebacq[2]. Following the work of Kleinman *et al.* [291] and MacDonald *et al.* [292], the relativistic Hamiltonian is given in a basis of total angular-momentum eigenstates $|j, m_j\rangle$ with $j = l \pm \frac{1}{2}$ is recast in the form of 2×2 matrices in spin space by re-expressing the eigenstates of the total angular-momentum in terms of a tensor product of regular angular-momentum eigenstates $|l, m\rangle$ and the eigenstates of the z component of the Pauli-spin matrices. The relativistic effective potential consists of a term which is diagonal in spin space and contains the mass velocity and the Darwin corrections, and the spin-orbit operator

$$\mathbf{V} = \mathbf{V}^{SC} + \mathbf{V}^{SO} = \sum_{l,m} \left[V_l \cdot 1_\sigma + V_l^{SO} \mathbf{L} \cdot \mathbf{S} \right] |l, m\rangle\langle l, m|, \tag{6.4}$$

[2]VASP manual: http://cms.mpi.univie.ac.at/vasp/vasp/vasp.html

where 1_σ is the unit operator in spin space and

$$\mathbf{L}\cdot\mathbf{S} = \frac{1}{2}\begin{pmatrix} L_z & L_- \\ L_+ & -L_z \end{pmatrix}. \tag{6.5}$$

The l components of the scalar V_l and spin-orbit V_l^{SO} potentials are weighted averages over the $l \pm \frac{1}{2}$ components. The Hamiltonian is therefore a 2×2 matrix in spin space. The nondiagonal elements arise from the spin-orbit coupling but also from the exchange-correlation potential when the system under consideration exhibits a noncollinear magnetization [293]. Calculations including spin-orbit coupling were, hence, performed in the noncollinear mode implemented in VASP by Hobbs *et al.* [294] and Marsman *et al.* [295].

Our calculated evolution of electronic gap of graphene as a function of the graphene-Bi_2Se_3 distance is presented in Fig. 6.11(a) [296]. In order to determine the bands belonging to graphene, the local density of states (LDOS), projected onto spherical harmonics centered over the atoms, have been evaluated for a given energy band and momentum parallel to the interface. The graphene band gap can be extrapolated as an energy difference between the top of the highest occupied (or partially occupied) and the bottom of the lowest unoccupied graphene bands. Four distinct regions can be observed in Fig. 6.11(a).

For a graphene-Bi_2Se_3 separation larger than $d = 3.2$ Å, graphene has a zero gap [region D in Fig. 6.11(a)]. This is expected since at such a large distance the graphene states do not overlap with the surface states of Bi_2Se_3 and both systems act independently, i.e. there is no interaction between the two materials (graphene is a zero-gap semiconductor [270,271]). Due to the particular supercell setting used for the calculations, the high symmetry points (K and K') of the graphene's Brillouin zone (BZ) are folded onto the Γ point of the Bi_2Se_3 BZ [see Fig. 6.11(b)]. As a result, the two distinct cones of the bare graphene band structure give rise to 4 degenerate

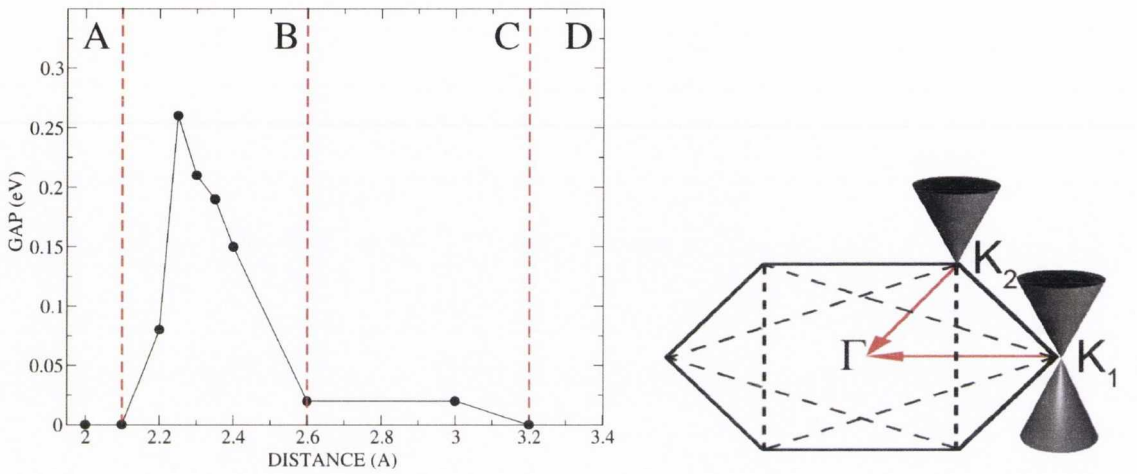

(a) (b)

Figure 6.11: (a) Evolution of the band gap of graphene as a function of the distance d with respect to Bi_2Se_3. Four main regions can be identified: A: $d \leq 2.1$ Å; B: 2.1 Å$< d <$ 2.6 Å; C: 2.6 Å$< d <$ 3.2 Å and D: $d \geq 3.2$ Å. (b) Folding of the graphene Brillouin zone within the supercell setting used in the calculations. The two inequivalent cones at K_1 and K_2 are folded to the Γ point in the BZ of the composite system [296].

cones (2 cones plus 2 spin degeneracy per cone) in the band structure of the composed system [this can be noticed in Fig. 6.12(a)]. The region C of Fig. 6.11(a), for 2.62 Å $<$ $d <$ 3.2 Å, is characterized by a very small gap in the graphene band structure. By comparing the band structure for $d = 3.0$ Å and $d = 2.6$ Å, [compare Fig. 6.12(a) with Fig. 6.12(b)] it can be noticed that the degeneracy of the upper part of the graphene's 4-folded cones is removed. Two bands belonging to the original cone are located at around 0.11 eV above E_F while the other two are shifted up by 0.2 eV. The reason for this splitting might be due to the symmetry of the electrostatic potential of Bi_2Se_3 but its nature is still under investigation. By reducing the distance d [see region B in Fig. 6.11(a)], a gap opens in graphene, which monotonically increases till its maximum value of 0.26 eV, corresponding to a separation $d = 2.3$ Å. Then it disappears again for $d = 2.1$ Å. While the upper cone of graphene is further pushed up toward higher energies, the lower cone remains pinned around the Fermi level E_F.

The two topologically protected states of Bi_2Se_3 (one for each surface) are located

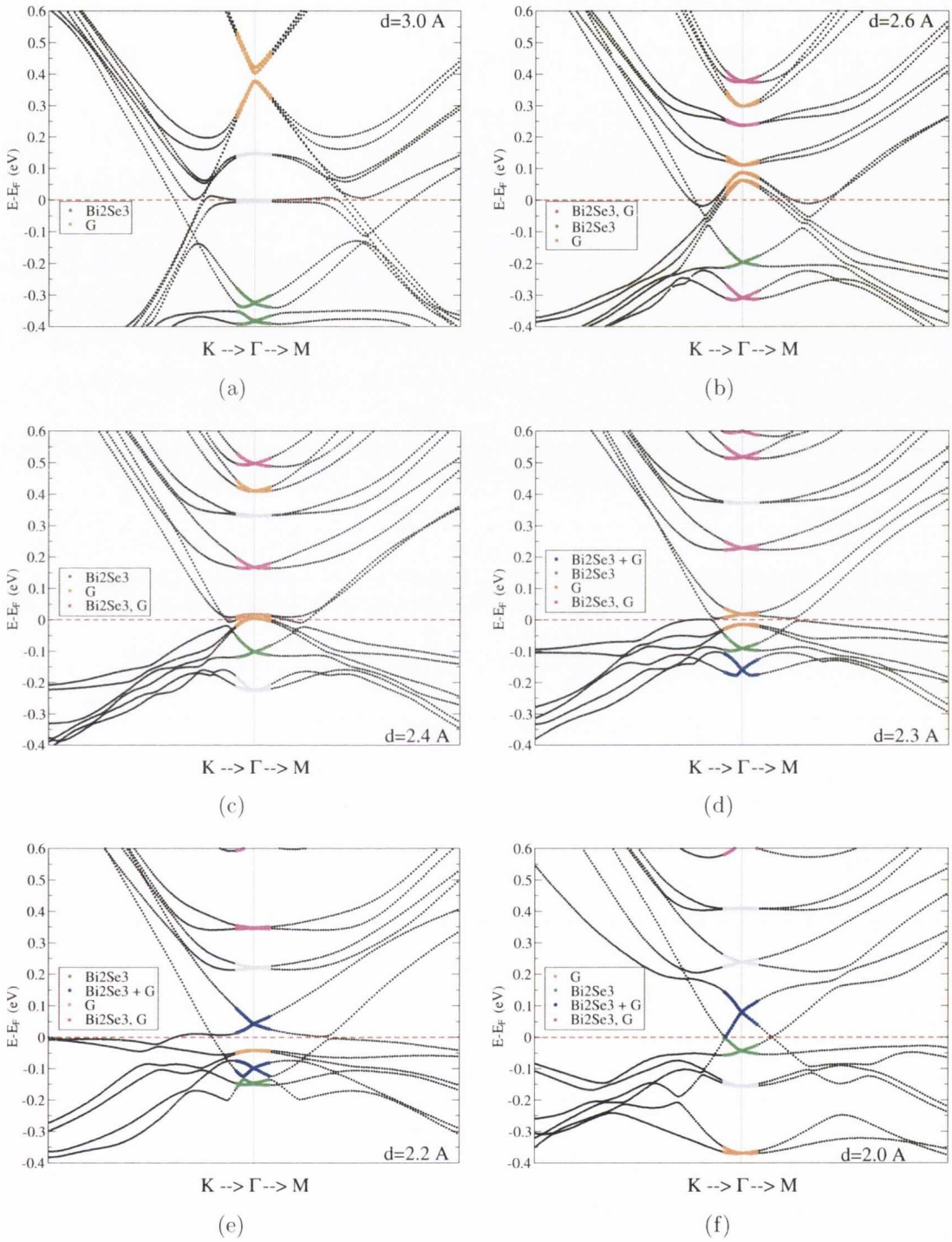

Figure 6.12: Evolution of the band structure of graphene as a function of the distance d. The orange bands are mostly due to graphene. The blue bands are interface bands of the composite systems. The green bands are Bi_2Se_3 surface bands. The magenta bands have independent contributions from both systems. The grey bands are Bi_2Se_3 bands which do not belong to the surfaces.

in the proximity of the Fermi level E_F and are degenerate in the isolated system. The interaction with graphene, for distances lower than 2.4 Å breaks the inversion symmetry of these states, removing the degeneracy [see Figs. 6.12(c), 6.12(d) and 6.12(e)]. At a separation $d = 2.2$ Å, the graphene states pinned around the Fermi level start to couple with the surface state of Bi_2Se_3 causing the 4-fold cone of graphene to split. Two out of the four bands initially belonging to the cone are pushed towards lower energies [see Fig. 6.12(e)]. The mixed band originating from graphene and the surface state of Bi_2Se_3 is marked with the blue color in Fig. 6.12(e). The remaining graphene double degenerate band and the other Bi_2Se_3 surface state are colored respectively in orange and green and are located at around 0.05 eV and 0.15 eV below the Fermi level E_F. The electron density integrated in the energy range around Fermi level and projected on the mixed state is shown in Fig. 6.13(b). This state is mostly localized on the graphene atoms and the interface Se atoms. The mixed state is dominated by C-p_z and Se-p_z atomic orbitals contributions and it is delocalized at the interface between the two subsystems due to the ppπ interaction. In order to gain a more quantitative insight, we plot the charge density corresponding to Bi_2Se_3 surface state opposite to the interface [see Fig. 6.13(a)]. The plot shown Fig. 6.13(c) is obtained by summing the contribution of the two LDOS and averaging the data in planes perpendicular to the interface. While the contribution of the bulk region to the LDOS is small, the surface states dominate on both sides of the slab. As expected, at the opposite side of the interface, the state is localized dominantly at the surface Se layer. A striking feature of the interface region is the migration of the surface LDOS of Bi_2Se_3 from the Se atoms to the graphene sheet. This behavior resembles closely to the one reported the Sb_2Se_3-Bi_2Se_3 interface (a normal metal with a TI) [297].

The region A of Fig. 6.11(a), corresponding to $d \leq 2.1$ Å, witnesses the closing of the graphene gap which remains constant until a separation $d = 2$ Å (we did

not investigate shorter distances). The other two bands, originally belonging to the 4-fold degenerate cone pinned at the Fermi level, are pushed further towards lower energy. The energy window around the Fermi level features, at the Γ point, the graphene-Bi_2Se_3 interface cone, located 0.1 eV above E_F and the remaining Bi_2Se_3 surface cone at 0.15 eV below E_F.

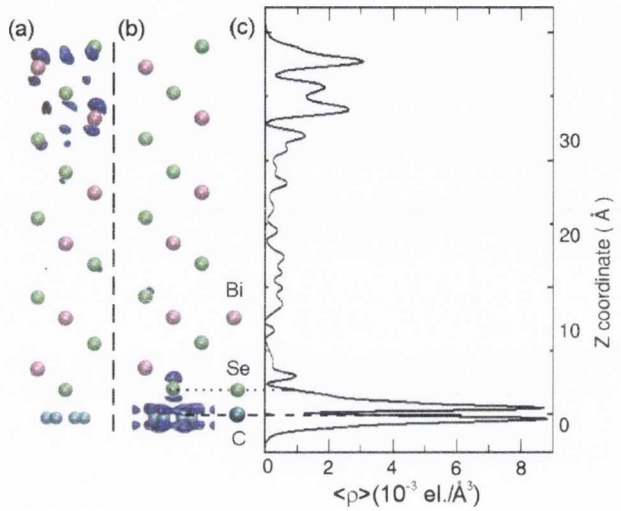

Figure 6.13: LDOS for the graphene-Bi_2Se_3 mixed state (b) and the Bi_2Se_3 surface states on the opposite side (a), calculated at the Γ point for $d = 2.2$ Å. (c) The graphs shows the sum of the LDOS in (a) and (b) avaraged on a plane parallel to the interface. z=0 corresponds to the position of the C atoms.

A fundamental property of 3D TIs is the existence of an odd number of surface bands around Fermi level. Bi_2Se_3, for instance, has one conical band that crosses the Fermi level. In addition, the topology of the surface states is such that the states connect bulk valence and conduction bands. As a topological property cannot be changed by smooth transformation of the material's geometry, such states must cross the Fermi level, i.e. the states remain metallic even in presence of defects (or non-magnetic impurities) [17]. The graphene-Bi_2Se_3 heterostructure exhibits one conical band at the Fermi level for a separation $d = 2.0$ Å at which the C-Se bond length is close to the sum of their covalent radii. Although a full structural optimization of the interface was not performed (mostly because it requires an accurate description of the van der Waals interaction), the topological properties are not expected to

depend on the geometry details. The single conical band has a significant contribution from graphene, whereas the contribution of the interfacing Se surface becomes proportionally smaller [296]. A similar situation was found for the Sb_2Se_3-Bi_2Se_3 interface, where the topological protected state is transferred to the normal metal Sb_2Se_3 [297]. Moreover, the graphene band at Fermi level exhibits a helical spin texture (a preliminary result, not shown here), which is a requirement for topologically protected surface states in TIs. The verification of the topological protection of graphene band by means of the parity of wave function is not possible in the case of graphene-Bi_2Se_3 heterostructure due to the lack of inversion symmetry. Hence, a direct calculation of the Chern numbers is necessary and it is under investigation.

6.5 Conclusions

The preliminary results concerning the electronic properties of a graphene-Bi_2Se_3 heterostructure were presented in this chapter. For different graphene-TI separations, four phases were identified. In the first phase ($d \geq 3.2$ Å), the electronic structures of graphene and Bi_2Se_3 remain identical to those of the corresponding isolated systems. In the second phase ($2.6\text{Å} \leq d < 3.0\text{Å}$), the upper part of the 4-fold degenerate graphene cone splits into two. Two of the bands participating in the original cone are pushed towards higher energies, while the remaing two remain located around the Fermi level. The third phase ($2.1\text{Å} < d < 2.6\text{Å}$) is characterized by the formation of a chemical bond between the two subsystems. The degeneracy is removed from the lower 4-folded cone originating from graphene and from the double degenerate surface state of Bi_2Se_3. A new conical band (at the Γ point) originates from the mixing of graphene and Bi_2Se_3 bands. The fourth phase ($d \leq 2.1$ Å) clearly indicates a conical band in the proximity of the Fermi level which is spatially located at the graphene-Bi_2Se_3 interface and originates from the mixed system. The topological nature of such a band is still under investigation.

CHAPTER 7

Conclusions

In this thesis we studied the electronic and structural properties of a single H atom adsorbed on a bare Si(100) surface with $c(4 \times 2)$ reconstruction. The H atom passivates one of the Si dangling bonds, breaks the Si-Si π-bond and leaves an isolated dangling bond, named the single dangling bond (SDB), on the other site of the dimer. We were able to characterize the geometry and the charging state of the SDB for different doping conditions by means of DFT calculations together with STM/STS experiments. For n-doped systems the H-produced SDB is doubly occupied with the H_B configuration being the lowest in energy. This configuration coincides with the majority species found in low temperature STM experiments. The H_T configuration is the lowest in energy for p-doped samples, with the SDB state being empty. Finally, according to our calculations, the H_B configuration is predicted to be the lowest in energy for the neutral intrinsic case and the SDB state is partially occupied and spin-polarized. The buckling angle of the reacted dimer and, correspondingly, the bonding character of the Si atoms at SDB site reflect the occupation of the SDB

state: sp^3-like and sp^2-like orbital symmetries are found when the SDB is, respectively, doubly occupied and empty. A hybrid configuration in between the two is found for a partial occupation (one electron in the SDB state).

Beside the "classical" local approach, we made use of a nonlocal approach which enabled us to characterize the different configurations of the system in their unperturbed state. This approach combines the calculated nonlocal DOS with STS measurements to extract information about the phase-shift $\Theta(k)$. The phase-shift mapping proved to be a very precise fingerprint for discerning between different H adsorption configurations and it has the potential of becoming a very general tool to determine the configuration of molecules and adspecies deposited on surfaces. Furthermore, it can be very useful where the topographic signatures of different configurations are indistinguishable or, for instance, where there are no STM-accessible states within the tunneling energy window. As the nonlocal approach barely perturbs the scattering center, it can be used to characterize adsorbate geometries that are mechanically unstable under the STM tip.

The configuration and charging state of the SDB are responsible for a gating between the reacted row and a bare adjacent one. The magnitude of the gating is proportional to the charging of the SDB and to the directionality of the SDB orbital. The extra negative charge and the directionality of the p orbital of the SDB result in a pronounced gating effect on the adjacent row in the case of the n-doped H_B configuration. This effect is less pronounced in the n-doped H_T case, where the SDB is singly occupied and the orbital has a s symmetry. Finally the gating effect is almost absent in the p-doped H_T case, due to the lack of negative charge at the SDB site.

All the results presented in this thesis can provide an interesting perspective for exploring fundamental properties of coupled systems (e.g. quantum wells) as well as applicative aspects aimed at the fabrication of nano-devices. The gating effect,

together with the ability of creating quantum wells by nanopattering the Si(100) with an STM tip, may offer the opportunity to study coupled real quantum wells. Two hydrogen atoms, for instance, may be deposited on one dimer row of the Si(100)-$c(4\times2)$ surface to create a quantum well, while a third H is deposited on an adjacent row. This latter H will induce a gating (depending on the adsorption configuration) on the row containing the quantum well, causing it to split into two coupled wells. Such a system is currently under investigation.

The interplay between charging and geometry can be taken as the basic mechanism for fabricating an atomic-scale switch device. In fact, by tuning the surface doping from p-type to n-type, one may switch between the two H configurations. These have distinct scattering and transport properties [226], so that the switch can be detected electrically or by mapping the phase-shift using the nonlocal approach method. The surface doping can be tuned by a local gating of the SDB, for example using the STM tip as a gating electrode. Another possibility is to create a depletion region in the surroundings of the SDB by applying an electric field through an electrode positioned at the bottom of the slab. It would work in the same fashion as the gate electrode of a FET transistor.

Due to the gating dependence on charging and geometry of the SDB, a two rows device can also be modeled on the Si(100)-$c(4\times2)$ reconstructed surface. The flipping between the two configurations is operated at the reacted row (the one containing the adsorbed H) and the signal discriminating the two states (phase-shift, for example) is detected at the bare adjacent row.

The modelling and the experimental implementation of the aforementioned flipping mechanism into a switch device will be part of our future plans. We performed some preliminary calculations on phosphorous-doped systems. The position-dependent features related to the presence of the dopant and confirmed by STM experiments will be the object of further investigations.

The preliminary results concerning the electronic properties of a graphene-Bi_2Se_3 heterostructure were presented. For different graphene-TI separations, four phases were identified. In the first phase ($d \geq 3.2$ Å), the electronic structures of graphene and Bi_2Se_3 remain the one of the isolated systems. In the second phase ($2.6\text{Å} \leq d < 3.0\text{Å}$), the upper part of the 4-fold degenerate graphene cone splits in two. Two of the bands participating in the original cone are pushed towards higher energies, while the remaining two are still located around the Fermi level. The third phase ($2.1\text{Å} < d < 2.6\text{Å}$) is characterized by the chemical bonding between the two subsystems. The degeneracy is removed from the lower 4-fold cone originating from graphene and from the double degenerate surface state of Bi_2Se_3. A new conical band (at the Γ point) originates from the mixing of graphene and Bi_2Se_3 bands. The fourth phase ($d \leq 2.1$ Å) clearly indicates a conical band in the proximity of the Fermi level which is spatially located at the graphene-Bi_2Se_3 interface and originates from the mixed system. Some preliminary results (not shown in this thesis) indicate a helical spin texture characterizing the Fermi surface of the interface conical band in the proximity of the Γ point of the Brillouin zone. This is one of the peculiar properties necessary for topological insulators but it requires further investigations.

A topological protected state in graphene, once supported by experimental verification, would promote this versatile material as a very promising replacement for silicon aimed at nanoelectronics applications.

APPENDIX A

Schrödinger equation for a potential step

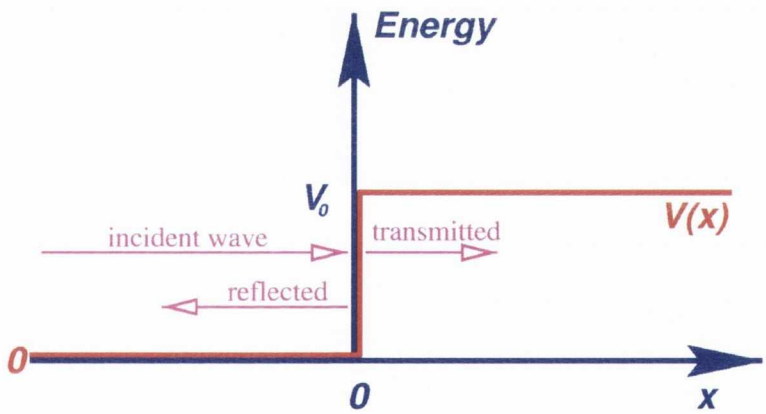

Figure A.1: Schematic representation of a potential step $V(x)$ at the position $x = 0$.

The solution of the Schrödinger equation for a potential step has been used as a model to map the standing wave pattern present in the LDOS and originating from the potential barrier created by the reacted dimer. In this simple model the potential step is supposed to be finite and positive so that $V = V_0(x)$ with $V_0 > 0$ for $x \geq 0$ and $V_0 = 0$ elsewhere, as shown in fig. A.1. The potential creates a barrier to the wave function and an incident wave coming from the left ($x < 0$) can

be partially (or totally) reflected from the barrier. If the energy of the wave ε is less than V_0, then it cannot propagate in the positive region ($x > 0$) and the wave-vector $k = \sqrt{2m[\varepsilon - V_0(x)]/\hbar^2}$ is imaginary. In the negative half-space the wave function can be considered under the general form

$$\psi_1(x) = Ae^{ikx} + Be^{-ikx}. \tag{A.1}$$

It is composed by an incident and a reflected wave (positive and negative exponent term, respectively), where the wave vector is now given by

$$k = \sqrt{\frac{2m\varepsilon}{\hbar^2}}. \tag{A.2}$$

In the positive half-space, the solution of the Schrödinger equation is

$$\psi_2(x) = Ce^{-i\gamma x} \qquad \text{where} \qquad \gamma = \sqrt{\frac{2m[V_0 - \varepsilon]}{\hbar^2}}. \tag{A.3}$$

The two wave function have to be smoothly joined at $x = 0$. The constants A, B and C can be determined by the normalization of the wave function and by applying the boundary conditions. The normalization condition can be considered by setting $A = 1$ without losing generality. The boundary conditions are applied by imposing the continuity of the wave function and its derivative at the interface ($x = 0$):

$$\begin{cases} \psi_1(0) = \psi_2(0) & \Rightarrow \quad A + B = C \\ \left.\dfrac{d\psi_1}{dx}\right|_{x=0} = \left.\dfrac{d\psi_2}{dx}\right|_{x=0} & \Rightarrow \quad ik(A - B) = -\gamma C, \end{cases} \tag{A.4}$$

from which it follows

$$\begin{cases} \frac{C}{A} = \frac{2ik}{ik-\gamma} \\ \frac{B}{A} = \frac{ik+\gamma}{ik-\gamma}. \end{cases} \tag{A.5}$$

The amplitude of the reflected wave is unity as there is no probability amplitude for

transmission across the interface and the only effect due to the interface is a phase shift in the reflected wave. The wave function in the negative region is given by

$$\psi_1(x) = A[e^{ikx} + e^{-ikx+\Theta}], \tag{A.6}$$

where

$$\Theta = 2\tan^{-1}\left(\frac{\gamma}{k}\right). \tag{A.7}$$

The probability amplitude is then given by

$$|\psi_1(x)|^2 = 2A^2[1 + 2cos(2kx + \Theta)] \qquad \text{for} \qquad x < 0. \tag{A.8}$$

This is a standing wave pattern with the probability oscillating from 0 to $2A^2$. The first peak occurs at $x = -\Theta/2k$ and it is dependent on the phase shift at the interface. For $V_0 \to \infty$ the damping coefficient $\gamma \to \infty$ and the phase shift approaches π. The first peak occurs for $kx = \pi/2$, which implies the wave function to become zero at $x = 0$ [52].

APPENDIX B

Publications

- *Spectroscopic characterization of a single dangling bond on a bare Si(100)-c(4 × 2) surface for n- and p-type doping.*
  M. Mantega, I. Rungger, B. Naydenov, J. J. Boland and S. Sanvito,
  Physical Review B **86**, 035318 (2012).

- *Scattered surface charge density: A tool for surface characterization.*
  B. Naydenov, **M. Mantega**, I. Rungger, S. Sanvito and J. J. Boland,
  Physical Review B **84**, 195321 (2011).

- *Gating effects on the dimer rows of Si(100)-c(4 × 2) surface.*
  B. Naydenov, **M. Mantega**, I. Rungger, S. Sanvito and J. J. Boland,
  submitted to Physical Review Letters, (2012).

- *Emergence of topological protected states at the graphene-Bi_2Se_3 interface.*
  I. Popov, **M. Mantega**, A. Narayan and S. Sanvito,
  submitted to Physical Review Letters, (2012).

- *Density functional theory based screening of ternary alkali-transition metal borohy-*

drides: A computational material design project.

J. S. Hummelshøj, D. D. Landis, J. Voss, T. Jiang, A. Tekin, N. Bork, M. Dulak, J. J. Mortensen, L. Adamska, J. Andersin, J. D. Baran, G. D. Barmparis, F. Bell, A. L. Bezanilla, J. Bjork, M. E. Björketun, F. Bleken, F. Buchter, M. Bürkle, P. D. Burton, B. B. Buus, A. Calborean, F. Calle-Vallejo, S. Casolo, B. D. Chandler, D. H. Chi, I Czekaj, S. Datta, A. Datye, A. DeLaRiva, V Despoja, S. Dobrin, M. Engelund, L. Ferrighi, P. Frondelius, Q. Fu, A. Fuentes, J. Fürst, A. García-Fuente, J. Gavnholt, R. Goeke, S. Gudmundsdottir, K. D. Hammond, H. A. Hansen, D. Hibbitts, E. Hobi, Jr., J. G. Howalt, S. L. Hruby, A. Huth, L. Isaeva, J. Jelic, I. J. T. Jensen, K. A. Kacprzak, A. Kelkkanen, D. Kelsey, D. S. Kesanakurthi, J. Kleis, P. J. Klüpfel, I Konstantinov, R. Korytar, P. Koskinen, C. Krishna, E. Kunkes, A. H. Larsen, J. M. García Lastra, H. Lin, O. Lopez-Acevedo, **M. Mantega**, J. I. Martínez, I. N. Mesa, D. J. Mowbray, J. S. G. Mýrdal, Y. Natanzon, A. Nistor, T. Olsen, H. Park, L. S. Pedroza, V Petzold, C. Plaisance, J. A. Rasmussen, H. Ren, M. Rizzi, A. S. Ronco, C. Rostgaard, S. Saadi, L. A. Salguero, E. J. G. Santos, A. L. Schoenhalz, J. Shen, M. Smedemand, O. J. Stausholm-Møller, M. Stibius, M. Strange, H. B. Su, B. Temel, A. Toftelund, V Tripkovic, M. Vanin, V Viswanathan, A. Vojvodic, S. Wang, J. Wellendorff, K. S. Thygesen, J. Rossmeisl, T. Bligaard, K. W. Jacobsen, J. K. Nørskov, T. Vegge,

Journal of Chemical Physics **131**, 014101 (2009).

List of Figures

Bibliography

[1] http://www.britannica.com/. The invention of the transistor, Encyclopaedia Britannica, 2011.

[2] G. E. Moore. Cramming more components onto integrated circuits. *Electronics*, **38**(8), 1965.

[3] Y. M. Lin, C. Dimitrakopoulos, K. A. Jenkins, D. B. Farmer, H. Y. Chiu, A. Grill, and P. Avouris. 100-GHz Transistors from Wafer-Scale Epitaxial Graphene. *Science*, **327**(5966), 2010.

[4] Y.-M. Lin, A. Valdes-Garcia amd S.-J. Han, D. B. Farmer, I. Meric, Y. Sun, Y. Wu, C. Dimitrakopoulos, A. Grill P. Avouris, and K. A. Jenkins. Wafer-Scale Graphene Integrated Circuit. *Science*, **332**(1294), 2011.

[5] L. Britnell, R. V. Gorbachev, R. Jalil, B. D. Belle, F. Schedin, A. Mishchenko, T. Georgiou, M. I. Katsnelson, L. Eaves, S. V. Morozov, N. M. R. Peres, J. Leist, A. K. Geim, K. S. Novoselov, and L. A. Ponomarenko. Field-Effect Tunneling Transistor Based on Vertical Graphene Heterostructures. *Science*, **335**(947), 2012.

[6] C. Sire, F. Ardiaca, S. Lepilliet, J.-W. T. Seo, M. C. Hersam, G. Dambrine, H. Happy, and V. Derycke. Flexible Gigahertz Transistors Derived from Solution-Based Single-Layer Graphene. *Nano Letters*, **12**(1184), 2012.

[7] F. Schwierz. Graphene transistors. *Nature Nanotechnology*, **5**(487), 2010.

[8] H. Liu and P. D. Ye. Atomic-layer-deposited Al_2O_3 on Bi_2Te_3 for topological insulator field-effect transistors. *Applied Physics Letters*, **99**(052108), 2011.

[9] D. Kong, Y. Chen, J. J. Cha, Q. Zhang, J. G. Analytis, K. Lai, Z. Liu, S. Sae Hong, K. J. Koski, S.-K. Mo, Z. Hussain, I. R. Fisher, Z.-X. Shen, and Y. Cui. Ambipolar field effect in the ternary topological insulator $(Bi_xSb_{1-x})_2Te_3$ by composition tuning. *Nature Nanotechnology*, **6**(705), 2011.

[10] T. Hasegawa and J. Takeya. Organic field-effect transistors using single crystals. *Science and Technology of Advanced Materials*, **10**(024314), 2009.

[11] Y. Yamashita. Organic semiconductors for organic field-effect transistors. *Science and Technology of Advanced Materials*, **10**(024313), 2009.

[12] G.P. Lopinski, D. D. Wayner, and R. A. Wolkow. Self-directed growth of molecular nanostructures on silicon. *Nature*, **406**(48), 2000.

[13] Y.-H. Chu, L. W. M, M. B. Holcomb, M. Gajek, S.-J. Han, Q. He, N. Balke, C.-H. Yang, D. Lee, W. Hu, Q. Zhan, P.-L. Yang, A. Fraile-Rodrguez, A. Scholl, S. X. Wang, and R. Ramesh. Electric-field control of local ferromagnetism using a magnetoelectric multiferroic. *Nature Materials*, **7**(478), 2008.

[14] K. S. Novoselov, A. K. Geim, S. V. Morozov, D. Jiang, Y. Zhang, S. V. Dubonos, I. V. Grigorieva, and A. A. Firsov. Electric Field Effect in Atomically Thin Carbon Films. *Science*, **306**(666), 2004.

[15] M. C. Lemme, T. J. Echtermeyer, M. Baus, and H. Kurz. A Graphene Field-Effect Device. *IEEE Electron Device Letters*, **28**(282), 2007.

[16] R. Sordan, F. Traversi, and V. Russo. Logic gates with a single graphene transistor. *Applied Physics Letters*, **94**(073305), 2009.

[17] M. Z. Hasan and C. L. Kane. Colloquium: Topological insulators. *Reviews of Modern Physics*, **82**(3045), 2010.

[18] S. Y. Xu, Y. Xia, L. A. Wray, S. Jia, F. Meier, J. H. Dil, J. Osterwalder, B. Slomski, A. Bansil, H. Lin, R. J. Cava, and M. Z. Hasan. Topological Phase Transition and Texture Inversion in a Tunable Topological Insulator. *Science*, **332**(560), 2011.

[19] J. T. Yates. A New Opportunity in Silicon-Based Microelectronics. *Science*, **279**(335), 1998.

[20] T. Rakshit, G.-C. Liang, A. W. Ghosh, and S. Datta. Silicon-based Molecular Electronics. *Nanoletters*, **4**(1803), 2004.

[21] B. E. Kane. A silicon-based nuclear spin quantum computer. *Nature*, **393**(133), 1998.

[22] A. Politi, J. C. F. Matthews, and J. L. O'Brien. Shors Quantum Factoring Algorithm on a Photonic Chip. *Science*, **325**(1221), 2009.

[23] J. W. Lyding, T.C. Shen, J. S. Hubacek, J. R. Tucker, and G. C. Abeln. Nanoscale patterning and oxidation of H-passivated Si(100)-2×1 surfaces with an ultrahigh vacuum scanning tunneling microscope. *Applied Physics Letters*, **64**(2010), 1994.

[24] S. R. Schofield, N. J. Curson, M. Y. Simmons, F. J. Rueß, T. Hallam, L. Oberbeck, and R. G. Clark. Atomically Precise Placement of Single Dopants in Si. *Physical Review Letters*, **91**(136104), 2003.

[25] T.C. Shen, C. Wang, G. C. Abeln, J. R. Tucker, J. W. Lyding, Ph. Avouris, and R. E. Walkup. Atomic-Scale Desorption Through Electronic and Vibrational Excitation Mechanisms. *Science*, **268**(1590), 1995.

[26] M. Baseer Haider, Jason L. Pitters, Gino A. DiLabio, Lucian Livadaru, Josh Y. Mutus, and Robert A. Wolkow. Controlled Coupling and Occupation of Silicon Atomic Quantum Dots at Room Temperature. *Physical Review Letters*, **102**(046805), 2009.

[27] M. B. Haider, J. L. Pitters, G. A. DiLabio, L. Livadaru, J. Y. Mutus, and R. A. Wolkow. Controlled Coupling and Occupation of Silicon Atomic Quantum Dots at Room Temperature. *Physical Review Letters*, **102**(046805), 2009.

[28] T. Yokoyama and K. Takayanagi. Size quantization of surface-state electrons on the Si(001) surface. *Physical Review B*, **59**(12232), 1999.

[29] K. Sagisaka and D. Fujita. Quasi-one-dimensional quantum well on Si(100) surface crafted by using scanning tunneling microscopy tip. *Applied Physics Letters*, **88**(203118), 2006.

[30] K. Sagisaka and D. Fujita. A parabolic quantum well on a single dimer row of the Si(001) surface studied by scanning tunneling spectroscopy. *Journal of Physics: Conference Series*, **100**(052002), 2008.

[31] B. Naydenov and J. J. Boland. STM spectroscopy of a 1D quantum well on the Si(100) surface. *Unpublished*, , 2009.

[32] G. P. Lansbergen, R. Rahman, C. J. Wellard, I. Woo, J. Caro, N. Collaert, S. Biesemans, G. Klimeck, L. C. L. Hollenberg, and S. Rogge. Gate-induced

quantum-confinement transition of a single dopant atom in a silicon FinFET. *Nature Physics*, **4**(656), 2008.

[33] J. J. L. Morton, D. R. McCamey, M. A. Eriksson, and S. A. Lyon. Embracing the quantum limit in silicon computing. *Nature*, **479**(345), 2011.

[34] A. M. Tyryshkin, S. Tojo, J. J. L. Morton, H. Riemann, N. V. Abrosimov, P. Becker, H.-J. Pohl, T. Schenkel, M. L. W. Thewalt, K. M. Itoh, and S. A. Lyon. Electron spin coherence exceeding seconds in high-purity silicon. *Nature Materials*, **11**(143), 2012.

[35] Efthimios Kaxiras. *Atomic and Electronic Structure of Solids*. Cambridge University Press, 1^{st} edition, 2003.

[36] F. J. Himpsel and D. E. Eastman. Photoemission studies of intrinsic surface states on Si(100). *Journal of Vacuum Science and Technology*, **16**(1297), 1979.

[37] F. J. Himpsel. Electronic structure and geometry of group IV semiconductor surfaces. *Physica B+C*, **117**(767), 1983.

[38] J. E. Ortega and F. J. Himpsel. Inverse-photoemission study of Ge(100), Si(100), and GaAs(100): Bulk bands and surface states. *Physical Review B*, **47**(2130), 1993.

[39] G. Le Lay, A. Cricenti, C. Ottaviani, P. Perfetti, T. Tanikawa, I. Matsuda, and S. Hasegawa. Evidence of asymmetric dimers down to 40 K at the clean Si(100) surface. *Physical Review B*, **66**(153317), 2002.

[40] L. Perdigao, D. Deresmes, B. Grandidier, M. Dubois, C. Delerue, G. Allan, and D. Stievenard. Semiconducting Surface Reconstructions of p-Type Si(100) Substrates at 5 K. *Physical Review Letters*, **92**(216101), 2004.

[41] R. A. Wolkow. Direct observation of an increase in buckled dimers on Si(001) at low temperature. *Physical Review Letters*, **68**(2636), 1992.

[42] D. Badt, H. Wengelnik, and H. Neddermeyer. Scanning tunneling microscopy at low temperatures on the c(4×2)/(2×1) phase transition of Si(100). *Journal of Vacuum Science and Technology B*, **12**(2015), 1994.

[43] M. Dubois, L. Perdigão, C. Delerue, G. Allan, B. Grandidier, D. Deresmes, and D. Stiévenard. Scanning tunneling microscopy and spectroscopy of reconstructed Si(100) surfaces. *Physical Review B*, **71**(165322), 2005.

[44] Y. Enta, S. Suzuki, and S. Kono. Angle-resolved-photoemission study of the electronic structure of the Si(001) c(4x2) surface. *Physical Review Letter*, **65**(2704), 1990.

[45] T. Tabata, T. Aruga, and Y. Murata. Order-disorder transition on Si(001) c(4×2) to (2×1). *Surface Science Letters*, **179**(L63), 1987.

[46] A. Ramstad, G. Brocks, and P. J. Kelly. Theoretical study of the Si(100) surface reconstruction. *Physical Review B*, **51**(14504), 1994.

[47] D. J. Chadi. Atomic and Electronic Structures of Reconstructed Si(100) Surfaces. *Physical Review Letters*, **43**(43), 1979.

[48] K. Inoue, Y. Morikawa, K. Terakura, and M. Nakayama. Order-disorder phase transition on the Si(001) surface: Critical role of dimer defects. *Physical Review B*, **49**(14774), 1994.

[49] J. E. Northrup. Electronic structure of Si(100)-c(4×2) calculated within the GW approximation. *Physical Review B*, **47**(10032), 1992.

[50] K. Sagisaka and D. Fujita. Standing waves on Si(100) and Ge(100) surfaces observed by scanning tunneling microscopy. *Physical Review B*, **72**(235327), 2005.

[51] J. J. Boland. Scanning tunneling microscopy study of the adsorption and recombinative desorption of hydrogen from the Si(100)-2×1 surface. *Journal of Vacuum Science and Technology A*, **10**(2458), 1992.

[52] D. K. Ferry. *Quantum Mechanics: An Introduction for Device Physicists and Electrical Engineers.* Taylor and Francis Group, UK, 2^{nd} edition, 2001.

[53] C. E. Burkhardt and J. J. Leventhal. *Foundations of Quantum Physics.* Springer Science + Business Media LLC, 1^{st} edition, 2008.

[54] G. Binnig and H. Rohrer. Scanning tunneling microscopy. *Helvetica Physica Acta*, **55**(726), 1982.

[55] G. Binnig and H. Rohrer. Scanning tunneling microscopy - from birth to adolescence. *Review of Modern Physics*, **56**(615), 1987.

[56] G. Binnig and H. Rohrer. Scanning tunneling microscopy. *Surface Science*, **126**(236), 1983.

[57] G. Binnig and H. Rohrer. Scanning tunneling microscopy. *IBM Journal of Research and Development*, **30**(355), 1986.

[58] G. Binnig, H. Rohrer, Ch. Gerber, and E. Weibel. Tunneling through a controllable vacuum gap. *Applied Physics Letters*, **40**(178), 1982.

[59] G. Binnig, H. Rohrer, Ch. Gerber, and E. Weibel. Surface Studies by Scanning Tunneling Microscopy. *Physical Review Letters*, **49**(57), 1982.

[60] C. Julian Chen. *Introduction to Scanning Tunneling Microscopy.* Oxford University Press, 1^{st} edition, 1993.

[61] J. A. Stroscio, R. M. Feenstra, and A. P. Fein. Local state density and long-range screening of adsorbed oxygen atoms on the GaAs(110) surface. *Physical Review Letters*, **58**(1668), 1987.

[62] V. A. Ukraintsev. Data evaluation technique for electron-tunneling spectroscopy. *Physical Review B*, **53**(11176), 1996.

[63] N. Li, M. Zinke-Allmang, and H. Iwasaki. A re-examination of scanning tunneling spectroscopy for its practical application in studies of surface electronic structures. *Surface Science*, **554**(253), 2004.

[64] B. Koslowski, C. Dietrich, A. Tschetschetkin, and P. Ziemann. Evaluation of scanning tunneling spectroscopy data: Approaching a quantitative determination of the electronic density of states. *Physical Review B*, **75**(035421), 2007.

[65] C. Wagner, R. Franke, and T. Fritz. Evaluation of I(V) curves in scanning tunneling spectroscopy of organic nanolayers. *Physical Review B*, **75**(235432), 2007.

[66] B. Naydenov and J. J. Boland. Variable-height scanning tunneling spectroscopy for local density of states recovery based on the one-dimensional WKB approximation. *Physical Review B*, **82**(245411), 2010.

[67] M. Passoni, F. Donati, A. Li Bassi, C. S. Casari, and C. E. Bottani. Recovery of local density of states using scanning tunneling spectroscopy. *Physical Review B*, **79**(045404), 2009.

[68] N. Garcia. Theory of the scanning tunneling microscopy and spectroscopy: Resolution, image and field states, and thin oxide layers. *IBM Journal of Research and Development*, **30**(533), 1986.

[69] J. H. Coombs and J. B. Pethica. Properties of vacuum tunneling currents: Anomalous barrier heights. *IBM Journal of Research and Development*, **30**(455), 1986.

[70] J. Tersoff and D. R. Hamann. Theory and Application for the Scanning Tunneling Microscope. *Physical Review Letters*, **50**(1998), 1983.

[71] J. Bardeen. Tunnelling from a Many-Particle point of View. *Physical Review Letters*, **6**(57), 1961.

[72] L. D. Landau and L. M. Lifshitz. *Quantum Mechanics*. Oxford Pergamon Press, 3^{rd} edition, 1977.

[73] I. Giaever. Energy Gap in Superconductors Measured by Electron Tunneling. *Physical Review Letters*, **5**(147), 1960.

[74] I. Giaever. Electron Tunneling Between Two Superconductors. *Physical Review Letters*, **5**(464), 1960.

[75] I. Giaever and K. Megerle. Study of Superconductors by Electron Tunneling. *Physical Review*, **122**(1101), 1961.

[76] J. Tersoff and D. R. Hamann. Theory of the scanning tunneling microscope. *Physical Review B*, **31**(805), 1985.

[77] E. Stoll. Resolution of the scanning tunneling microscope. *Surface Science*, **143**(L411), 1984.

[78] N. Garcia, C. Ocal, and F. Floers. Model theory for scanning tunneling microscopy: Application to Au(110)-2x1. *Physical Review Letters*, **50**(2002), 1983.

[79] C. J. Chen. Tunneling matrix elements in three-dimensional space: The derivative rule and the sum rule. *Physical Review B*, **42**(8841), 1990.

[80] C. J. Chen. Effects of $m \neq 0$ tip states in scanning tunneling microscopy: The explanation of corrugation reversal. *Physical Review Letters*, **69**(1656), 1992.

[81] O. Paz and J. M. Soler. Efficient and reliable method for the simulation of scanning tunneling images and spectra with local basis sets. *Physica Status Solidi B*, **243**(1080), 2006.

[82] D. Lawunmi and M. C. Payne. Theoretical investigation of the scanning tunnelling microscope image of graphite. *Journal of Physics: Condensed Matter*, **2**(3881), 1990.

[83] C. J. Chen. Origin of atomic resolution on metal surfaces in scanning tunneling microscopy. *Physical Review Letters*, **65**(448), 1990.

[84] J. Tersoff and N. D. Lang. Tip-dependent corrugation of graphite in scanning tunneling microscopy. *Physical Review Letters*, **65**(1132), 1990.

[85] M. Tsukada, K. Kobayashi, and N. Isshiki. Effect of tip atomic and electronic structure on scanning tunneling microscopy/spectroscopy. *Surface Science*, **242**(12), 1991.

[86] J. M. Bass and C. C. Matthai. Theoretical simulation of scanning-tunneling-microscopy images of the GaAs(001) $\beta(2 \times 4)$ and $\beta(4 \times 2)$ surfaces. *Physical Review B*, **50**(11212), 1994.

[87] W.A. Hofer and J. Redinger. Scanning tunneling microscopy of binary alloys: first principles calculation of the current for PtX (100) surfaces. *Surface Science*, **447**(51), 2000.

[88] W. A. Hofer, A. J. Fisher, R. A. Wolkow, and P. Grütter. Surface Relaxations, Current Enhancements, and Absolute Distances in High Resolution Scanning Tunneling Microscopy. *Physical Review Letters*, **87**(236104), 2001.

[89] J. A. Appelbaum and W. F. Brinkman. Theory of Many-Body Effects in Tunneling. *Physical Review*, **186**(464), 1969.

[90] T. E. Feuchtwang. Tunneling theory without the transfer-Hamiltonian formalism. I. *Physical Review B*, **10**(4121), 1974.

[91] T. E. Feuchtwang. Tunneling theory without the transfer-Hamiltonian formalism. II. Resonant and inelastic tunneling across a junction of finite width. *Physical Review B*, **10**(4135), 1974.

[92] T. E. Feuchtwang. Theory of tunneling without transfer Hamiltonian: Relation between continuum and discrete formalisms, and equivalence with elementary theory for noninteracting systems. *Physical Review B*, **12**(3979), 1975.

[93] T. E. Feuchtwang. Tunneling theory without the transfer-Hamiltonian formalism. IV. The abrupt (zero-width) three-dimensional junction. *Physical Review B*, **13**(517), 1976.

[94] T. E. Feuchtwang. Tunneling theory without the transfer Hamiltonian formalism. V. A theory of inelastic-electron-tunneling spectroscopy. *Physical Review B*, **20**(430), 1979.

[95] P.Sautet and C. Joachim. Electronic interference produced by a benzene embedded in a polyacetylene chain. *Chemical Physics Letters*, **153**(511), 1988.

[96] P.Sautet and C. Joachim. Calculation of the benzene on rhodium STM images. *Chemical Physics Letters*, **185**(23), 1991.

[97] C. Noguera. Theoretical approach to the scanning tunneling microscope. *Physical Review B*, **42**(1629), 1990.

[98] G. Doyen, D. Drakova, and M. Scheffler. Green-function theory of scanning tunneling microscopy: Tunnel current and current density for clean metal surfaces. *Physical Review B*, **47**(9778), 1993.

[99] F. Flores, P.L. de Andres, F.J. Garcia-Vidal, L. Jurczyszyn, N. Mingo, and R. Perez. Adsorption of noble gases on metal surfaces and the scanning tunneling microscope. *Progress in Surface Science*, **48**(27), 1995.

[100] H. Ness and A. J. Fisher. Nonperturbative evaluation of STM tunneling probabilities from ab initio calculations. *Physical Review B*, **56**(12469), 1997.

[101] J. Cerdá, M. A. Van Hove, P. Sautet, and M. Salmeron. Efficient method for the simulation of STM images. I. Generalized Green-function formalism. *Physical Review B*, **56**(15885), 1997.

[102] M. Brandbyge, J.-L. Mozos, P. Ordejón, J. Taylor, and K. Stokbro. Density-functional method for nonequilibrium electron transport. *Physical Review B*, **65**(165401), 2002.

[103] C. Toher, I. Rungger, and S. Sanvito. Simulating STM transport in alkanes from first principles. *Physical Review B*, **79**(205427), 2009.

[104] N. Baadji, S. Kuck, J. Brede, G. Hoffmann, R. Wiesendanger, and S. Sanvito. Controlled sequential dehydrogenation of single molecules by scanning tunneling microscopy. *Physical Review B*, **82**(115447), 2010.

[105] P. Hohenberg and W. Kohn. Inhomogeneous Electron Gas. *Physical Review*, **136**(B864), 1964.

[106] W. Kohn and L. J. Sham. Self-Consistent Equations Including Exchange and Correlation Effects. *Physical Review*, **140**(A1133), 1965.

[107] L. J. Sham and W. Kohn. One Particle Properties of an Inhomogeneous Interacting Electron Gas. *Physical Review*, **145**(2), 1966.

[108] W. Kohn. Electronic structure of matter. *Reviews of Modern Physics*, **71**(5), 1999.

[109] S. Datta. Electrical resistance: an atomistic view. *Nanotechnology*, **15**(S433), 2004.

[110] A. R. Rocha, V. M. García-Suárez, S. Bailey, C. Lambert, J. Ferrer, and S. Sanvito. Spin and molecular electronics in atomically generated orbital landscapes. *Physical Review B*, **73**(085414), 2006.

[111] A. R. Rocha, V. M. Garca-surez, S. W. Bailey, C. J. Lambert, J. Ferrer, and S. Sanvito. Towards molecular spintronics. *Nature Materials*, **4**(335), 2005.

[112] E. Schröedinger. Quantisierung als Eigenwertproblem. *Annalen der Physik*, **79**(361), 1926.

[113] J. C. Slater. The Theory of Complex Spectra. *Physical Review*, **34**(1293), 1929.

[114] J. Kohanoff. *Electronic Structure Calculations for Solids and Molecules*. Cambridge University Press, 1^{st} edition, 2006.

[115] M. Born and R. Oppenheimer. Zur Quantentheorie der Molekeln. *Annalen der Physik*, **389**(457), 1927.

[116] P. Ehrenfest. Bemerkung ber die angenherte gltigkeit der klassischen mechanik innerhalb der quantenmechanik. *Zeitschrift für Physik*, **45**(455), 1927.

[117] H. Hellmann. *Einführung in die Quantenchemie*. Franz Deuticke, first edition, 1937.

[118] R. P. Feynman. Forces in molecules. *Physical Review*, **56**(340), 1939.

[119] S. Habib, K. Shizumeand, and W. H. Zurek. Decoherence, chaos and the correspondence priciple. *Physical Review Letters*, **80**(4361), 1998.

[120] N. C. Handy and A. M. Lee. The adiabatic approximation. *Chemical Physical Letters*, **252**(425), 1996.

[121] D. R. Hartree. The wave mechanics of an atom with a non-Coulomb central field. Part I. Theory and Methods. *Mathematical Proceedings of the Cambridge Philosophical Society*, **24**(89), 1928.

[122] J. C. Slater. The self-consistent-field and the structure of atoms. *Physical Review*, **32**(339), 1928.

[123] V. Fock. Näherungsmethode zur Losung des quantenmechanischen Mehrkörperprobleme. *Zeitschrift für Physik*, **61**(126), 1930.

[124] Alessio Filippetti. Proprietà strutturali di superfici metalliche e di semiconduttori. *Ph.D. Thesis, Università degli Studi di Cagliari*, 1997.

[125] U. von Barth and L. Hedin. A local exchange-correlation potential for the spin polarized case: I. *Journal of Physics C: Solid State Physics*, **5**(1629), 1972.

[126] J. C. Stoddart and N. H. March. Density-functional theory of magnetic instabilities in metals. *Annals of Physics*, **64**(174), 1971.

[127] M. M. Pant and A. K. Rajagopal. Theory of inhomogeneous magnetic electron gas. *Solid State Communications*, **10**(1157), 1972.

[128] A. K. Rajagopal and J. Callaway. Inhomogeneous electron gas. *Physical Review B*, **7**(1912), 1973.

[129] T. Oda, A. Pasquarello, and R. Car. Fully unconstrained approach to non-collinear magnetism: application to small Fe clusters. *Physical Review Letters*, **80**(3622), 1998.

[130] J. E. Peralta, G. E. Scuseria, and M. J. Frisch. Noncollinear magnetism in density functional calculations. *Physical Review B*, **75**(125119), 2007.

[131] L. M. Sandratskii. Energy Band Structure Calculations for Crystals with Spiral Magnetic Structure. *Physica Status Solidi (b)*, **136**(167), 1986.

[132] J. Kübler, K.-H. Höck, J. Sticht, and A. R. Williams. Density functional theory of non-collinear magnetism. *Journal of Physics F: Metal Physics*, **18**(469), 1988.

[133] J. Sticht, K.-H. Höck, and J. Kübler. Non-collinear itinerant magnetism: the case of Mn_3Sn. *Journal of Physics: Condensed Matter*, **1**(8155), 1989.

[134] D. M. Ceperley and B. J. Alder. Ground State of the Electron Gas by a Stochastic Method. *Physical Review Letters*, **45**(566), 1980.

[135] J. P. Perdew and A. Zunger. Self-interaction correction to density-functional approximations for many-electron systems. *Physical Review B*, **23**(5048), 1981.

[136] Matteo Cococcioni. A LDA+U study of selected iron compounds. *Ph.D. Thesis, Università degli Studi di Trieste*, 2002.

[137] J. P. Perdew and W. Yue. Accurate and simple density functional for the electronic exchange energy: Generalized gradient approximation. *Physical Review B*, **33**(8800), 1986.

[138] D. C. Langreth and M. J. Mehl. Easily implementable nonlocal exchange-correlation energy functional. *Physical Review Letters*, **47**(446), 1981.

[139] J. P. Perdew, K. Burke, and M. Ernzerhof. Generalized Gradient Approximation Made Simple. *Physical Review Letters*, **77**(3865), 1996.

[140] J. P. Perdew and Y. Wang. Accurate and simple analytic representation of the electron-gas correlation energy. *Physical Review B*, **45**(13244), 1992.

[141] J. P. Perdew, J. Tao, V. N. Staroverov, and G. E. Scuseria. Meta-generalized gradient approximation: explanation of a realistic nonempirical density functional. *Journal of Chemical Physics*, **120**(6898), 2004.

[142] J. P. Perdew, A. Ruzsinszky, G. I. Csonka, O. A. Vydrov, G. E. Scuseria, L. A. Constantin, X. Zhou, and K. Burke. Restoring the Density-Gradient Expansion for Exchange in Solids and Surfaces. *Physical Review Letters*, **100**(136406), 2008.

[143] V. I. Anisimov, J. Zaanen, and O. K. Andersen. Band theory and Mott insulators: Hubbard U instead of Stoner I. *Physical Review B*, **44**(943), 1991.

[144] V. I. Anisimov, I. V. Solovyev, M. A. Korotin, M. T. Czyżyk, and G. A. Sawatzky. Density-functional theory and NiO photoemission spectra. *Physical Review B*, **48**(16929), 1993.

[145] I. V. Solovyev, P. H. Dederichs, and V. I. Anisimov. Corrected atomic limit in the local-density approximation and the electronic structure of d impurities in Rb. *Physical Review B*, **50**(16861), 1994.

[146] J. Hubbard. Electron correlations in narrow energy bands. IV. The atomic representation. *Proceedings of the Royal Society London*, **285**(542), 1965.

[147] A. I. Liechtenstein, V. I. Anisimov, and J. Zaanen. Density-functional theory and strong interactions: Orbital ordering in Mott-Hubbard insulators. *Physical Review B*, **52**(R5467), 1995.

[148] V. I. Anisimov, F. Aryasetiawan, and A. Liechtenstein. First-principle calculations of the electronic structure and spectra of strongly correlated systems: the LDA+U method. *Journal of Physics: Condensed Matter*, **9**(767), 1997.

[149] S. L. Dudarev, G. A. Botton, S. Y. Savrasov, C. J. Humphreys, and A. P. Sutton. Electron-energy-loss spectra and the structural stability of nickel oxide: An LSDA+U study. *Physical Review B*, **57**(1505), 1998.

[150] M. Cococcioni and S. de Gironcoli. Linear response approach to the calculation of the effective interaction parameters in the LDA+U method. *Physical Review B*, **71**(035105), 2005.

[151] A. Filippetti and N. A. Spaldin. Self-interaction-corrected pseudopotential scheme for magnetic and strongly-correlated systems. *Physical Review B*, **67**(125109), 2003.

[152] A. Filippetti and N. A. Spaldin. Strong-correlation effects in born effective charges. *Physical Review B*, **68**(045111), 2003.

[153] C. D. Pemmaraju, T. Archer, D. Snchez-Portal, and S. Sanvito. Atomic-orbital-based approximate self-interaction correction scheme for molecules and solids. *Physical Review B*, **75**(045101), 2007.

[154] D. Vogel, P. Krüger, and J. Pollmann. Self-interaction and relaxation-corrected pseudopotentials for II-VI semiconductors. *Physical Review B*, **54**(5495), 1996.

[155] T. Archer, C. D. Pemmaraju, S. Sanvito, C. Franchini, J. He, A. Filippetti, P. Delugas, D. Puggioni, V. Fiorentini, R. Tiwari, and P. Majumdar. Exchange interactions and magnetic phases of transition metal oxides: Benchmarking advanced ab initio methods. *Physical Review B*, **84**(115114), 2011.

[156] A. Droghetti, C. D. Pemmaraju, and S. Sanvito. Polaronic distortion and vacancy-induced magnetism in MgO. *Physical Review B*, **81**(092403), 2010.

[157] C. D. Pemmaraju, I. Rungger, X. Chen, A. R. Rocha, and S. Sanvito. Ab initio study of electron transport in dry poly(G)-poly(C) A-DNA strands. *Physical Review B*, **82**(125426), 2010.

[158] A. Filippetti, C. D. Pemmaraju, S. Sanvito, P. Delugas, D. Puggioni, and Vincenzo Fiorentini. Variational pseudo-self-interaction-corrected density functional approach to the ab initio description of correlated solids and molecules. *Physical Review B*, **84**(195127), 2011.

[159] G. M. Lopez, A. Filippetti, M. Mantega, and V. Fiorentini. First-principles calculation of electronic and structural properties of $YBa_2Cu_3O_{6+y}$. *Physical Review B*, **82**(195122), 2010.

[160] G. Peralta, D. Puggioni, A. Filippetti, and V. Fiorentini. Jahn-Teller stabilization of magnetic and orbital ordering in rocksalt CuO. *Physical Review B*, **80**(140408R), 2009.

[161] A. Filippetti and V. Fiorentini. Magnetic Ordering in CuO from First Principles: A Cuprate Antiferromagnet with Fully Three-Dimensional Exchange Interactions. *Physical Review Letters*, **95**(086405), 2005.

[162] Y. Zhang and W. Yang. A challenge for density functionals: Self-interaction error increases for systems with a noninteger number of electrons. *Journal of Chemical Physics*, **109**(2604), 1998.

[163] S. Datta. *Electronic Transport in Mesoscopic Systems*. Cambridge University Press, Cambridge, UK, 1^{st} edition, 1995.

[164] C. Caroli, R. Combescot, P. Nozieres, and D. Saint-James. A direct calculation of the tunnelling current: IV. Electron-phonon interaction effects. *Journal of Physics C: Solid State Physics*, **5**(21), 1972.

[165] J. Ferrer, A. Martn-Rodero, and F. Flores. Contact resistance in the scanning tunneling microscope at very small distances. *Physical Review B*, **38**(10113), 1988.

[166] L. V. Keldysh. Diagram technique for non-equilibrium processes. *Soviet Physics JETP*, **20**(1018), 1965.

[167] E. Economou. *Green's Functions in Quantum Physics*. Spinger-Verlag, Berlin, 1^{st} edition, 1995.

[168] J. M. Soler, E. Artacho, J. D. Gale, A. García, J. Junquera, P. Ordejón, and D. Sánchez-Portal. The SIESTA method for ab-initio order-N materials simulation. *Journal of Physics: Condensed Matter*, **14**(2745), 2002.

[169] G. Kresse and J. Hafner. Ab initio molecular dynamics for liquid metals. *Physical Review B*, **47**(558), 1993.

[170] G. Kresse and J. Hafner. Ab initio molecular-dynamics simulation of the liquid-metalamorphous-semiconductor transition in germanium. *Physical Review B*, **49**(14251), 1994.

[171] G. Kresse and J. Furthmüller. Efficiency of ab-initio total energy calculations for metals and semiconductors using a plane-wave basis set. *Computational Material Science*, **6**(15), 1996.

[172] G. Kresse and J. Furthmüller. Efficient iterative schemes for ab initio total-energy calculations using a plane-wave basis set. *Physical Review B*, **54**(11169), 1996.

[173] G. Kresse and D. Joubert. From ultrasoft pseudopotentials to the projector augmented-wave method. *Physical Review B*, **59**(1758), 1999.

[174] I. P. Batra. From uncertainty to certainty in quantum conductance of nanowires. *Solid State Communications*, **124**(463), 2002.

[175] S. Sanvito, C. J. Lambert, J. H. Jefferson, and A. M. Bratkovsky. General Greens-function formalism for transport calculations with spd hamiltonians and giant magnetoresistance in Co- and Ni-based magnetic multilayers. *Physical Review B*, **59**(11936), 1999.

[176] Y. Meir and N. S. Wingreen. Landauer formula for the current through an interacting electron region. *Physical Review Letters*, **68**(2512), 1992.

[177] Stefano Sanvito. Ab-initio methods for spin-transport at the nanoscale level. *unpublished*, .

[178] O. F. Sankey and D. J. Niklewski. Ab initio multicenter tight-binding model for molecular-dynamics simulations and other applications in covalent systems. *Physical Review B*, **40**(3979), 1989.

[179] N. Troullier and J. L. Martins. Efficient pseudopotentials for plane-wave calculations. *Physical Review B*, **43**(1993), 1991.

[180] N. Troullier and J. L. Martins. Efficient pseudopotentials for plane-wave calculations. II. Operators for fast iterative diagonalization. *Physical Review B*, **43**(8861), 1991.

[181] S. G. Louie, S. Froyen, and Marvin L. Cohen. Nonlinear ionic pseudopotentials in spin-density-functional calculations. *Physical Review B*, **26**(1738), 1982.

[182] M.M. Fadlallah, C. Schuster, U. Eckern, and U. Schwingenschlögl. Modification of the electronic transport in Au by prototypical impurities and interlayers. *Europhysics Letters*, **89**(47003), 2010.

[183] I. Rungger, O. Mryasov, and S. Sanvito. Resonant electronic states and I-V curves of Fe/MgO/Fe(100) tunnel junctions. *Physical Review B*, **79**(094414), 2009.

[184] N. M. Caffrey, T. Archer, I. Rungger, and S. Sanvito. Prediction of large bias-dependent magnetoresistance in all-oxide magnetic tunnel junctions with a ferroelectric barrier. *Physical Review B*, **83**(125409), 2011.

[185] C. Toher and S. Sanvito. Effects of self-interaction corrections on the transport properties of phenyl-based molecular junctions. *Physical Review B*, **77**(155402), 2008.

[186] R. Pilevarshahri, I. Rungger, T. Archer, S. Sanvito, and N. Shahtahmassebi. Spin transport in higher n-acene molecules. *Physical Review B*, **84**(174437), 2011.

[187] A. R. Rocha, T. Archer, and S. Sanvito. Search for magnetoresistance in excess of 1000% in Ni point contacts: Density functional calculations. *Physical Review B*, **76**(054435), 2007.

[188] A. Garcia-Fuente, A. Vega, V. M. Garcia-Suarez, and J. Ferrer. Impact of dimerization and stretching on the transport properties of molybdenum atomic wires. *Nanotechnology*, **21**(095205), 2010.

[189] X. Shen, L. Sun, Z. Yi, E. Benassi, R. Zhang, Z. Shen, S. Sanvito, and S. Hou. Spin transport properties of 3d transition metal(II) phthalocyanines in contact with single-walled carbon nanotube electrodes. *Physical Chemistry Chemical Physics*, **12**(10805), 2010.

[190] P. Schwerdtfeger. The Pseudopotential Approximation in Electronic Structure Theory. *ChemPhysChem*, **12**(3143), 2011.

[191] D. R. Hamann, M. Schlüter, and C. Chiang. Norm-conserving pseudopotentials. *Physical Review Letters*, **43**(1494), 1979.

[192] J. C. Phillips and L. Kleinman. New Method for Calculating Wave Functions in Crystals and Molecules. *Physical Review*, **116**(287), 1959.

[193] J. D. Weeks and S. A. Rice. Use of Pseudopotentials in Atomic-Structure Calculations. *The Journal of Chemical Physics*, **49**(2741), 1968.

[194] W. E. Pickett. Pseudopotential methods in condensed matter applications. *Computer Physics Reports*, **9**(115), 1989.

[195] J. S. Lin, A. Qteish, M. C. Payne, and V. Heine. Optimized and transferable nonlocal separable *ab initio* pseudopotentials. *Physical Review B*, **47**(4174), 1993.

[196] V. Heine. The pseudopotential concept. *Solid States Physics*, **24**(1), 1970.

[197] J. Ihm. Total energy calculations in solid state physics. *Reports on Progress in Physics*, **51**(105), 1988.

[198] H. Hellmann. A New Approximation Method in the Problem of Many Electrons. *The Journal of Chemical Physics*, **3**(61), 1935.

[199] H. Hellmann and W. Kassatotschkin. Metallic Binding According to the Combined Approximation Procedure. *The Journal of Chemical Physics*, **4**(324), 1936.

[200] W. C. Topp and J. J. Hopfield. Chemically Motivated Pseudopotential for Sodium. *Physical Review B*, **7**(1295), 1973.

[201] T. Starkloff and J. D. Joannopoulos. Local pseudopotential theory for transition metals. *Physical Review B*, **16**(5212), 1977.

[202] G. B. Bachelet, D. R. Hamann, and M. Schlüter. Pseudopotentials that work: From H to Pu. *Physical Review B*, **26**(4199), 1982.

[203] S. Goedecker and K. Maschke. Transferability of pseudopotentials. *Physical Review A*, **45**(88), 1992.

[204] F. Bloch. Über die Quantenmechanik der Elektronen in Kristallgittern. *Zeitschrift für Physik*, **52**(555), 1928.

[205] D. J. Chadi and M. L. Cohen. Special Points in the Brillouin Zone. *Physical Review B*, **8**(5747), 1973.

[206] H. J. Monkhorst and J. D. Pack. Special points for Brillouin-zone integrations. *Physical Review B*, **13**(5188), 1976.

[207] A Baldereschi. Mean-Value Point in the Brillouin Zone. *Physical Review B*, **7**(5212), 1973.

[208] M. Methfessel and A. T. Paxton. High-precision sampling for Brillouin-zone integration in metals. *Physical Review B*, **40**(3616), 1989.

[209] D. Vanderbilt. Optimally smooth norm-conserving pseudopotentials. *Physical Review B*, **32**(8412), 1985.

[210] D. Vanderbilt. Soft self-consistent pseudopotentials in a generalized eigenvalue formalism. *Physical Review B*, **41**(7892), 1990.

[211] P. E. Blöchl. Projector augmented-wave method. *Physical Review B*, **50**(17953), 1994.

[212] D. M. Wood and A. Zunger. A new method for diagonalising large matrices. *Journal of Physics A: Mathematical and General*, **18**(1343), 1985.

[213] P. Pulay. Convergence acceleration of iterative sequences. the case of SCF iteration. *Chemical Physics Letters*, **73**(393), 1980.

[214] E. R. Davidson. *Methods in Computational Molecular Physics.* Lawrence Berkeley Laboratory, University of California, 1^{st} edition, 1978.

[215] O. Jepson and O. K. Anderson. The electronic structure of h.c.p. Ytterbium. *Solid State Communications*, **9**(1763), 1971.

[216] G. Lehmann and M. Taut. On the Numerical Calculation of the Density of States and Related Properties. *physica status solidi b*, **54**(469), 1972.

[217] P. E. Blöchl, O. Jepsen, and O. K. Andersen. Improved tetrahedron method for Brillouin-zone integrations. *Physical Review B*, **49**(16223), 1994.

[218] O. K. Andersen. Linear methods in band theory. *Physical Review B*, **12**(3060), 1975.

[219] M. W. Radny, P. V. Smith, T. C. G. Reusch, O. Warschkow, N. A. Marks, H. F. Wilson, S. R. Schofield, N. J. Curson, D. R. McKenzie, and M. Y. Simmons. Single hydrogen atoms on the Si(001) surface. *Physical Review B*, **76**(155302), 2007.

[220] T. C. G. Reusch, O. Warschkow, M. W. Radny, P.V. Smith, N. A. Marks, N. J. Curson, D. R. McKenzie, and M. Y. Simmons. Doping and STM tip-induced changes to single dangling bonds on Si(001). *Surface Science*, **601**(4036), 2007.

[221] G. A. Shah, M. W. Radny, P. V. Smith, S. R. Schofield, and N. J. Curson. Electronic effects of single H atoms on Ge(001) revisited. *Journal of Chemical Physics*, **133**(014703), 2010.

[222] M. Mantega, I. Rungger, B. Naydenov, J. J. Boland, and S. Sanvito. Spectroscopic characterization of a single dangling bond on a bare Si(100)-c(4 × 2) surface for *n*- and *p*-type doping. *Physical Review B*, **86**(035318), 2012.

[223] B. Naydenov, P. Ryan, L. C. Teague, and J. J. Boland. Measuring the Force of Interaction between a Metallic Probe and a Single Molecule. *Physical Review Letters*, **97**(098304), 2006.

[224] E. Hill, B. Freelon, and E. Ganz. Diffusion of hydrogen on the Si(001) surface investigated by STM atom tracking. *Physical Review B*, **60**(15896), 1999.

[225] D. R. Bowler, J. H. G. Owen, C. M. Goringe, K. Miki, and G. A. D. Briggs. An experimental-theoretical study of the behaviour of hydrogen on the Si(001) surface. *Journal of Physics: Condensed Matter*, **12**(7655), 2000.

[226] B. Naydenov, M. Mantega, I. Rungger, S. Sanvito, and J. J. Boland. Scattered surface charge density: A tool for surface characterization. *Physical Review B*, **84**(195321), 2011.

[227] E. C. Stoner. The Distribution of Electrons among Atomic Levels. *Philosophical Magazine*, **48**(719), 1924.

[228] I. Rungger and S. Sanvito. Algorithm for the construction of self-energies for electronic transport calculations based on singularity elimination and singular value decomposition. *Physical Review B*, **78**(035407), 2008.

[229] O. R. Davies and J. E. Inglesfield. Embedding method for conductance of DNA. *Physical Review B*, **69**(195110), 2004.

[230] M. F. Crommie, C. P. Lutz, and D. M. Eigler. Confinement of Electrons to Quantum Corrals on a Metal Surface. *Science*, **262**(218), 1993.

[231] P. Avouris. Studies of confined states and quantum size effects with scanning tunneling microscopy. *Solid State Communications*, **92**(11), 1994.

[232] B. Naydenov, M. Mantega, I. Rungger, S. Sanvito, and J. J. Boland. Gating effects on the dimer rows of Si(100)-c(4 $\times$ 2) surface. *in preparation*, , 2012.

[233] M. König, S. Wiedmann C. Brüne, A. Roth, H. Buhmann, L. W. Molenkamp, X.-L. Qi, and S.-C. Zhang. Quantum Spin Hall Insulator State in HgTe Quantum Wells. *Science*, **318**(766), 2007.

[234] C. L. Kane and E. J. Mele. Z_2 Topological Order and the Quantum Spin Hall Effect. *Physical Review Letters*, **95**(146802), 2005.

[235] L. Fu and C. L. Kane. Probing Neutral Majorana Fermion Edge Modes with Charge Transport. *Physical Review Letters*, **102**(216403), 2009.

[236] L. Fu and C. L. Kane. Topological insulators with inversion symmetry. *Physical Review B*, **76**(045302), 2007.

[237] L. Fu, C. L. Kane, and E. J. Mele. Topological Insulators in Three Dimensions. *Physical Review Letters*, **98**(106803), 2007.

[238] J. E. Moore and L. Balents. Topological invariants of time-reversal-invariant band structures. *Physical Review B*, **75**(121306), 2007.

[239] R. Roy. Z_2 classification of quantum spin Hall systems: An approach using time-reversal invariance. *Physical Review B*, **79**(195321), 2009.

[240] R. Roy. Topological phases and the quantum spin Hall effect in three dimensions. *Physical Review B*, **79**(195322), 2009.

[241] B. A. Bernevig, T. L. Hughes, and S.-C. Zhang. Quantum Spin Hall Effect and Topological Phase Transition in HgTe Quantum Wells. *Science*, **314**(1757), 2006.

[242] D. Hsieh, D. Qian, L. Wray, Y. Xia, Y. S. Hor, R. J. Cava, and M. Z. Hasan. A topological Dirac insulator in a quantum spin Hall phase. *Nature*, **452**(970), 2008.

[243] D. Hsieh, Y. Xia, D. Qian, L. Wray, J. H. Dil, F. Meier, J. Osterwalder, L. Patthey, J. G. Checkelsky, N. P. Ong, A. V. Fedorov, H. Lin, A. Bansil, D. Grauer, Y. S. Hor, R. J. Cava, and M. Z. Hasan. A tunable topological insulator in the spin helical Dirac transport regime. *Nature*, **460**(1101), 2009.

[244] Y. Xia, D. Qian, D. Hsieh, L. Wray, A. Pal, H. Lin, A. Bansil, D. Grauer, Y. S. Hor, R. J. Cava, and M. Z. Hasan. Observation of a large-gap topological-insulator class with a single Dirac cone on the surface. *Nature Physics*, **5**(398), 2009.

[245] H. Zhang, C.-X. Liu, X.-L. Qi, X. Dai, Z. Fang, and S.-C. Zhang. Topological insulators in Bi_2Se_3, Bi_2Te_3 and Sb_2Te_3 with a single Dirac cone on the surface. *Nature Physics*, **5**(438), 2009.

[246] Y. L. Chen, J. G. Analytis, J.-H. Chu, Z. K. Liu, S.-K. Mo, X. L. Qi, H. J. Zhang, D. H. Lu, X. Dai, Z. Fang, S. C. Zhang, I. R. Fisher, Z. Hussain, and Z.-X. Shen. Experimental Realization of a Three-Dimensional Topological Insulator, Bi_2Te_3. *Science*, **325**(178), 2009.

[247] J. Moore. Topological insulators: The next generation. *Nature Physics*, **5**(378), 2009.

[248] M. Z. Hasan and C. L. Kane. Colloquium: Topological insulators. *Reviews of Modern Physics*, **82**(3045), 2010.

[249] K. v. Klitzing, G. Dorda, and M. Pepper. New Method for High-Accuracy Determination of the Fine-Structure Constant Based on Quantized Hall Resistance. *Physical Review Letters*, **45**(494), 1980.

[250] M. König, H. Buhmann, L. W. Molenkamp, T. Hughes, C.-X. Liu, X.-L. Qi, and S.-C. Zhang. The Quantum Spin Hall Effect: Theory and Experiment. *Journal of the Physical Society of Japan*, **77**(031007), 2008.

[251] B. A. Bernevig and S.-C. Zhang. Quantum Spin Hall Effect. *Physical Review Letters*, **96**(106802), 2006.

[252] D. Hsieh, Y. Xia, L. Wray, D. Qian, A. Pal, J. H. Dil, J. Osterwalder, F. Meier, G. Bihlmayer, C. L. Kane, Y. S. Hor, R. J. Cava, and M. Z. Hasan. Observation of Unconventional Quantum Spin Textures in Topological Insulators. *Science*, **323**(919), 2009.

[253] C. L. Kane and E. J. Mele. Quantum Spin Hall Effect in Graphene. *Physical Review Letters*, **95**(226801), 2005.

[254] X.-L. Qi, R. Li, J. Zang, and S.-C. Zhang. Inducing a Magnetic Monopole with Topological Surface States. *Science*, **323**(1184), 2009.

[255] X.-L. Qi, T. L. Hughes, and S.-C. Zhang. Topological field theory of time-reversal invariant insulators. *Physical Review B*, **78**(195424), 2008.

[256] X.-L. Qi and S.-C. Zhang. The quantum spin Hall effect and topological insulators. *Physics Today*, **63**(33), 2010.

[257] R. B. Laughlin. Quantized Hall conductivity in two dimensions. *Physical Review B*, **23**(5632), 1981.

[258] D. R. Yennie. Integral quantum Hall effect for nonspecialists. *Reviews of Modern Physics*, **59**(781), 1987.

[259] M. Franz. U-turns strictly prohibited. *Nature*, **466** (323), 2010.

[260] C. Wu, B. A. Bernevig, and S.-C. Zhang. Helical Liquid and the Edge of Quantum Spin Hall Systems. *Physical Review Letters*, **96**(106401), 2006.

[261] C. Xu and J. E. Moore. Stability of the quantum spin Hall effect: Effects of interactions, disorder, and Z_2 topology. *Physical Review B*, **73**(045322), 2006.

[262] S.-S. Lee and S. Ryu. Many-Body Generalization of the Z_2 Topological Invariant for the Quantum Spin Hall Effect. *Physical Review Letters*, **100**(186807), 2008.

[263] O. V. Yazyev, J. E. Moore, and S. G. Louie. Spin Polarization and Transport of Surface States in the Topological Insulators Bi_2Se_3 and Bi_2Te_3 from First Principles. *Physical Review Letters*, **105**(266806), 2010.

[264] A. H. Castro Neto, F. Guinea, N. M. R. Peres, K. S. Novoselov, and A. K. Geim. The electronic properties of graphene. *Reviews of Modern Physics*, **81**(109), 2009.

[265] P. R. Wallace. The Band Theory of Graphite. *Physical Review*, **71**(622), 1947.

[266] J. W. McClure. Diamagnetism of Graphite. *Physical Review*, **104**(666), 1956.

[267] J. C. Slonczewski and P. R. Weiss. Band Structure of Graphite. *Physical Review*, **109**(272), 1958.

[268] H. P. Boehm, A. Clauss, G. O. Fischer, and U. Hofmann. Das Adsorptionsverhalten sehr dünner Kohlenstoff-Folien. *Zeitschrift für anorganische und allgemeine Chemie*, **316**(119), 1962.

[269] K. S. Novoselov, D. Jiang, F. Schedin, T. J. Booth, V. V. Khotkevich, S. V. Morozov, and A. K. Geim. Two-dimensional atomic crystals. *Proceedings of the National Academy of Science of USA*, **102**(10451), 2005.

[270] K. S. Novoselov, A. K. Geim, S. V. Morozov, D. Jiang, M. I. Katsnelson, I. V. Grigorieva, S. V. Dubonos, and A. A. Firsov. Two-dimensional gas of massless Dirac fermions in graphene. *Nature*, **438**(197), 2005.

[271] Y. Zhang, Y.-W. Tan, H. L. Stormer, and P. Kim. Experimental observation of the quantum Hall effect and Berry's phase in graphene. *Nature*, **438**(201), 2005.

[272] P. Avouris, Z. Chen, and V. Perebeinos. Carbon-based electronics. *Nature Nanotechnology*, **2**(605), 2007.

[273] G. W. Semenoff. Condensed-Matter Simulation of a Three-Dimensional Anomaly. *Physical Review Letters*, **53**(2449), 1984.

[274] A. K. Geim and K. S. Novoselov. The rise of graphene. *Nature Materials*, **6**(183), 2007.

[275] S. V. Morozov, K. S. Novoselov, M. I. Katsnelson, F. Schedin, D. C. Eias, J. A. Jaszczak, and A. K. Geim. Giant Intrinsic Carrier Mobilities in Graphene and Its Bilayer. *Physical Review Letters*, **100**(016602), 2008.

[276] J.-H. Chen, C. Jang, S. Xiao, M. Ishigami, and M. S. Fuhrer. Intrinsic and extrinsic performance limits of graphene devices on SiO_2. *Nature Nanotechnology*, **3**(206), 2008.

[277] A. Akturk and N. Goldsman. Electron transport and full-band electron-phonon interactions in graphene. *Journal of Applied Physics*, **103**(053702), 2008.

[278] T. O. Wehling, M. I. Katsnelson, and A. I. Lichtenstein. Impurities on graphene: Midgap states and migration barriers. *Physical Review B*, **80**(085428), 2009.

[279] A. L. Magna, I. Deretzis, G. Forte, and R. Pucci. Conductance distribution in doped and defected graphene nanoribbons. *Physical Review B*, **80**(195413), 2009.

[280] E. V. Castro, M. P. López-Sancho, and M. A. H. Vozmediano. New Type of Vacancy-Induced Localized States in Multilayer Graphene. *Physical Review Letters*, **104**(036802), 2010.

[281] T. O. Wehling, S. Yuan, A. I. Lichtenstein, A. K. Geim, and M. I. Katsnelson. Resonant Scattering by Realistic Impurities in Graphene. *Physical Review Letters*, **105**(056802), 2010.

[282] H. Miyazaki, K. Tsukagoshi, A. Kanda, M. Otani, and S. Okada. Influence of Disorder on Conductance in Bilayer Graphene under Perpendicular Electric Field. *Nano Letters*, **10**(3888), 2010.

[283] E. R. Mucciolo and C. H. Lewenkopf. Disorder and electronic transport in graphene. *Journal of Physics: Condensed Matter*, **22**(273201), 2010.

[284] V. M. Pereira and A. H. Castro Neto. Strain Engineering of Graphenes Electronic Structure. *Physical Review Letters*, **103**(046801), 2009.

[285] S.-M. Choi, S.-H. Jhi, and Y.-W. Son. Controlling Energy Gap of Bilayer Graphene by Strain. *Nano Letters*, **10**(3486), 2010.

[286] V. M. Pereira, A. H. Castro Neto, H. Y. Liang, and L. Mahadevan. Geometry, Mechanics, and Electronics of Singular Structures and Wrinkles in Graphene. *Physical Review Letters*, **105**(156603), 2010.

[287] W. Bao, F. Miao, Z. Chen, H. Zhang, W. Jang, C. Dames, and C. N. Lau. Controlled ripple texturing of suspended graphene and ultrathin graphite membranes. *Nature Nanotechnology*, **4**(562), 2009.

[288] H. Lind and S. Lidin. A general structure model for BiSe phases using a superspace formalism. *Solid State Sciences*, **5**(47), 2003.

[289] C.-L. Song, Y.-L. Wang, Y.-P. Jiang, Y. Zhang, C.-Z. Chang, L. Wang, K. He, X. Chen, J.-F. Jia, Y. Wang, Z. Fang, X. Dai, X.-C. Xie, X.-L. Qi, S.-C. Zhang, Q.-K. Xue, and X. Ma. Topological insulator Bi_2Se_3 thin films grown on double-layer graphene by molecular beam epitaxy. *Applied Physics Letters*, **97**(143118), 2010.

[290] W. Dang, H. Peng, H. Li, P. Wang, and Z. Liu. Epitaxial heterostructures of ultrathin topological insulator nanoplate and graphene. *Nano Letters*, **10**(2870), 2010.

[291] L. Kleinman. Relativistic norm-conserving pseudopotential. *Physical Review B*, **21**(2630), 1980.

[292] A. H. MacDonald, W. E. Picket, and D. D. Koelling. A linearised relativistic augmented-plane-wave method utilising approximate pure spin basis functions. *Journal of Physics C: Solid State Physics*, **13**(2675), 1980.

[293] P. Błoński and J. Hafner. Magnetic anisotropy of transition-metal dimers: Density functional calculations. *Physical Review B*, **79**(224418), 2009.

[294] D. Hobbs, G. Kresse, and J. Hafner. Fully unconstrained noncollinear magnetism within the projector augmented-wave method. *Physical Review B*, **62**(11556), 2000.

[295] M. Marsman and J. Hafner. Broken symmetries in the crystalline and magnetic structures of -iron. *Physical Review B*, **66**(224409), 2002.

[296] I. Popov, M. Mantega, A. Narayan, and S. Sanvito. Emergence of topological protected states at the graphene-Bi_2Se_3 interface. *Submitted to Physical Review Letters*, , 2012.

[297] Q. Zhang, Z. Zhang, Z. Zhu, U. Schwingenschlögl, and Y. Cui. Exotic topological insulator States and topological phase transitions in Sb_2Se_3-Bi_2Se_3 heterostructures. *ACS Nano*, **6**(2345), 2012.